PNC TN9410 98-015

Super-Phenix Benchmark used for Comparison of PNC and CEA Calculation Methods, and of JENDL-3.2 and CARNAVAL IV Nuclear Data

February, 1998

O-ARAI ENGINEERING CENTER
POWER REACTOR AND NUCLEAR FUEL DEVELOPMENT CORPORATION

複製又はこの資料の入手については、下記にお問い合わせ下さい。
〒311－1393　茨城県東茨城郡大洗町成田町4002
動力炉・核燃料開発事業団
大洗工学センター
システム開発推進部・技術管理室
Inquiries about copyright and reproduction should be addressed to: Technology Management Section, O-arai Engineering Center, Power Reactor and Nuclear Fuel Development Corporation 4002 Narita-machi, O-arai-machi, Higashi-Ibaraki, Ibaraki-ken 311-13, Japan.

© 動力炉・核燃料開発事業団 (Power Reactor and Nuclear Fuel Development Corporation) 1998

Ⓢ

February, 1998

Super-Phenix Benchmark used for comparison of PNC and CEA Calculation Methods, and of JENDL-3.2 and CARNAVAL IV Nuclear Data

Stuart N. Hunter*

Abstract

The study was carried out within the framework of the PNC-CEA collaboration agreement. Data were provided, by CEA, for an experimental loading of a start-up core in Super-Phenix. This data was used at PNC to produce core flux snapshot calculations.

CEA undertook a comparison of the PNC results with the equivalent calculations carried out by CEA, and also with experimental measurements from SPX. The results revealed a systematic radial flux tilt between the calculations and the reactor measurements, with the PNC tilts only ~30-40% of those from CEA.

CEA carried out an analysis of the component causes of the radial tilt. It was concluded that a major cause of radial tilt differences between the PNC and CEA calculations lay in the nuclear datasets used: JENDL-3.2 and CARNAVAL IV.

For the final stage of the study, PNC undertook a sensitivity analysis, to examine the detailed differences between the two sets of nuclear data.

The PNC flux calculations modelled SPX in both 2D (RZ) and 3D (hex-Z) geometries, using the diffusion programs CITATION and MOSES.

The sensitivity analysis of the differences between the JENDL-3.2 and CARNAVAL IV nuclear datasets used the SAGEP calculational route. Both datasets were condensed to a single, non-standard, set of energy group boundaries. There were some incompatibilities in the cross-section formats of the two datasets.

The sensitivity analysis showed that a relatively small number of nuclear data items contributed the bulk of the radial tilt difference between calculations with JENDL-3.2 and with CARNAVAL IV.

A direct comparison between JENDL-3.2 and CARNAVAL IV data revealed the following. The Nu values showed little difference (<5%). The only large fission cross-section differences were at low energy (<30% otherwise, with <10% typical). Although down-scattering reactions showed some large fractional differences, absolute differences were negligible compared with in-group scattering; for in-group scattering fractional differences were up to ~75%, but generally <20%. There were many large differences in capture cross-sections, generally ~30-200%.

---

* PNC International Fellow (20'th April 1995 -)
Reactor Physics Research Section, Advanced Technology Division,
O-arai Engineering Center, PNC, Japan

PNC TN9410 98-015
1998年 2月

Super-Phenixベンチマークによる PNCとCEAの解析手法及び核データの比較

スチュアート N. ハンター*

要 旨

本研究は、CEAから提供されたSuper-Phenixの起動試験炉心ベンチマークデータを動燃が解析した成果であり、動燃－CEA共同研究の一環として実施されたものである。

動燃によるSuper-Phenixの解析結果を、CEAの解析結果及び実験測定値と比較したところ、CEAのC/E（解析/実験）値が系統的な径方向依存性を示すのに対して、動燃のC/E値はその30～40%しかなく非常に小さいことが判明した。CEAが原因を検討した結果、両者のC/E値径方向依存性の違いの主たる要因は、使用した核データセット（JENDL-3.2とCARNAVAL-Ⅳ）にあると結論された。

本検討の最終段階として、動燃はこの2種の核データセットの違いを詳細に検討するために、感度解析を実施した。中性子束分布計算で用いた解析コードは2次元RZまたは3次元Hex-モデルのCITATIONとMOSESコードである。JENDL-3.2とCARNAVAL-Ⅳの違いに対する感度解析は、SAGEPコードを用いて行われた。ここでは、両者のエネルギー構造を統一するための縮約操作を施す必要があり、また、両者の核断面積の定義には幾つか食い違いがあることが分かった。

感度解析の結果、JENDL-3.2とCARNAVAL-ⅣのC/E値径方向依存性の違いの原因は、少数の核種による寄与であることが判明した。両者の核データの比較結果は以下のとおりである。核分裂当たりの中性子発生数νの違いは小さい（<5%）。低エネルギーでの核分裂断面積差は大きい（<30%、代表値<10%）。下方散乱断面積は相対差としては大きい違いがあるが、絶対値の差は自群散乱と比較すれば無視できる。自群散乱の相対差は75%程度まであり、一般には20%以下である。捕獲断面積の違いは非常に大きく、30～200%まで見られた。

---

* 動燃 大洗工学センター 基盤技術開発部 炉心技術開発室 国際特別研究員（1995年4月20日～）

CONTENTS

LIST OF TABLES

LIST OF FIGURES

1 INTRODUCTION

This report describes a short series of calculations that were carried out within the framework of the PNC - CEA collaboration agreement. A major purpose of the calculations was to provide some comparison between the different calculational methods and data employed by PNC and CEA.

The scope of the calculations covered basic steady-state reactor physics calculations (power and flux distributions, Keff values, 1-group nuclear data) for a fast reactor core. The calculations modelled a specific loading of the Super-Phenix (SPX) reactor, for which experimental measurements were available for comparison with the calculations.

The data describing the SPX states modelled were provided by CEA, they are given in Section 2 of the report. The PNC calculation methods used in this study to model SPX are described in Section 3. The results of the calculations are given in Section 4, along with the comparison with the equivalent CEA calculations and SPX measurements.

One major feature of the results was a marked radial rating tilt, relative to the SPX measurements; this occurred in all the calculations, but was more pronounced in those carried out by CEA. Analysis of the causes of the radial tilt was carried out by CEA, it is outlined briefly in Section 5. Errors in nuclear data were seen to cause a major component of the radial tilt.

A sensitivity analysis was carried out, to analyse the effects on the calculated radial tilts of the different nuclear data used by PNC and CEA. The PNC calculations used data based on JENDL-3.2, whilst the CEA data was based on CARNAVAL IV. The method used is described in Section 6 and the results are given in Section 7.

2 SUPER-PHENIX STATES MODELLED

The configuration of SPX that was modelled was an experimental loading of a start-up core, one in which a number of diluent S/As were loaded. The complete core was loaded as clean fuel, then irradiated at a fraction of full power.

The study modelled the SPX core in 4 states; two were the basic core configuration in clean and irradiated states, two were variations on the basic configuration. These 4 states, and the names used to identify them, were:

'28cm'	clean core,	CSDs 28 cm in, DSDs 0 cm in
'No Rods'	clean core,	CSD & DSD absorber removed from model
'All Fuel'	clean core,	rod & diluent S/As changed to fuel
'50 efpd'	~50 efpd irradiation,	CSDs 28 cm in, DSDs 0 cm in

All 4 states were with the reactor at hot operating temperatures. (CSDs are 'control and shutdown' or main rods, DSDs are 'diverse shutdown' or backup rods.)

The irradiation of the clean core to ~50 efpd was in the following 3 steps:

144 days at 0.0827 power, with CSD rods 40 cm inserted
124 days at 0.1035 power, with CSD rods 35 cm inserted
105 days at 0.2413 power, with CSD rods 28 cm inserted.

The full reactor power is 2990 MW(th).

The core composition was provided in the form of number density data for the clean core. Data was provided for 11 distinct material compositions, with the 8 different S/A types that make up the reactor model being constructed in a series of axial segments each corresponding to one of the 11 materials. The radial S/A distribution is shown in Figure 2.1, and the axial composition of each S/A type is shown in Figure 2.2. The number densities for the 11 material regions are given in Table 2.1.

The composition data is provided for an axial model height of 260 cm, corresponding to 100 cm of core, upper and lower axial breeders each of 30 cm, upper and lower axial shields each of 50 cm. These axial dimensions are for the cold reactor, they should be increased by a factor 1.008136 to adjust to hot operating temperatures - the same adjustment should be made to the various CSD insertions already quoted.

The radial S/A pitch is 18.019 cm at hot operating conditions. The number densities of Table 2.1 are also for hot operating conditions. Material temperatures were given as 1500K for the (U,Pu)O_2 in the fuel regions, 900 K for the UO_2 in the breeder regions, and 743 K for all other materials.

Since data was provided already in the form of number densities, there was no general need for detailed information on the structure (e.g. fuel pin size). However, heterogeneous models of rod absorbers were used (see Sub-section 3.3), so their structure was required. The CSDs have 31 absorber pins, on a 4 ring hexagonal lattice of 22.766 mm pin-to-pin pitch, with the 6 corner pins omitted. Each pin is clad in 1mm thick steel. The volume fractions are 46.94% Na, 25.36% B_4C and 27.70% steel (of which 14.33% is wrapper tube). For the DSDs the volume fractions are 65.84% Na, 16.77% B_4C and 17.08% steel (of which 9.67% is wrapper tube); the absorber geometry was taken to be a single steel-sheathed pin.

For the 'All Fuel' case, inner zone fuel S/As replace the 3 DSDs, the inner ring of 3 diluent S/As, the inner ring of 6 CSDs, and the 9 innermost of the outer ring of CSDs. The remaining 6 CSDs and 15 diluent S/As are replaced by outer zone fuel S/As. This gives a total of 211 inner zone fuel S/As and 179 outer zone fuel S/As.

For the 'No Rods' case, the axial compositions of the CSD and DSD S/A types became a full 260 cm height of the appropriate follower material. Where the CSD absorber insertion was altered from 28 cm to a different value (during the burn-up to ~50 efpd), only the absorber-follower interface was moved, the upper end of the absorber remained at the top of the S/A model.

All the data quoted in this section were provided directly by CEA, specifically for the purposes of the comparison exercise.

Table 2.1 Clean core number density data

	Reactor Region					
	Inner Fuel	Outer fuel	Axial Blanket	Radial Blanket	Shield	Diluent
U235	$2.8098\text{x}10^{-5}$	$2.6246\text{x}10^{-5}$	$2.2161\text{x}10^{-5}$	$3.0658\text{x}10^{-5}$		
U238	$7.0837\text{x}10^{-3}$	$6.6902\text{x}10^{-3}$	$8.7306\text{x}10^{-3}$	$1.2078\text{x}10^{-2}$		
Pu238	$5.1215\text{x}10^{-6}$	$7.2075\text{x}10^{-6}$				
Pu239	$9.0032\text{x}10^{-4}$	$1.1045\text{x}10^{-3}$				
Pu240	$2.9957\text{x}10^{-4}$	$3.5148\text{x}10^{-4}$				
Pu241	$5.5846\text{x}10^{-5}$	$7.1233\text{x}10^{-5}$				
Pu242	$2.1903\text{x}10^{-5}$	$2.7470\text{x}10^{-5}$				
Am241	$2.1191\text{x}10^{-5}$	$1.8460\text{x}10^{-5}$				
Fe	$1.3062\text{x}10^{-2}$	$1.3062\text{x}10^{-2}$	$1.3062\text{x}10^{-2}$	$1.0075\text{x}10^{-2}$	$2.6625\text{x}10^{-2}$	$3.9139\text{x}10^{-2}$
Cr	$3.7589\text{x}10^{-3}$	$3.7589\text{x}10^{-3}$	$3.7589\text{x}10^{-3}$	$2.8993\text{x}10^{-3}$	$7.6619\text{x}10^{-3}$	$1.1263\text{x}10^{-2}$
Ni	$2.7416\text{x}10^{-3}$	$2.7416\text{x}10^{-3}$	$2.7416\text{x}10^{-3}$	$2.1146\text{x}10^{-3}$	$5.5882\text{x}10^{-3}$	$8.2147\text{x}10^{-3}$
Mo	$3.2955\text{x}10^{-4}$	$3.2955\text{x}10^{-4}$	$3.2955\text{x}10^{-4}$	$2.5418\text{x}10^{-4}$	$6.7172\text{x}10^{-4}$	$9.8743\text{x}10^{-4}$
O	$1.6663\text{x}10^{-2}$	$1.6428\text{x}10^{-2}$	$1.7506\text{x}10^{-2}$	$2.4217\text{x}10^{-2}$		
Na	$7.3689\text{x}10^{-3}$	$7.3689\text{x}10^{-3}$	$7.3689\text{x}10^{-3}$	$5.6096\text{x}10^{-3}$	$1.0931\text{x}10^{-2}$	$5.7635\text{x}10^{-3}$
Ti	$9.6008\text{x}10^{-5}$	$9.6008\text{x}10^{-5}$	$9.6008\text{x}10^{-5}$	$7.4051\text{x}10^{-5}$	$1.9570\text{x}10^{-4}$	$2.8767\text{x}10^{-4}$
Cu	$6.3329\text{x}10^{-5}$	$6.3329\text{x}10^{-5}$	$6.3329\text{x}10^{-5}$	$4.8846\text{x}10^{-5}$	$1.2909\text{x}10^{-4}$	$1.8976\text{x}10^{-4}$
Si	$2.2514\text{x}10^{-4}$	$2.2514\text{x}10^{-4}$	$2.2514\text{x}10^{-4}$	$1.7365\text{x}10^{-4}$	$4.5891\text{x}10^{-4}$	$6.7460\text{x}10^{-4}$
Mn	$3.1391\text{x}10^{-4}$	$3.1391\text{x}10^{-4}$	$3.1391\text{x}10^{-4}$	$2.4212\text{x}10^{-4}$	$6.3984\text{x}10^{-4}$	$9.4057\text{x}10^{-4}$

	Reactor Region				
	CSD Follower	CSD Absorber	DSD Follower	DSD Absorber	Neutron Guide
Fe	$7.6307\text{x}10^{-3}$	$1.4750\text{x}10^{-2}$	$5.1493\text{x}10^{-3}$	$9.0951\text{x}10^{-3}$	$1.7572\text{x}10^{-2}$
Cr	$2.1959\text{x}10^{-3}$	$4.2447\text{x}10^{-3}$	$1.4818\text{x}10^{-3}$	$2.6173\text{x}10^{-3}$	$5.0568\text{x}10^{-3}$
Ni	$1.6016\text{x}10^{-3}$	$3.0959\text{x}10^{-3}$	$1.0808\text{x}10^{-3}$	$1.9089\text{x}10^{-3}$	$3.6882\text{x}10^{-3}$
Mo	$1.9252\text{x}10^{-4}$	$3.7213\text{x}10^{-4}$	$1.2991\text{x}10^{-4}$	$2.2946\text{x}10^{-4}$	$4.4334\text{x}10^{-4}$
B10		$2.3597\text{x}10^{-2}$		$1.5604\text{x}10^{-2}$	
B11		$2.6219\text{x}10^{-3}$		$1.7338\text{x}10^{-3}$	
C		$6.5548\text{x}10^{-3}$		$4.3345\text{x}10^{-3}$	
Na	$1.8776\text{x}10^{-2}$	$1.0259\text{x}10^{-2}$	$1.9800\text{x}10^{-2}$	$1.4415\text{x}10^{-2}$	$7.1929\text{x}10^{-3}$
Ti	$5.6086\text{x}10^{-5}$	$1.0842\text{x}10^{-4}$	$3.7848\text{x}10^{-5}$	$6.6850\text{x}10^{-5}$	$1.2916\text{x}10^{-4}$
Cu	$3.6996\text{x}10^{-5}$	$7.1513\text{x}10^{-5}$	$2.4965\text{x}10^{-5}$	$4.4096\text{x}10^{-5}$	$8.5196\text{x}10^{-5}$
Si	$1.3152\text{x}10^{-4}$	$2.5424\text{x}10^{-4}$	$8.8753\text{x}10^{-5}$	$1.5676\text{x}10^{-4}$	$3.0288\text{x}10^{-4}$
Mn	$1.8338\text{x}10^{-4}$	$3.5447\text{x}10^{-4}$	$1.2375\text{x}10^{-4}$	$2.1857\text{x}10^{-4}$	$4.2230\text{x}10^{-4}$

Number Densities are in atoms/cc x 10^{-24}

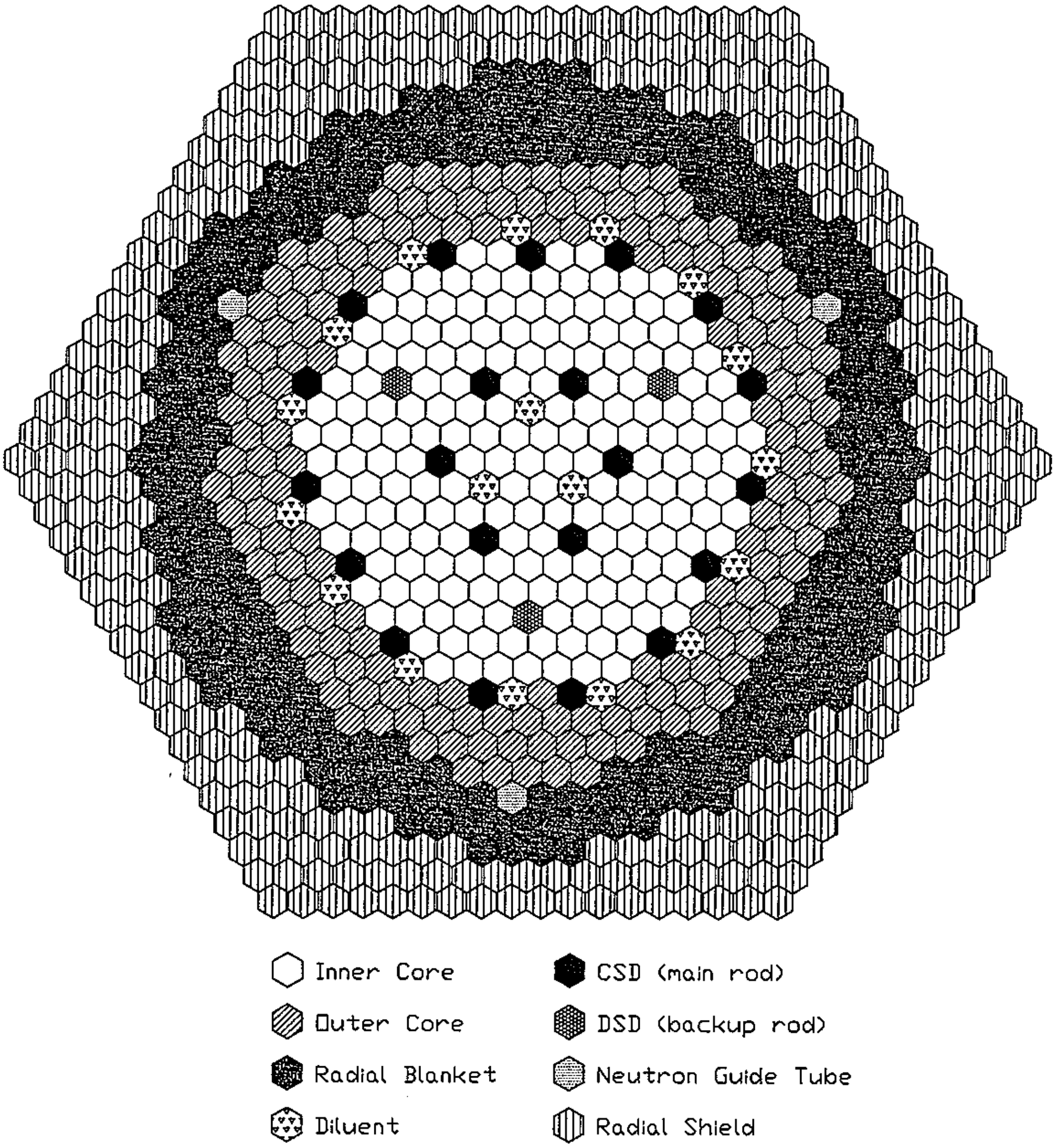

Figure 2.1 Reactor S/A layout of Super-Phenix experimental loading

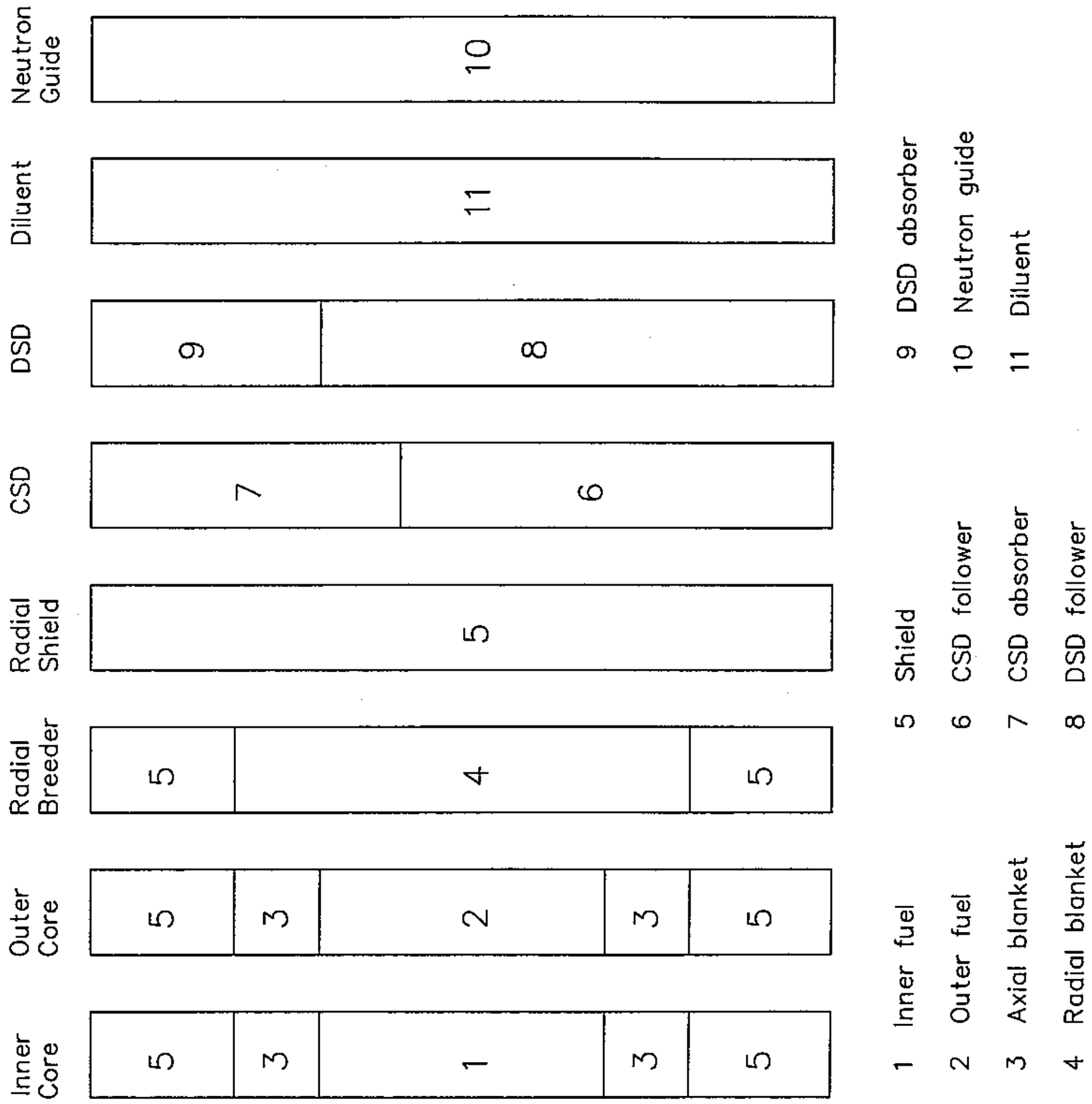

Figure 2.2 Axial S/A compositions of Super-Phenix experimental loading

3 SUPER-PHENIX MODELLING METHODS

The PNC assessment of the SPX experimental loading produced both 2D (RZ) and 3D (hex-Z) snapshot calculations for each of the 4 reactor states defined in Section 2. These calculations were produced using respectively the diffusion codes CITATION$^{(3-1)}$ and MOSES. In addition, there are calculations to condense 70-group nuclear data, which were based on JENDL-3.2$^{(3-2)}$, to the lesser numbers of groups used in (some of) the diffusion calculations. One group cross-section data were also produced, for comparison purposes. There were also calculations to evaluate the changes in fuel and breeder region number densities with the irradiation to ~50 efpd.

3.1 CLEAN CORE CALCULATIONS

For each of the three clean core conditions - '28 cm', 'All Fuel' and 'No Rods' - the same sequence of calculations was carried out. Steady state calculations were required for both the 2D (RZ) CITATION diffusion model and the 3D (hex-Z) MOSES diffusion model. The CITATION calculation was done using the full 70-group nuclear data structure: the results of this calculation were used to condense the nuclear data to 7 groups, for use with the larger model of the MOSES calculation. To obtain 1-group cross-section data, the original 70-group CITATION calculation was repeated, but with the subsequent condensation modified to give 1-group rather than 7-group data. The CITATION calculation was also repeated using the 7-group data, to aid in the comparison of the different PNC calculations. Figure 3.1 gives a schematic representation of the calculational route.

The 70-group CITATION calculations incorporated preliminary SLAROM$^{(3-3)}$ cell calculations, to produce effective cross-section data for the particular material compositions from the infinite dilution data of JENDL-3.2. The 7-group data produced by the condensations is already in the correct format for direct use in the CITATION and MOSES calculations.

The reactor geometry represented in the calculations corresponded directly to the data of Section 2, with the exception that for the 2D (RZ) calculations the S/A map of Figure 2.1 had to be represented as a 1D radial band structure. The radial material structure used is shown in Figure 3.2; for the 'All Fuel' case there are no CSD, DSD or diluent regions, just the inner core out to a radius of 137.42 cm, and the outer core from there to 189.22 cm.

The axial flux representation used meshes of 5 cm height in the core and breeders, with the mesh size increasing to 10 cm at the top and bottom of the axial shield regions. The radial flux modelling used 1 mesh per S/A in the 3D calculations; in the 2D calculations the radial mesh had to be fitted to the material structure of Figure 3.2, the typical mesh size was ~5 cm.

3.2 IRRADIATED CORE CALCULATIONS

A similar set of calculations was carried out for the '50 efpd' case as was undertaken for the clean core cases: a 70-group 2D CITATION calculation, with condensation of nuclear data to both 7 and 1 energy groups; a 7-group 3D MOSES calculation; a repeat of the 2D CITATION calculation, but using the 7-group nuclear data. Unlike the clean core calculations, it was necessary to first compute the variation in the core and breeder number densities; these are changed from their initial clean core values, a result of the irradiation. Figure 3.3 gives a schematic representation of the complete calculational route for the '50 efpd' case.

For the clean core, only a single number density region was needed to represent each core enrichment zone; for the irradiated core, a full representation requires a large number of number density regions. A large number of number density zones is not compatible with a 70-group calculation, because of data storage requirements. The calculation of irradiated number densities was carried out in two iterations.

First, a 70-group SLAROM and CITATION snapshot calculation for clean core conditions (i.e. identical to the '28 cm' case) was used to condense 7-group clean core nuclear data; this data was used in a detailed (90 number density region) CITATION burn-up calculation of irradiation to 25 efpd (i.e. the mean burn-up of the irradiation to

~50 efpd). The mean burn-up number densities produced by the foregoing calculation were restructured to a less detailed (15 number density region) form and used in a 70-group SLAROM and CITATION snapshot calculation, from which were condensed 7-group nuclear data for the mean burn-up condition.

The second iteration consisted of modelling the burn-up in 3 consecutive steps, with the power, duration and CSD insertions as given in Section 2. CITATION burn-up calculations were used, with 90 number density zones and using the 7-group mean burn-up nuclear data produced by the first iteration. This produced number density data, in 90 regions, for the ~50 efpd burn-up core.

The number density data calculated as described above were used to carry out the required '50 efpd' calculations. A 70-group SLAROM and 2D CITATION snapshot calculation was done (with the number density data restructured to a 15 region representation), with subsequent condensations to produce 7-group and 1-group nuclear data. The 7-group nuclear data was used for the 3D MOSES snapshot calculation, which was restricted to the 15 region number density model; the same nuclear data was also used for 2D CITATION snapshot calculations, with both 15 region and 90 region number density representations.

The 90 region number density model represented the reactor as follows. The core was divided into 10 axial meshes (each of 10 cm) and 8 radial meshes (5 inner core and 3 outer core), for a total of 80 core regions. There were 2 axial and 1 radial breeder regions, and 7 other (non-evolving) regions - shield, diluent, neutron guide, absorber and follower for both CSD and DSD. The 15 region model is as follows. The core has 3 axial meshes, of 20, 60 and 20 cm, in each of the fuel enrichment zones, for 6 core regions. The axial breeders were represented as a single number density region, distinct from the radial breeder region. The remaining 7 regions were the same non-evolving regions as previously.

The clean core calculations used a 12 region number density representation: one region for each core enrichment zone, 7 non-evolving regions, and 3 breeder zones (upper, lower and radial). The upper and lower axial breeders, although represented separately, have identical clean core compositions.

3.3 ABSORBER MODELLING

Unlike the other regions, the CSD and DSD absorbers are modelled heterogeneously in the SLAROM calculations of effective cross-sections. Without such a representation, the reactivity effect of the absorber would be significantly over-estimated.

The heterogeneous structures that can be modelled are limited to those geometry options available in the SLAROM program. The DSD was represented in a simple 1D cylindrical geometry, this models exactly a single absorber pin, with a very minor distortion of the hexagonal wrapper tube. For the CSD, a geometry option was used that is a close approximation to the design: a series of concentric hexagonal arrays of circular rods, overlaid on a series of concentric hexagonal regions. The only notable difference was that the outer ring of pins had to be spaced evenly, rather than leaving a gap for the pins missing from a regular hexagonal array. For both absorber types, a supercell model was used, representing a single absorber S/A surrounded by a region of fuel equivalent to 14.9 S/As (14.9:1 being the ratio of fuel to absorber S/As in the reactor).

For the DSD model, the radii of the various regions were determined by the volume fractions of the component materials. The unspecified volume fraction was placed as a void gap between the B_4C and its steel sheath. All the steel not in the wrapper tube was placed in the steel sheath.

The volume fraction of the B_4C in the CSD absorber implied a 0.856 cm radius for each B_4C region, with a 1mm thick steel sheath around them extending their radii to 0.956 cm. The overall steel volume fraction was greater than that occupied by the pin sheaths and wrapper tube; the extra steel was positioned in a region between the pin bundle and the wrapper, mixed with Na coolant (this additional steel in practise forms the pin bundle support structures).

Figure 3.4 shows, for both CSD and DSD absorbers, both the actual S/A cross-section and that modelled in the SLAROM calculations. The models are seen to be good approximations of the real geometries.

In the 2D calculations, no adjustments were made to the absorber nuclear data to allow for the distorting effects on absorber worth of the RZ geometry.

3.4 OTHER

In carrying out the calculations, no corrections were made for known systematic errors in calculation methods: such factors as mesh size effect, fuel cell heterogeneity or transport effects.

The number density data supplied by CEA included three minor elements in the steel composition - Ti, Cu and Si - which are not incorporated in the standard PNC calculational route. The calculational route was modified to include these three elements.

3.5 CEA METHODS

In the folowing Section, the results of the calculations described above are compared with equivalent calculations produced by CEA. There is only partial information available on the CEA calculation methods. CEA carried out both 2D and 3D calculations. Nuclear data from CARNAVAL IV was used. Representation of absorber heterogeneity effects was by reducing the boron concentration, to a level determined using rod worth measurements. The 3D calculations were in 6 energy groups, they used hex-Z geometry with 7 mesh points per S/A.

The comparison also includes some results of calculations by IPPE (Russia). The only available information on the methods used was to distinguish whether 2D or 3D geometry was used.

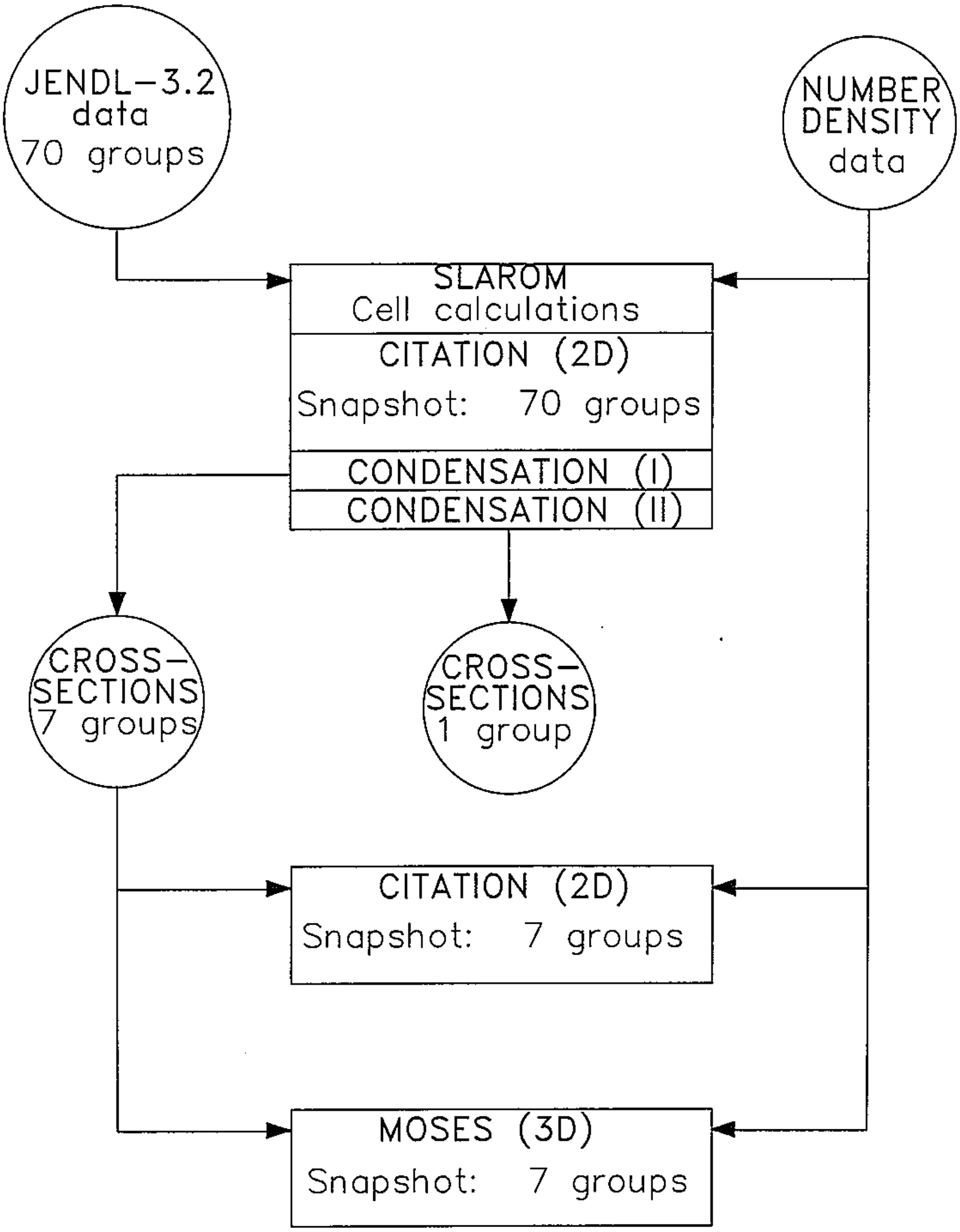

Figure 3.1 PNC calculational route - clean core cases

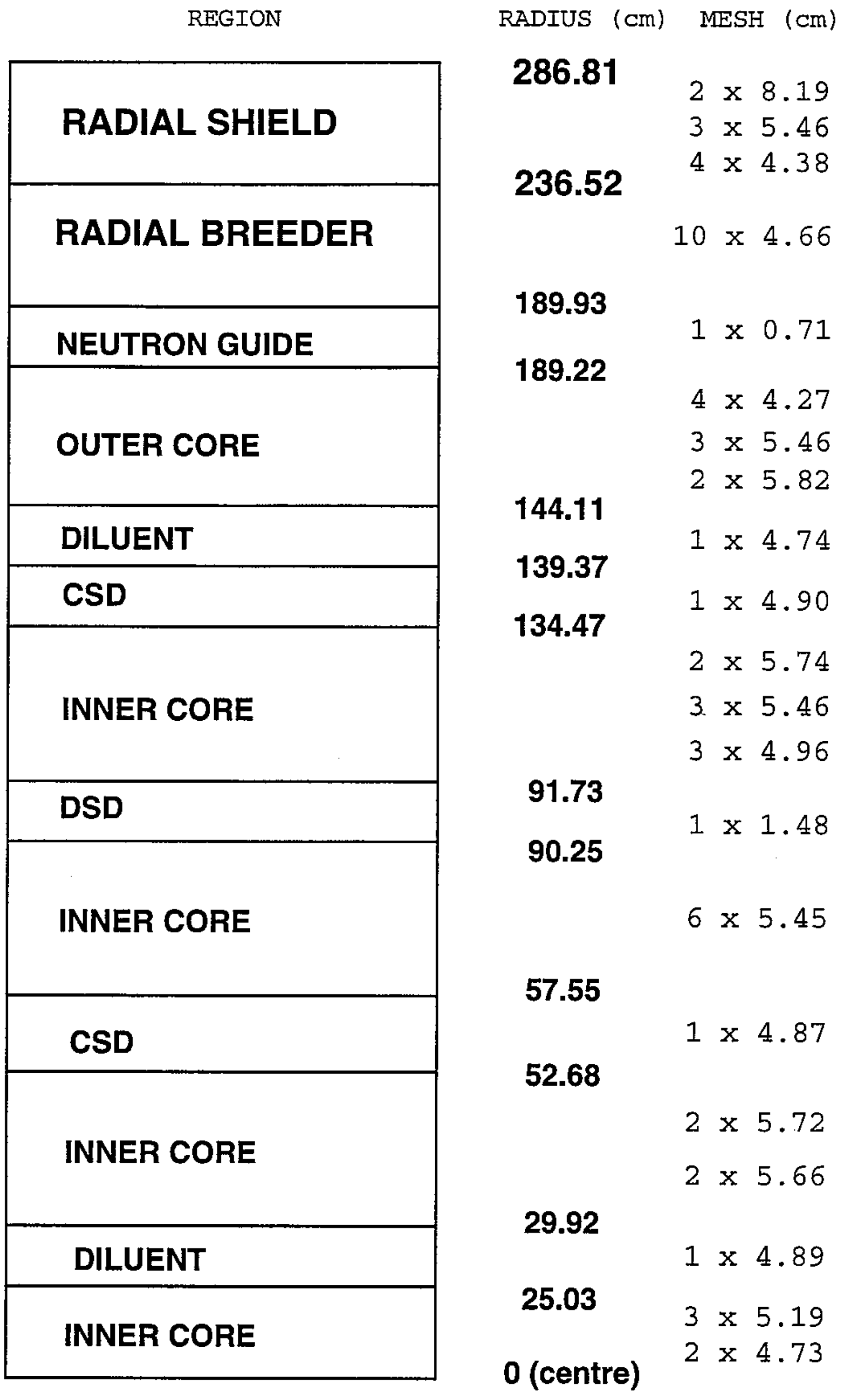

Figure 3.2 Radial region structure for 2D model (PNC calculations)

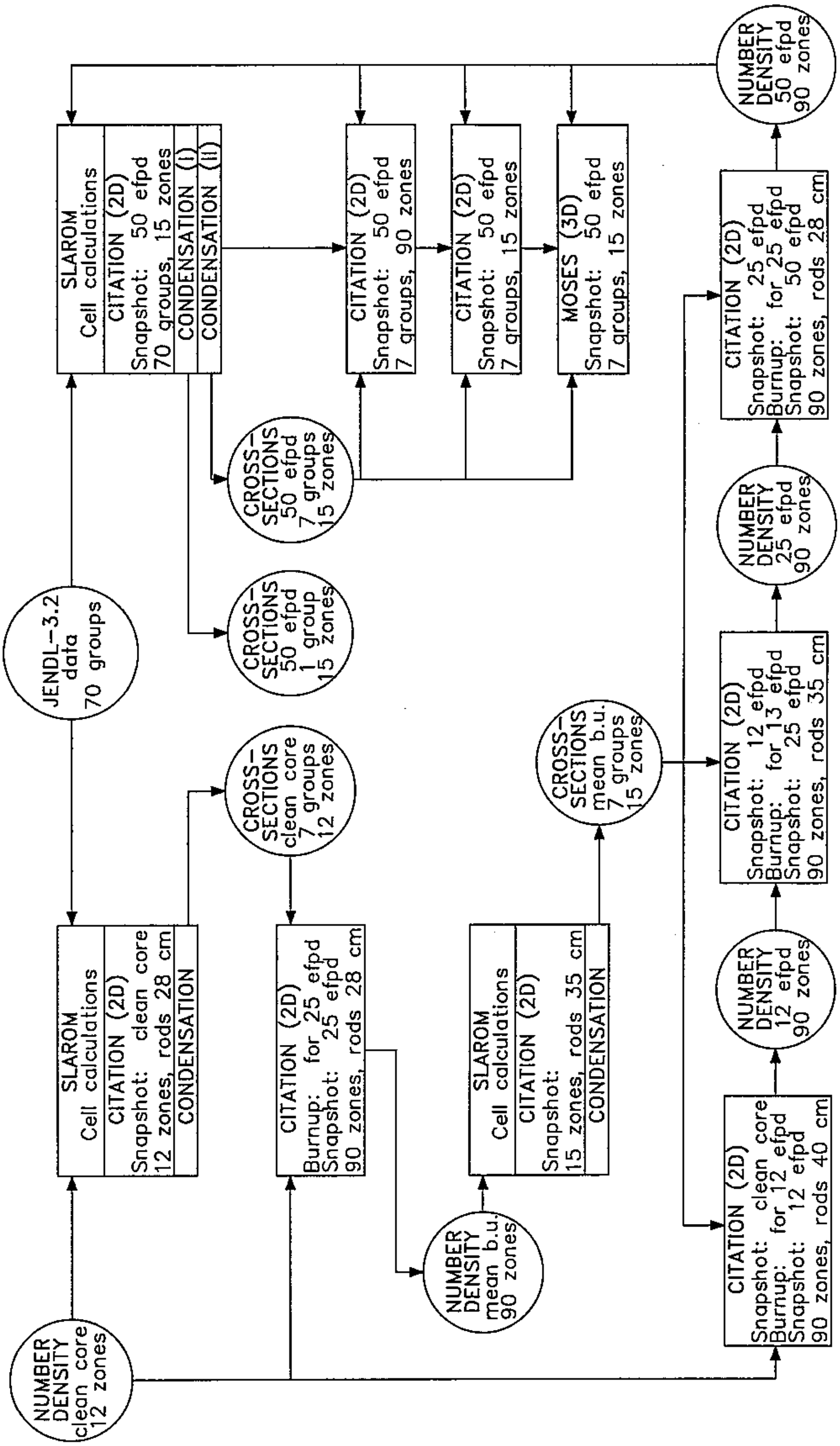

Figure 3.3 PNC calculational route - ~50 efpd irradiated case

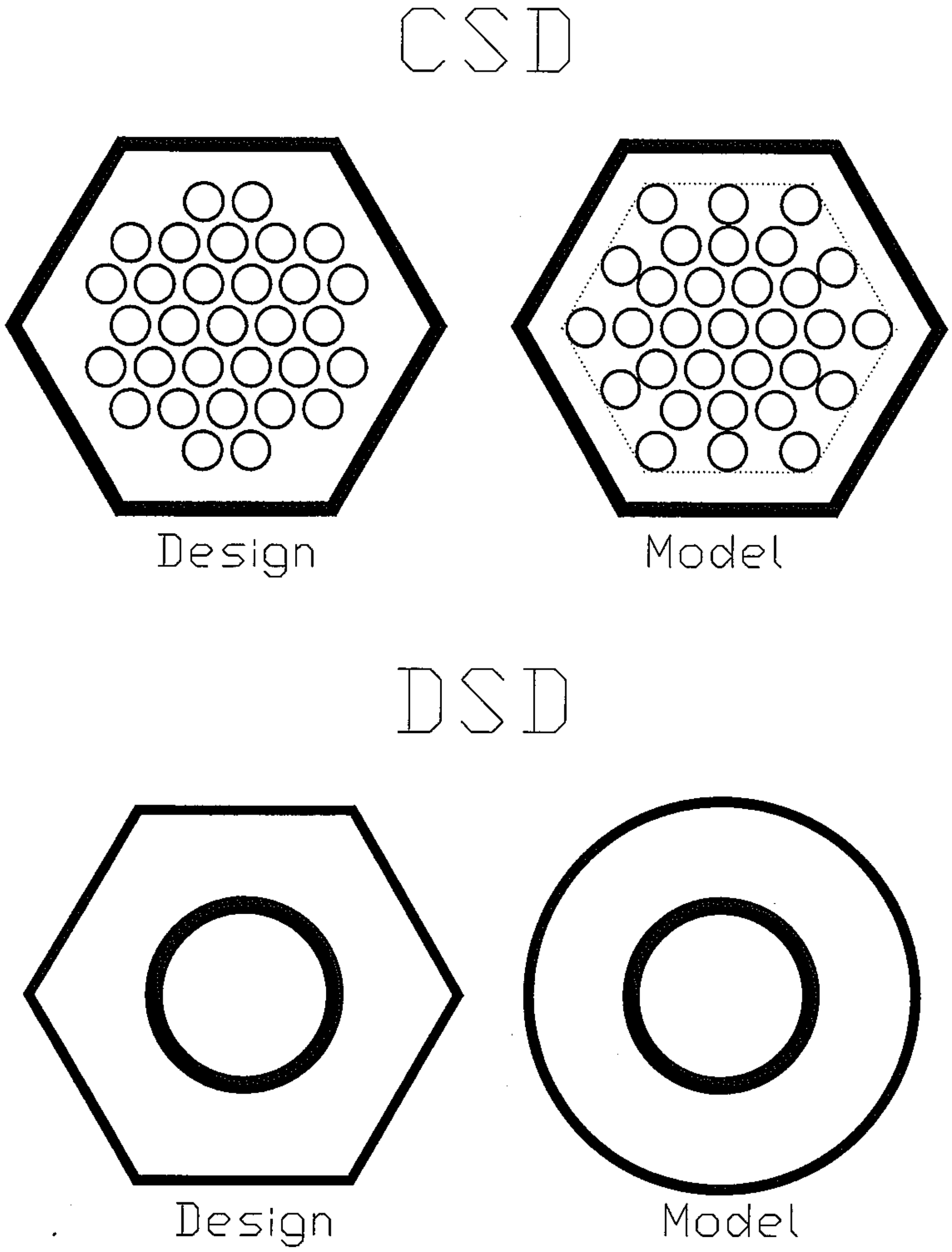

Figure 3.4 Cross-sections of S/As and cell models for rod absorbers

4 RESULTS

The analysis was limited to steady-state flux calculations for specific core configurations. As a consequence, the range of results available is somewhat limited compared with a full reactor physics fuel cycle assessment. The core reactivities (Keff values), together with the flux and rating distributions were the parameters examined as characteristic of the different core states; 1-group nuclear data were also produced.

Table 4.1 shows the values of Keff for each of the four cases, as calculated by the two different diffusion models and for different numbers of energy groups. The effect of condensing from 70 to 7 energy groups for the 2D CITATION calculations had a small and consistent effect, increasing Keff by ~0.06%. The effect of changing the calculation method and model from 2D to 3D (i.e. from CITATION to MOSES) is rather more significant, but varies between the four cases, from -0.1% to +0.6%: there are several contributing factors, 2D/3D geometry effects, radial mesh size (~5 cm in 2D, 18 cm S/A in 3D), as well as any differences in the modelling in the 2 programs. Table 4.1 also shows that, for the irradiated '50 efpd' case, the difference between the coarse (15 region) and detailed (90 region) representations of core number densities was insignificant as far as Keff was concerned - 0.014%.

In essence, the difference between the '28 cm' and 'No Rods' cases is that the absorber rods are at different insertions (in the 'No Rods' case they are completely removed from the model). Thus the difference in Keff values is a measure of absorber worth - 2.17%Δk/kk' for the 2D CITATION calculations and 1.82%Δk/kk' for the 3D MOSES calculations. This indicates that the 2D calculations do, as expected, overestimate the effectiveness of the absorber, by ~20%.

The conditions of the '28 cm' and '50 efpd' cases differ only in the burn-up of the core, thus the difference in their Keff values is a measure of the rate of loss of reactivity with irradiation. There is some difference between 2D and 3D calculations, for the former the reactivity loss is 0.8%Δk/kk', whereas for the latter it is only 0.66%Δk/kk'.

For the analysis to be described in Sections 6 and 7, it was necessary to repeat a calculation for the '28 cm' case, but with the CSD and DSD absorbers represented as homogeneous cells in the SLAROM calculations of effective cross-sections. The calculation used the 2D geometry (CITATION) and 70 energy groups. The resulting value of Keff was 0.98217. Comparing with the equivalent 'No Rods' case determines the worth of the homogeneous absorber to be 2.52%Δk/kk', an overestimate of ~16% compared with the 2.17%Δk/kk' value obtained using the heterogeneous absorber model.

Plots, for all four cases, of the radial variation in flux and rating in the 2D calculations are shown in Figures 4.1 and 4.2 respectively. In each case, the data were taken from the calculations with 7 group nuclear data. The flux values were taken from a single axial mesh, the 5 cm immediately above the core mid-plane, and the total flux summed over the 7 energy groups. The rating values plotted are the axially integrated power at each radial position, the summation covering axial breeder zones in addition to the core; the results are given as MW per S/A, for direct comparison with the 3D MOSES and SPX measurement values.

The behaviour of the 'All Fuel' case is rather different from that of the other three cases: it has an essentially flat flux and rating distribution over the inner enrichment zone - the uniform composition causes the flux and rating to be smooth, though not necessarily flat. The three other cases show a decided rating increase in the outer part of the inner enrichment zone, especially the '28 cm' and '50 efpd' cases, those in which absorber material is included. It was considered possible that the distorting effects of adopting a 2D model were responsible for the flux and rating hump.

Figures 4.3 to 4.6 compare the 2D radial rating distributions of Figure 4.2 with the radial rating distributions from the equivalent 3D MOSES calculations. The 3D radial distributions are displayed both as individual S/A powers, and as a plot of the average power for each hexagonal ring of S/As.

It is clear that, compared with the 3D model, the 2D calculations introduce a radial rating tilt, reducing rating in the centre of the core and raising it at the edge (in the 'All Fuel' case the effect is marginal). The 2D calculations produced a pronounced rating hump in the outer part of the inner enrichment zone, occurring in those cases in which absorber material is present in the model. This hump is still present in the 3D calculations, though somewhat less severe. It is apparent that the hump is caused by the absorber: in 2D geometry the effect of absorber is enhanced, but the calculations included no adjustments to offset this effect. Towards the outer part of the core, the ratings of the individual S/As in the 3D calculations show quite a scattering, rather than varying smoothly with radius (this is particularly so for the 'All Fuel' case): this is a consequence of the local presence of rod and diluent S/As.

1-group cross-section data were produced for each of the 4 cases. Table 4.2 shows the values produced for five main cross-sections - absorption, nu*fission, fission, total and diffusion. The SLAROM calculations used a diagonal transport approximation, so the transport and total cross-section values are identical. Values are given for each material region in each of the four cases. There is not a great deal of variation in cross-sections between the four cases; unsurprisingly, the largest differences (up to ~5%) were seen in the evolving regions (core and breeder) of the irradiated '50 efpd' case.

4.1 COMPARISON WITH CEA

The calculations described above were carried out to provide data for comparison with CEA calculations (and also with measurements made on SPX itself). The comparison was carried out by CEA, only a limited amount of CEA data has been supplied to enable PNC to undertake its own comparison assessment.

A number of Keff values for CEA calculations are available, though only for 3D calculations. Table 4.3 compares Keff values from PNC and CEA, for 3D diffusion calculations for the four cases. All the CEA calculations predict a higher value for Keff, by ~2% for the 'All Fuel' and 'No Rods' cases, but only by ~1% for the '28 cm' and '50 efpd' cases. There are several possible causes for the Keff differences between PNC and CEA, these include mesh size (1 or 7 meshes per S/A) and program model differences, but the most likely source is from nuclear data differences. Whether the difference is ~2% or ~1% corresponds to whether or not absorber materials are present in the reactor.

What was calculated as a 1.82%Δk/kk' absorber worth for the PNC calculations is increased to 2.90%Δk/kk' for the CEA calculations. It is understood that the CEA calculations did take account of absorber heterogeneity, but by artificially reducing the boron density, rather than explicitly. Absorber modelling is an area of significant difference between the PNC and CEA calculations.

The CEA value for the reduction in Keff with the irradiation change from case '28 cm' to case '50 efpd' was 0.61%Δk/kk', in agreement with the PNC value of 0.66%Δk/kk'.

Further Keff values are given in Table 4.4, showing the variation over the 3 stages of the irradiation to ~50 efpd. The PNC calculations were with the 2D model, whereas the equivalent CEA calculations used a 3D model. The variation in the Keff difference between PNC and CEA calculations, corresponds to the greater effect in the CEA calculations of the gradual withdrawal from the core of the CSD absorber. The cases of Table 4.4 represent the actual SPX burn-up conditions and therefore should be just critical: both PNC and CEA calculations underestimated Keff, by ~1% or more. The 0.4%Δk/kk' difference between the final PNC value of Table 4.4 and the equivalent case from Table 4.1 is a consequence of the 7 group nuclear data used being condensed for different conditions (those in table 4.4 are for the mean burn-up of 25 efpd).

Figures 4.7 and 4.8 show, for the '28 cm' and '50 efpd' cases respectively, the radial rating distribution in 2D calculations by both PNC and CEA (the '28 cm' case also includes the results of a calculation carried out at IPPE, Russia, which also provided results for CEA's comparison exercise). The graphs are in the form of the percentage variation from SPX measurements, as a function of S/A ring. Two things are worth noting about these results. All the calculations show a radial tilt relative to the SPX measurements, ratings raised towards the core centre and depressed at the core edge; the CEA calculations produce a significantly larger tilt than the others. Secondly, there is a remarkable degree of similarity in the radial rating shape between the one IPPE calculation presented and the equivalent PNC calculation. This similarity suggests that there is little effective difference between the PNC and IPPE nuclear data and methods used (at least for 2D calculations). The irregular difference between the PNC (and IPPE) results and the SPX measurements is considered to be, at least in part, a consequence of the radial band approximation (Fig. 3.2) that is necessary in 2D (RZ) geometry.

Using values of rating as a fraction of SPX measured values from Figures 4.7 and 4.8, and taking radial tilt as the ratio of maximum to minimum values; the PNC calculations gave radial tilts of 1.060 and 1.094 for the '28 cm' and '50 efpd' cases, whilst the CEA calculations produced tilts of 1.217 and 1.233; the IPPE calculation for the '28 cm' case gave a tilt of 1.098. The size of the tilts (variations from 1.0) calculated by PNC were only 28% and 40% of the CEA values, for the '28 cm' and '50efpd' cases respectively.

Figures 4.9 and 4.10 show respectively the flux and rating radial variations (mean values per S/A ring) for 3D calculations of the '28 cm' case. The values plotted are for both PNC and IPPE calculations, and show the percentage variation from the equivalent CEA calculations. The figures show, consistent with the 2D results, that the center-to-edge tilt remains significantly greater in the CEA calculations than in the others. Comparing the PNC and IPPE 3D results; whilst the fluxes are within 1% of each other, the ratings differ by up to 3%. Figure 4.11 shows the same information as Figure 4.10 (the difference of radial rating from CEA values), but for 2D rather than 3D calculations: the size of radial rating tilt is approximately the same as for the 3D calculations, though there are differences in the detailed structure.

Table 4.1 Keff variation with model geometry and number of energy groups (PNC calculations)

Core Configuration	Modelling Options		
	2D (CITATION) 70 groups	2D (CITATION) 7 groups	3D (MOSES) 7 groups
‘All Fuel’	1.05575	1.05633	1.05034
‘No Rods’	1.00711	1.00773	1.00370
‘28 cm’	0.98546	0.98617	0.98569
‘50 efpd’	0.97777	0.97826 (0.97812 , 90 z)	0.97932

Table 4.2 1-group cross-section data (PNC calculations)

Case and Region	Cross-section				
	Absorption	Nu*Fission	Fission	Total	Diffusion
<u>'All Fuel'</u>					
inner core	5.514e-3	6.581e-3	2.257e-3	2.8441e-1	1.3861
lower blanket	4.494e-3	5.732e-4	2.168e-4	3.3275e-1	1.1672
guide tube	5.398e-4	0	0	1.8832e-1	2.3581
outer core	5.768e-3	7.816e-3	2.671e-3	2.7590e-1	1.4292
radial blanket	5.688e-3	7.568e-4	2.861e-4	3.5834e-1	1.0525
shield	2.143e-3	0	0	3.9278e-1	1.0735
upper blanket	4.494e-3	5.732e-4	2.168e-4	3.3275e-1	1.1672
<u>'No Rods'</u>					
CSD follower	3.056e-4	0	0	1.5351e-1	2.7118
diluent	1.306e-3	0	0	3.7295e-1	1.2183
DSD follower	1.951e-4	0	0	1.3319e-1	3.1313
inner core	5.648e-3	6.668e-3	2.288e-3	2.8554e-1	1.3814
lower blanket	4.624e-3	5.680e-4	2.153e-4	3.3380e-1	1.1622
guide tube	5.366e-4	0	0	1.8706e-1	2.3729
outer core	5.878e-3	7.905e-3	2.703e-3	2.7654e-1	1.4273
radial blanket	5.652e-3	7.721e-4	2.915e-4	3.5719e-1	1.0567
shield	2.150e-3	0	0	3.9191e-1	1.0757
upper blanket	4.624e-3	5.680e-4	2.153e-4	3.3380e-1	1.1621
<u>'28 cm'</u>					
CSD absorber	3.2494e-2	0	0	2.8970e-1	1.5090
CSD follower	2.914e-4	0	0	1.5108e-1	2.7483
diluent	1.226e-3	0	0	3.6246e-1	1.2464
DSD absorber	1.7624e-2	0	0	2.2724e-1	2.2767
DSD follower	1.839e-4	0	0	1.3082e-1	3.1764
inner core	5.564e-3	6.644e-3	2.279e-3	2.8354e-1	1.3897
lower blanket	4.606e-3	5.734e-4	2.172e-4	3.3312e-1	1.1648
guide tube	5.299e-4	0	0	1.8596e-1	2.3847
outer core	5.812e-3	7.888e-3	2.696e-3	2.7492e-1	1.4346
radial blanket	5.628e-3	7.796e-4	2.942e-4	3.5653e-1	1.0590
shield	2.086e-3	0	0	3.8898e-1	1.0876
upper blanket	4.231e-3	5.976e-4	2.252e-4	3.2531e-1	1.1925
<u>'50 efpd'</u>					
axial blanket	4.442e-3	6.881e-4	2.564e-4	3.2854e-1	1.1815
CSD absorber	4.3908e-2	0	0	2.7839e-1	1.3792
CSD follower	2.909e-4	0	0	1.5089e-1	2.7505
diluent	1.222e-3	0	0	3.6135e-1	1.2493
DSD absorber	4.9664e-2	0	0	2.5917e-1	1.5483
DSD follower	1.835e-4	0	0	1.3068e-1	3.1785
bottom inner core	5.769e-3	6.699e-3	2.298e-3	2.8792e-1	1.3723
mid inner core	5.504e-3	6.598e-3	2.262e-3	2.8213e-1	1.3957
top inner core	5.464e-3	6.549e-3	2.246e-3	2.8253e-1	1.3915
guide tube	5.295e-4	0	0	1.8591e-1	2.3853
bottom outer core	5.987e-3	7.899e-3	2.701e-3	2.7909e-1	1.4170
mid outer core	5.742e-3	7.792e-3	2.663e-3	2.7372e-1	1.4398
top outer core	5.804e-3	7.804e-3	2.667e-3	2.7609e-1	1.4283
radial blanket	5.635e-3	8.323e-4	3.123e-4	3.5617e-1	1.0604
shield	2.053e-3	0	0	3.8629e-1	1.0984

Table 4.3 Comparison of PNC and CEA Keff values: 4 base Super-Phenix configurations

Core Configuration	Keff values	
	PNC Calculation	CEA Calculation
'All Fuel'	1.05034	1.07325
'No Rods'	1.00370	1.02454
'28 cm'	0.98569	0.99493
'50 efpd'	0.97932	0.98892

Table 4.4 Comparison of PNC and CEA Keff values: during 3-stage irradiation

Irradiation	CSD Insertion	Keff values	
		PNC Calculation	CEA Calculation
0 efpd	40 cm	0.97143	0.97636
~12 efpd	40 cm	0.97032	
~12 efpd	35 cm	0.97713	0.98262
~25 efpd	35 cm	0.97571	
~25 efpd	28 cm	0.98416	0.99132
~50 efpd	28 cm	0.98203	0.98892

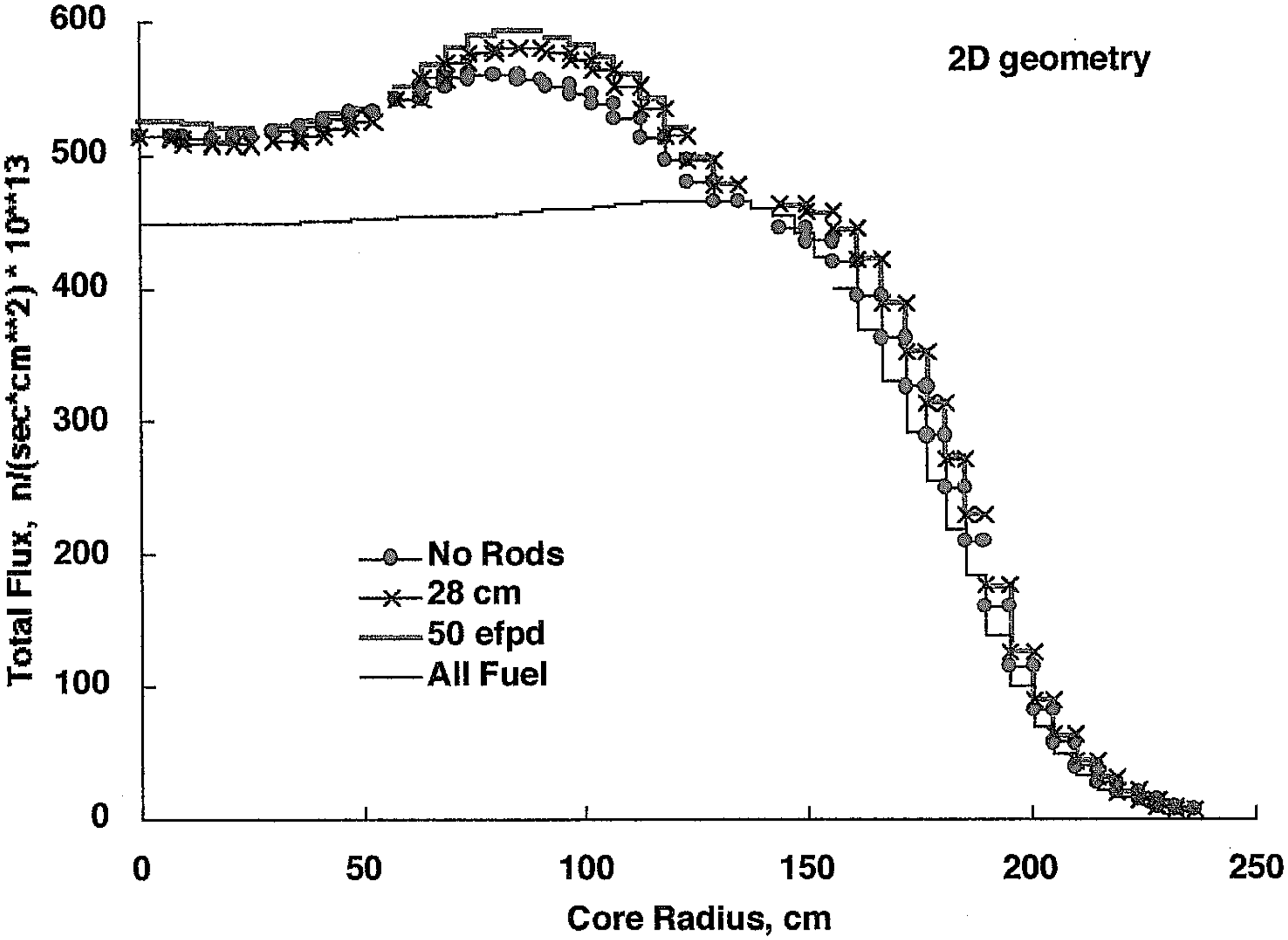

Figure 4.1 Radial flux distributions, 2D PNC calculations

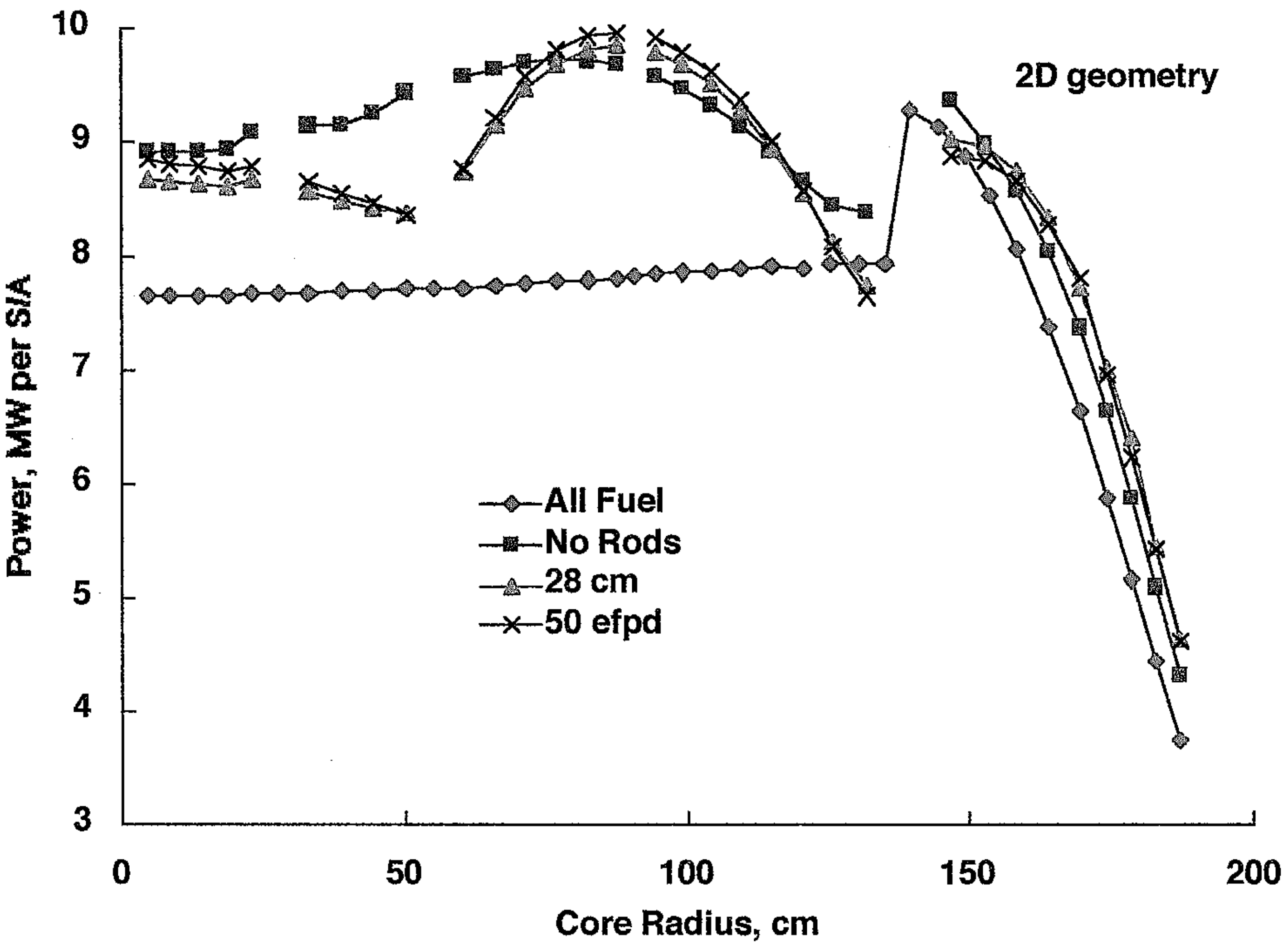

Figure 4.2 Radial rating distribution, 2D PNC calculations

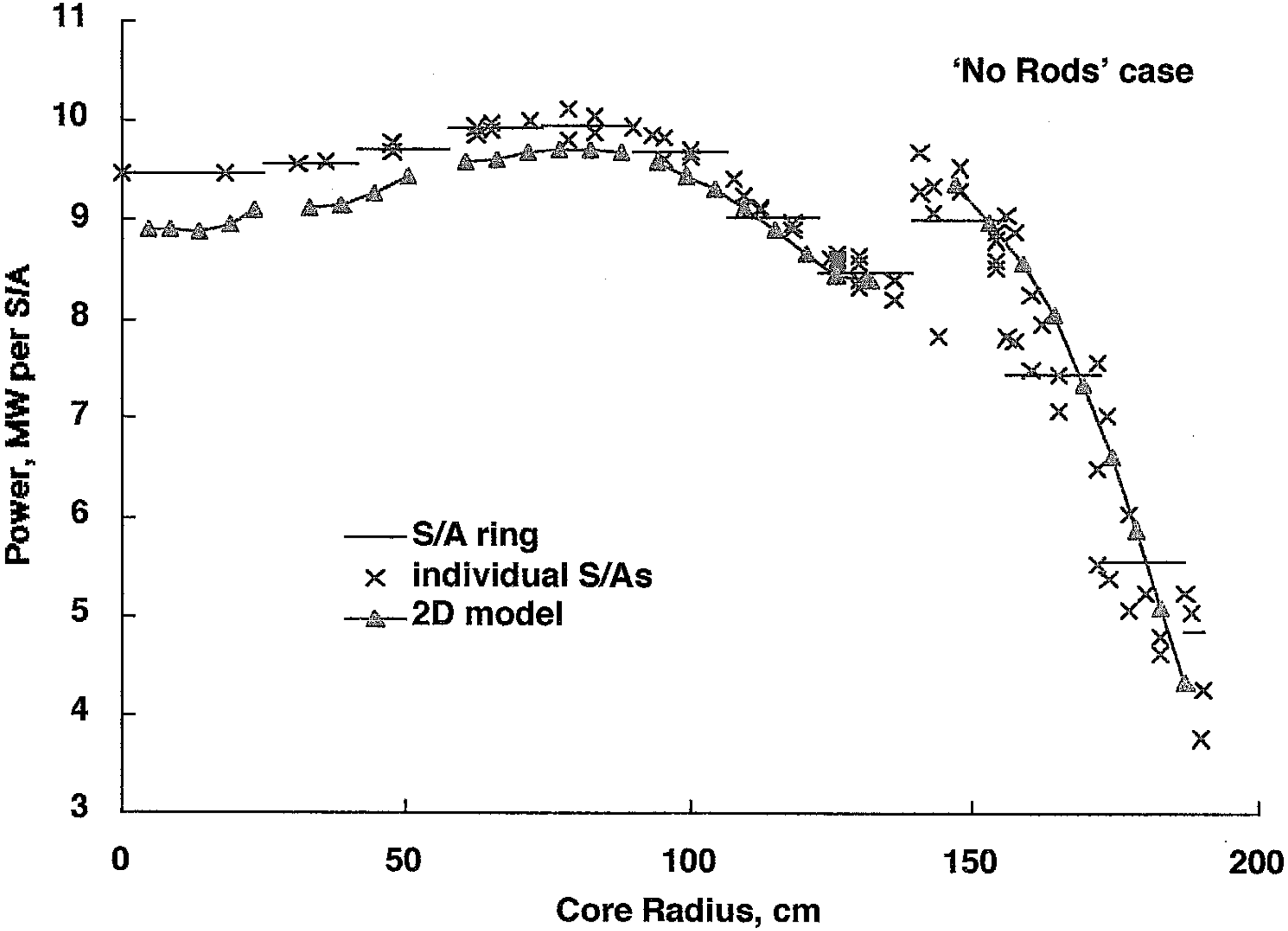

Figure 4.3 2D and 3D radial rating distributions, 'No Rods' case (PNC calculation)

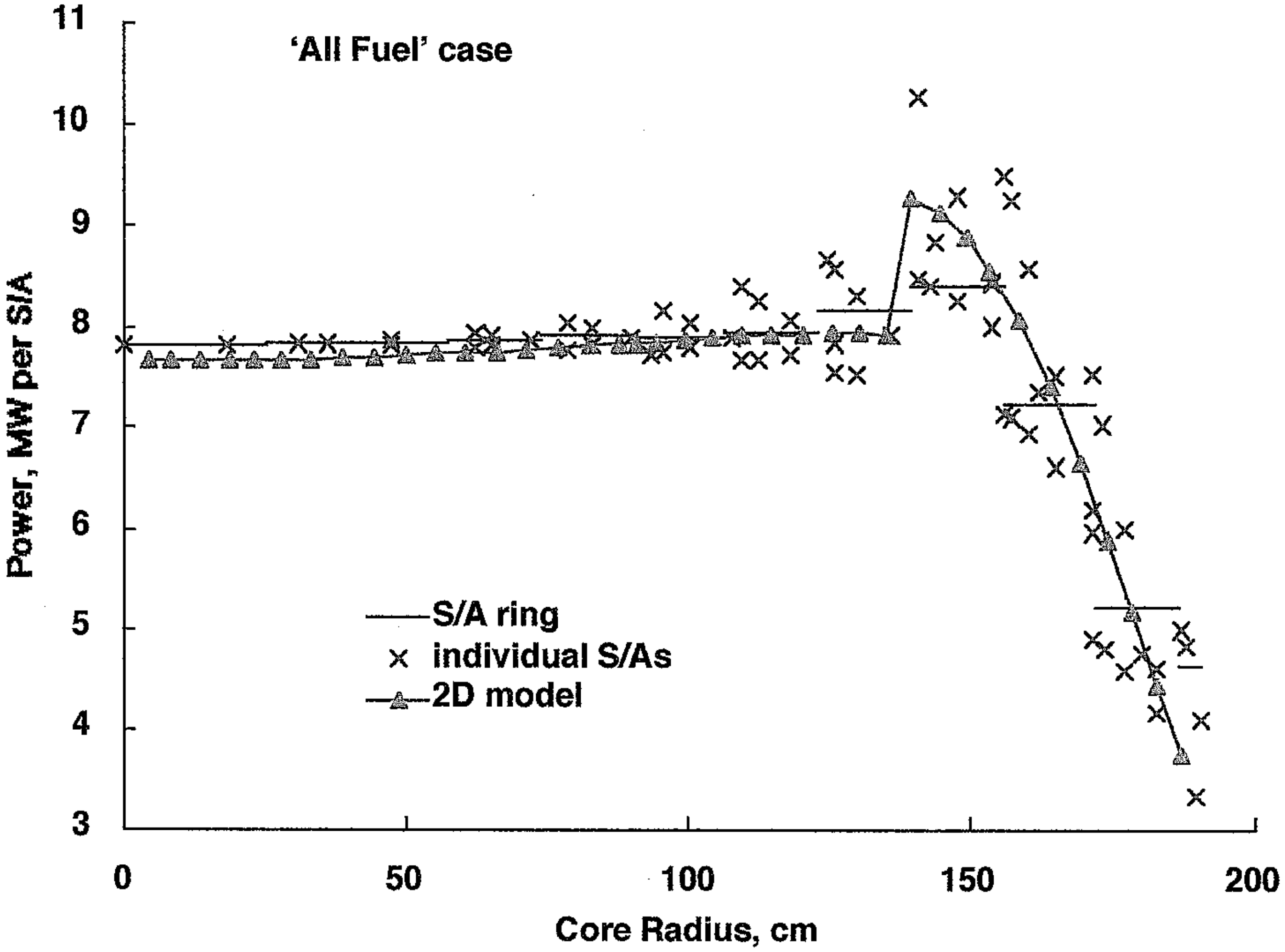

Figure 4.4 2D and 3D radial rating distributions, 'All Fuel' case (PNC calculation)

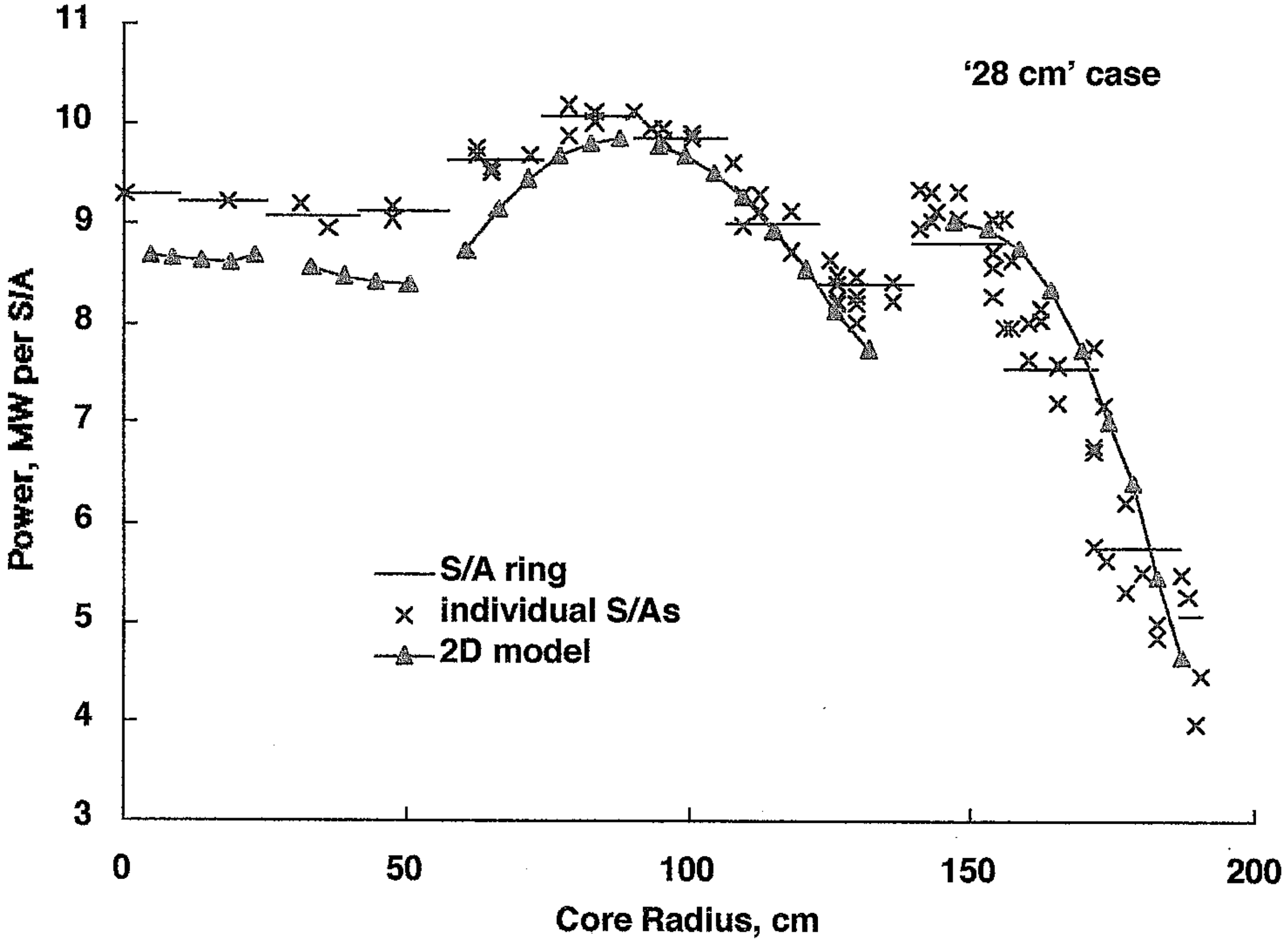

Figure 4.5 2D and 3D radial rating distributions, '28 cm' case (PNC calculation)

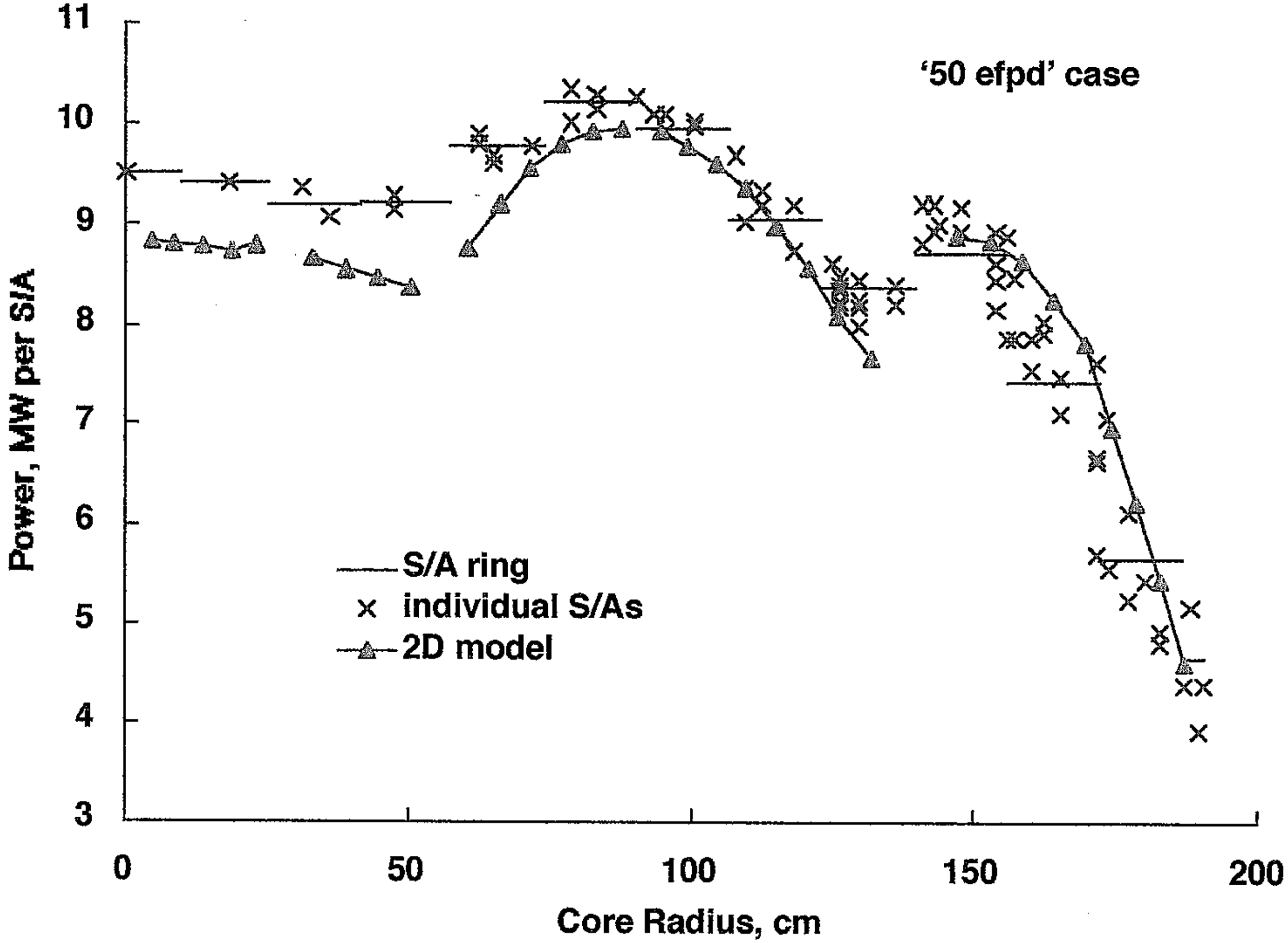

Figure 4.6 2D and 3D radial rating distributions, '50 efpd' case (PNC calculation)

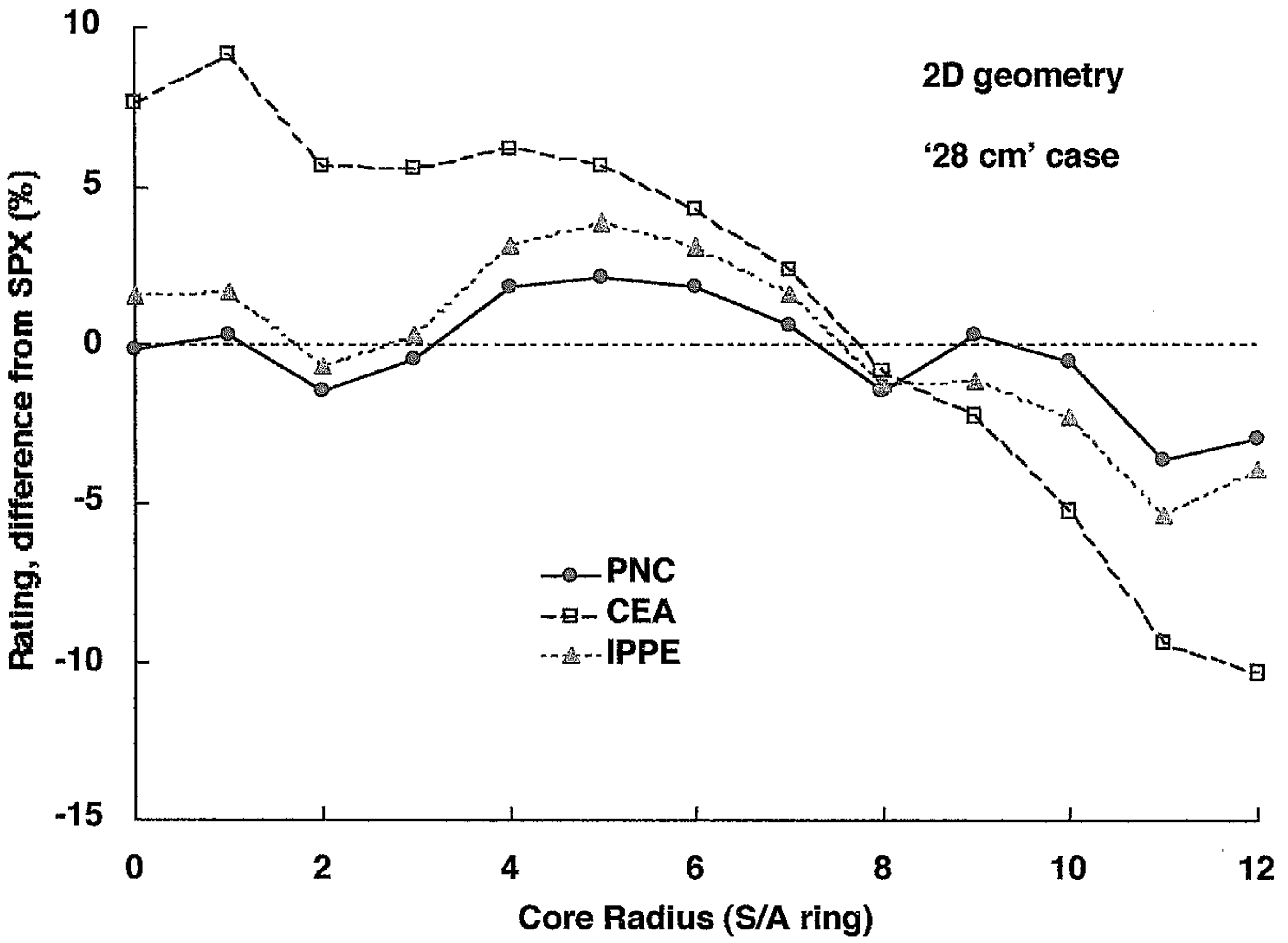

Figure 4.7 Radial rating difference from SPX measurements, '28 cm' case, 2D PNC, CEA and IPPE calculations

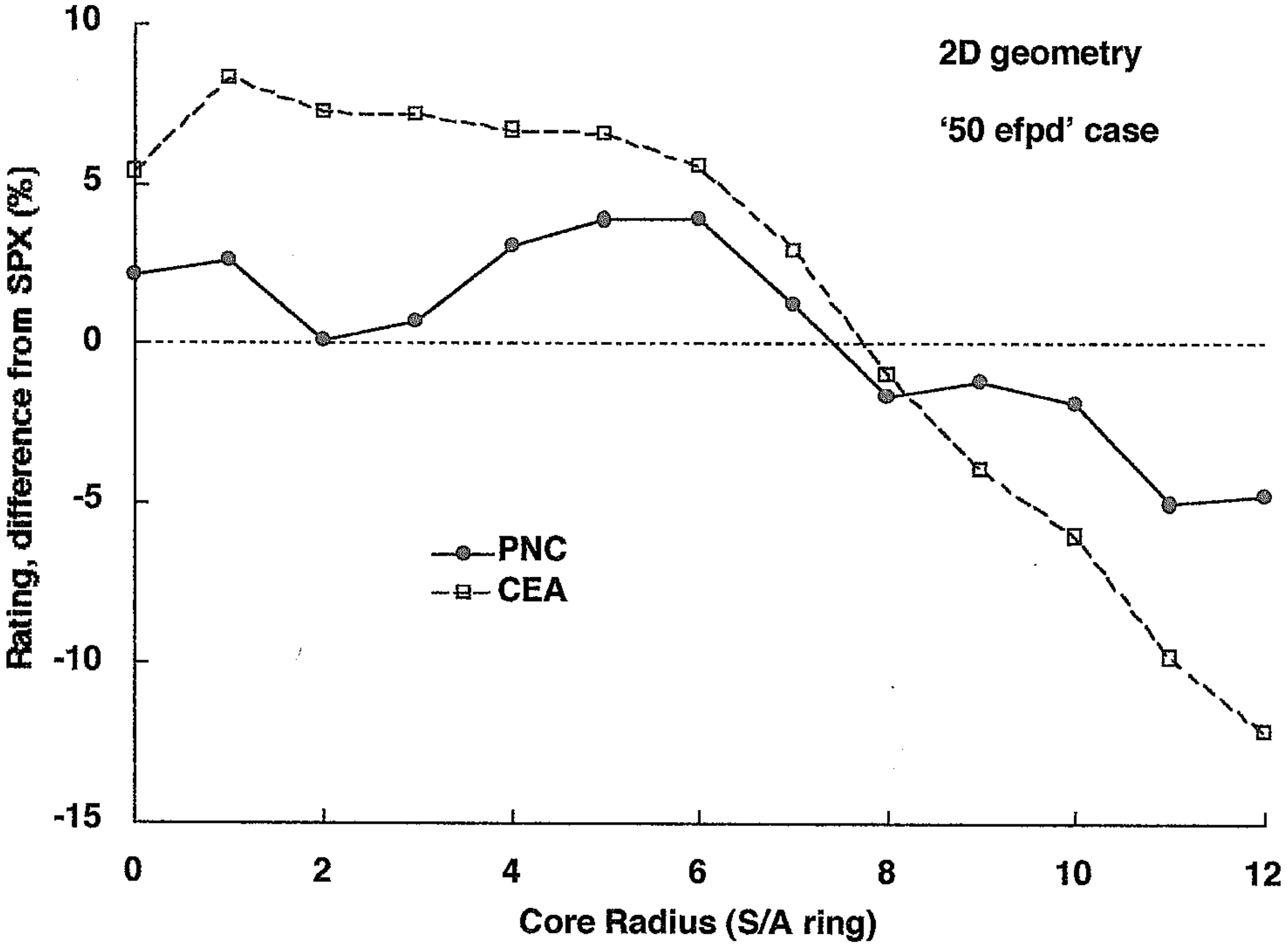

Figure 4.8 Radial rating difference from SPX measurements, '50 efpd' case, 2D PNC and CEA calculations

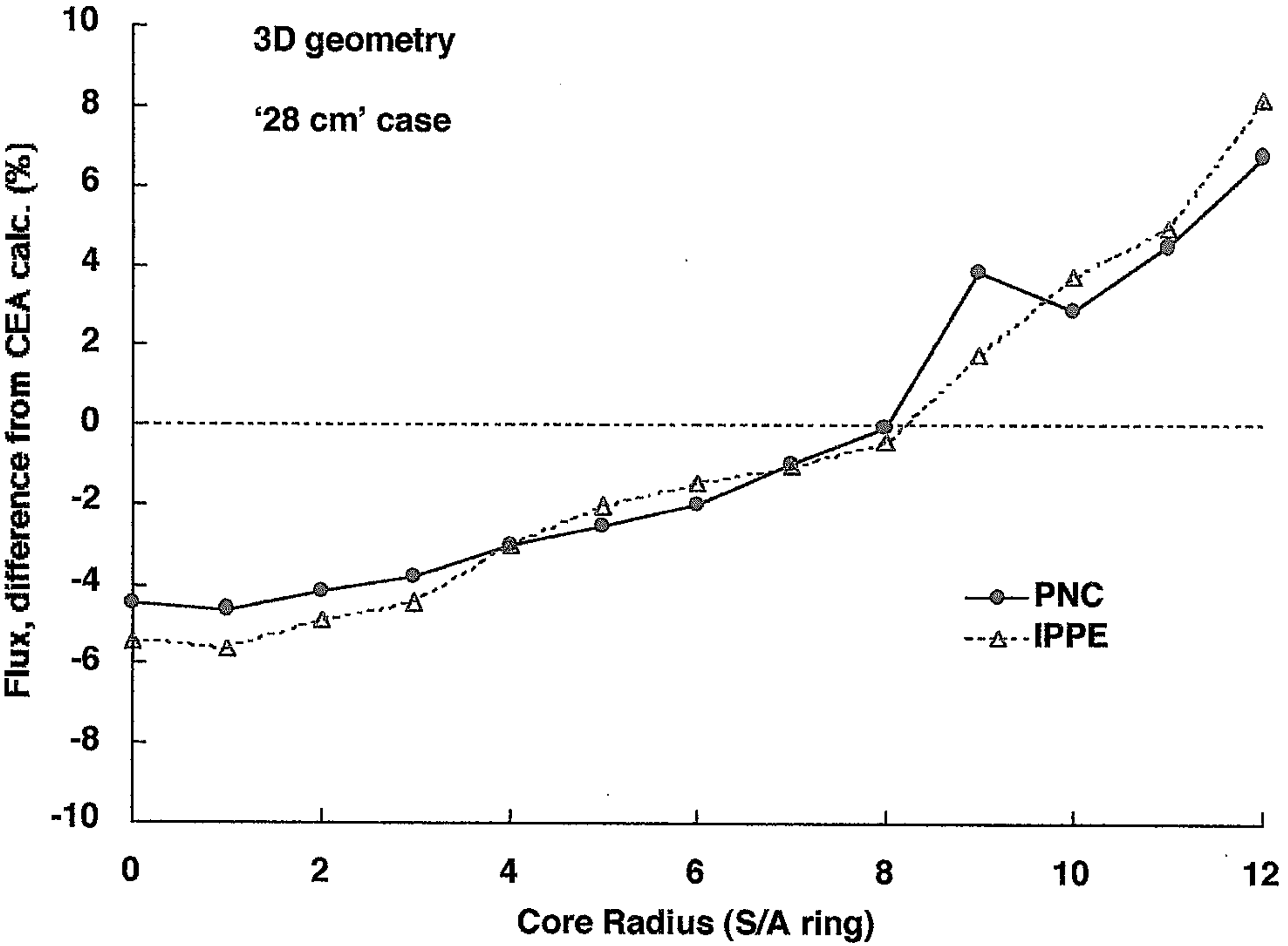

Figure 4.9 Radial flux difference from CEA calculations, '28 cm' case, 3D PNC and IPPE calculations

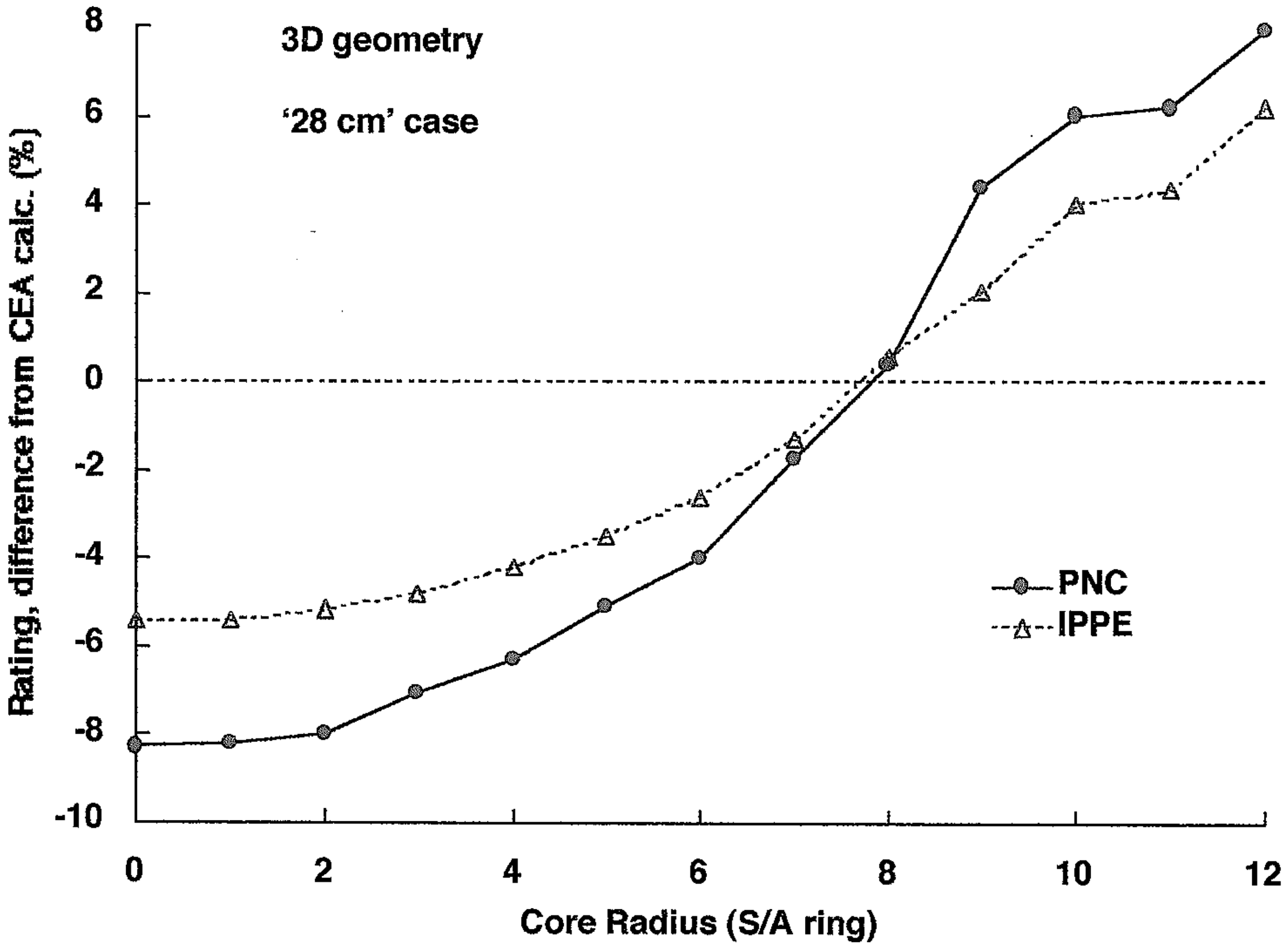

Figure 4.10 Radial rating difference from CEA calculations, '28 cm' case, 3D PNC and IPPE calculations

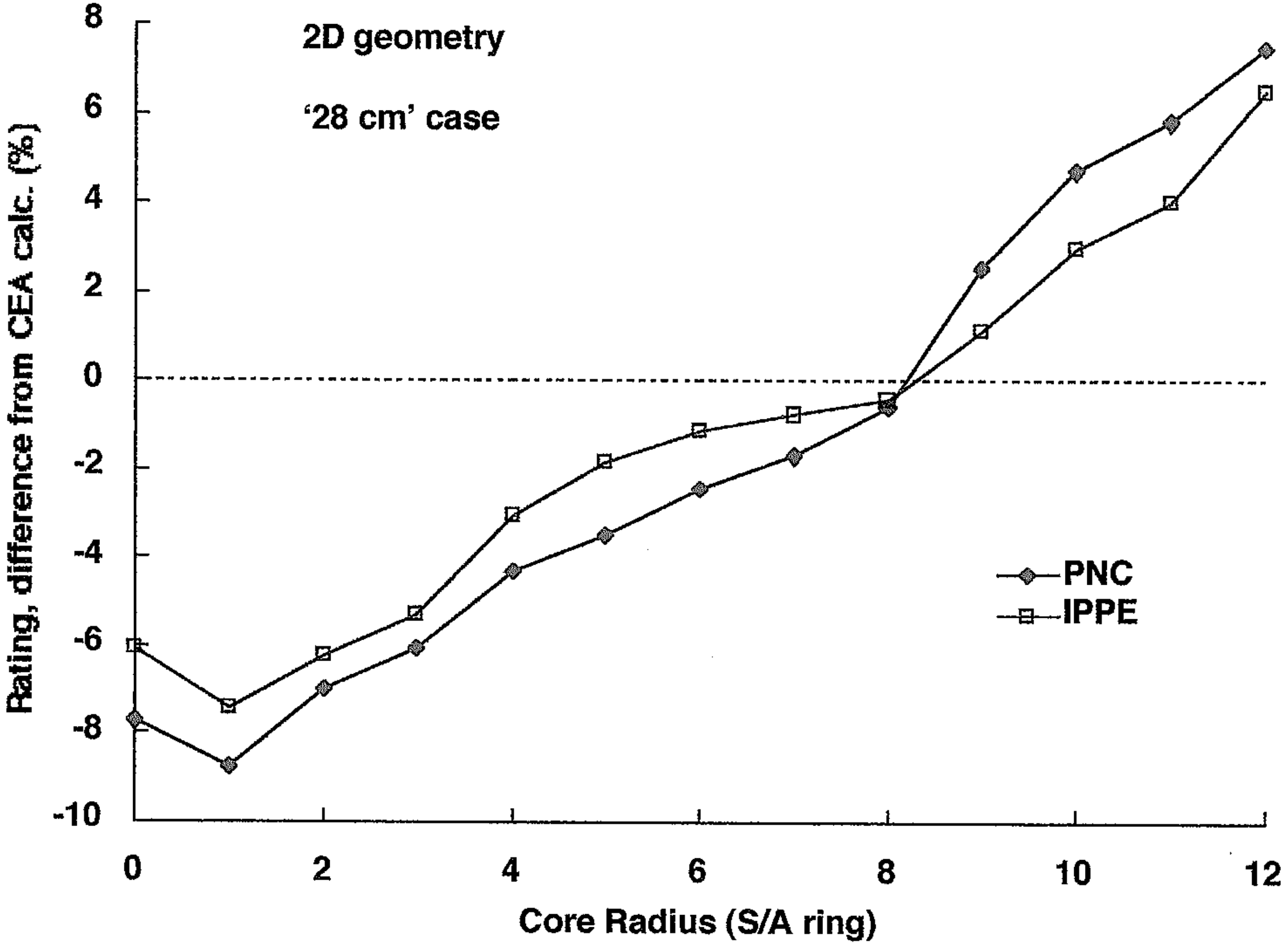

Figure 4.11 Radial rating difference from CEA calculations, '28 cm' case, 2D PNC and IPPE calculations

5 CEA ANALYSIS OF RADIAL TILT

CEA undertook an analysis of the components of the radial rating tilt effect, for one of their calculations. Only limited information on the analysis is available, summarized in this Section.

For the CEA analysis, a radial tilt parameter was defined as: the ratio of calculated to measured ratings averaged over the inner 5 S/A rings, divided by the ratio of calculated to measured ratings averaged over the outer S/A ring. Just the '28 cm' case was analysed. The calculation overestimated centre ratings by 6% and underestimated edge ratings by 12%, for a radial tilt of 1.18.

The CEA radial tilt analysis used only a 3D calculation. This calculation used a tri-Z (hex-Z, with 7 mesh points per S/A) 3D geometry for diffusion calculations, with nuclear data in 6 energy groups taken from CARNAVAL IV. The concentration of boron in the rod absorbers was reduced, as an approximate allowance for heterogeneity effects.

The CEA analysis showed that many of the approximations inherent in the calculation method contributed to the radial tilt discrepancy. An updated and improved calculation scheme was used to estimate the effect of various factors on the radial tilt. The modified calculation route used a nodal transport model, with nuclear data in 33 energy groups and taken from ERALIB-1 (which is based on JEF-2.2 data). Heterogeneity effects were modelled explicitly in the rod absorbers.

A number of other factors were identified. A correction for errors introduced by the finite mesh size. A correction for modelling fuel temperatures as uniform, rather than with a radial gradient. A correction to the SPX measurements, to allow for Na circulation above the core causing peripheral temperature measurements to be high.

Table 5.1 lists those factors which had a significant effect on the radial tilt. When all the factors were allowed for, they reduce the radial tilt by ~14%. Thus the CEA calculation with all the identified factors corrected had a radial tilt of 1.04 compared with the SPX measurements, rather than the 1.18 of the original calculation.

As Table 5.1 shows, the most significant contribution to the radial tilt effect came from the CARNAVAL IV nuclear data that was used. Of all the factors listed, only the nuclear data and the mesh size are the source of any significant difference between the PNC calculations and the original CEA calculations. Thus, it could be expected that the difference in radial tilt between PNC and CEA calculations, as in Figures 4.7 and 4.8, was primarily a consequence of the different nuclear data sources: JENDL-3.2 and CARNAVAL IV.

Table 5.1 Component factors of radial tilt effect
(CEA 3D calculation)

Effect	Radial Tilt Contribution
energy group condensation (33 to 6 groups)	+0.5%
mesh size correction	-2%
diffusion/transport model differences	-2.5%
nuclear dataset errors *	-6%
fuel temperature radial gradient	-1%
SPX thermal-hydraulics correction	-3%
Total	-14%

* estimated effect

6 NUCLEAR DATA SENSITIVITY ANALYSIS: METHOD

As was seen in the previous Section, a major cause of the difference in radial tilt between the PNC and CEA calculations was found to be the differences between the JENDL-3.2 and CARNAVAL IV nuclear data. An analysis was undertaken to determine where in the nuclear data the differences arose.

The analysis used an established PNC calculation method, based on the program SAGEP(6-1), whereby the effects on a flux calculation of changes to the nuclear dataset could be examined in detail.

The first step of the SAGEP based analysis was to define a parameter which could be used to measure the effects of changing nuclear data. It was possible to choose from a variety of parameters, including Keff and various reaction rates. Since the study was concerned with the radial rating tilt, a corresponding parameter was used: the ratio of Pu^{239} fission rates, for meshes at core axial mid-height and radii equivalent to approximately 11 and 0.5 S/A rings. The options were limited to single reaction rates; Pu^{239} was chosen because it was the main fissioning isotope. The assessed parameter can be represented as -

$$P = R_{11}/R_{0.5} \tag{1}$$

The program SAGEP uses calculations based on generalized perturbation theory. The SAGEP program calculated sensitivity coefficients, **G**, the fractional change in parameter **P** relative to the fractional change in nuclear data, for each nuclear data item -

$$G_{r,i,g} = \frac{\partial P / P}{\partial \sigma_{r,i,g} / \sigma_{r,i,g}} \tag{2}$$

r - reaction type
i - isotope
g - energy group

The next stage of the assessment was to calculate the fractional difference in each nuclear data item between the 2 datasets being compared (the dataset used in the SAGEP calculation, the PNC JENDL-3.2 data, being used as the reference value). Combining each fractional change in nuclear data with the appropriate sensitivity coefficient, **G**, gave the contribution to the fractional change in parameter **P** for each nuclear data item, as calculated by the sensitivity analysis method. These values were combined to give the overall fractional change in parameter **P**, thus -

$$\left(\frac{\Delta\sigma}{\sigma}\right)_{r,i,g} = \frac{\sigma_{r,i,g}^{CEA} - \sigma_{r,i,g}^{PNC}}{\sigma_{r,i,g}^{PNC}} \tag{3}$$

$$\frac{\Delta P}{P} = \sum_r \sum_i \sum_g G_{r,i,g} \cdot \left(\frac{\Delta\sigma}{\sigma}\right)_{r,i,g} \tag{4}$$

The calculations represented by equations (3) and (4) were evaluated using a purpose-written FORTRAN program. As well as the above equations, the program extracted the two nuclear datasets from their diverse formats and transformed them into compatible forms.

Provided that the two nuclear datasets compared are not greatly different, then the value of **$\Delta P/P$** calculated by equation (4) should be accurate. A definitive value of **$\Delta P/P$** is obtained from the fractional difference in **P** values calculated directly by flux snapshot calculations using the two different nuclear datasets.

The contributions to **$\Delta P/P$** from each individual nuclear data item are the values

$$G_{r,i,g} \cdot \left(\frac{\Delta\sigma}{\sigma}\right)_{r,i,g} \tag{5}$$

The analysis of these values identifies which of the nuclear data items are responsible for the largest contributions to the difference in radial tilt between the two nuclear datasets.

6.1 ENERGY GROUP STRUCTURE

It is necessary for the two datasets compared to have essentially the same energy group structure, if the comparison is to be meaningful. Although the PNC calculations described in Section 3 were done in either 7 or 70 energy groups, there is also a standard 18 group structure (condensed from the 70 groups) which is normally used in SAGEP calculations. The CEA nuclear data was provided in a 25 group structure.

The energy boundaries of the CEA 25 group structure did not, in general, correspond to boundaries in the standard PNC 18 group structure. Therefore, it was not possible to simply condense the CEA data to the standard 18 group PNC structure. With the exception of the maximum and minimum values (see below), the CEA 25 group energy boundaries did correspond to boundaries in the PNC 70 group structure. Therefore it was possible to define a completely new 18 group energy structure, to which it was possible to condense both the 70 group PNC data and the 25 group CEA data. This new 18 group structure was used for the SAGEP based sensitivity analysis.

The various energy group structures are shown in Figure 6.1. The extreme energies of the PNC data were 10 MeV and 10^{-5} eV, those of the CEA data were 14.5 MeV and 0.025 eV. It should be noted that, unlike the original PNC and CEA spectra, the energy groups of the new structure are to some extent irregular: groups 5,11,12 and 15 are approximately twice the size of their neighbours, and as such can be expected to be the source of larger contributions to the rating tilt.

6.2 NUCLEAR REACTION TYPES

Each of the PNC (JENDL-3.2 based) and CEA (CARNAVAL IV based) nuclear datasets provided values for a somewhat different list of nuclear data types. The PNC nuclear data items are listed in Table 6.1, and the CEA items in Table 6.2. Table 6.3 identifies those data items where a direct comparison can be made between the two datasets, and for which SAGEP calculated sensitivity coefficients.

The SAGEP sensitivity analysis normally includes, in addition to those reactions listed in Table 6.3, the (n,2n) reaction and Mu-average values. Normally the elastic and inelastic scattering matrices would be treated separately; however, since these data were combined in the CEA nuclear dataset, the PNC nuclear data and SAGEP sensitivity coefficients, **G**, were also produced in the form of a single matrix combining elastic and inelastic scattering.

Because the PNC and CEA nuclear data formats were not completely compatible, it was not possible to include a full set of reaction types in the sensitivity analysis. It was, therefore, to be expected that the sensitivity analysis would not necessarily give an accurate value for the overall fractional change in parameter **P**; it would still give a reliable calculation of the relative importance of those nuclear data items that were included in the analysis.

6.3 CALCULATIONS

The sensitivity analysis calculations were limited to just one of the four cases examined in Section 3. It was appropriate to assess a case in which all materials (i.e. including absorber) were present in the model; this restricted the choice to the cases '28 cm' and '50 efpd'. The production of all the CEA nuclear data was carried out for clean core conditions, whereas the PNC data for the '50 efpd' case took account of the changes in number density with irradiation, so the '28 cm' case was adopted for the sensitivity analysis.

PNC nuclear data in 18 groups, for use in the sensitivity analysis, was produced (for case '28 cm') in the same manner as the 7-group data used for the MOSES calculations of Section 4. The original 70-group SLAROM and 2D CITATION calculation was repeated, with the resulting flux used for the condensation to 18 groups. The CEA nuclear data included flux spectra for each material region, these were used - within the FORTRAN program written to evaluate equations (3) and (4) - to condense the CEA nuclear data to 18 groups.

The nuclear data have separate values calculated for each material region, but the SAGEP calculations of sensitivity coefficients produced values that were independent of region. It would in principle be possible to expand the equations of Section 6 to use nuclear data values which were averaged over all reactor regions (a volume and flux weighted average would seem appropriate); however, there was little variation in the nuclear data with region, so the calculations were done using nuclear data taken from one region. No region had all isotopes represented; most of the nuclear data used was taken from the inner core zone, with that for the B_4C isotopes taken from the CSD absorber region.

For the fission spectrum, the calculation of the sensitivity coefficients differs somewhat from that of the other reaction types. Since the fission spectrum has to be normalized to a total over all energy groups of 1.0, calculating the sensitivity to a change in one value requires a corresponding adjustment to the remaining values. The size of that adjustment depends on the size of the change in the one value for which the sensitivity coefficient is calculated (i.e. on the size of $\Delta\sigma/\sigma$). Thus, a series of fission spectrum sensitivity coefficients is calculated, for different sizes of $\Delta\sigma/\sigma$.

The CEA nuclear data for the CSD and DSD absorber regions was calculated using a homogeneous cell model. To ensure data compatibility, a version of the PNC '28 cm' case in which the absorbers were modelled homogeneously (rather than heterogeneously, as in the calculations for Section 4) was used in the condensation of the 18-group nuclear data for use in the sensitivity analysis.

Table 6.1 Components of PNC (JENDL-3.2) nuclear dataset

Absorption	Inelastic
Nu*Fission	n,2n
Transport	Mu-bar
Fission	Diffusion
Total Scattering	Scattering Matrix * (in-group & downscattering)

* normally separate elastic and inelastic matrices, combined for this study

Table 6.2 Components of CEA (CARNAVAL IV) nuclear dataset

Total	Elastic,g→g+1
Capture	Elastic,g→g
Fission	n,xn
Nu*Fission	Inelastic,g→g
Fission Spectrum	DPA
Disappearance	Scattering Matrix (only downscattering)
Kerma	

Table 6.3 Nuclear data items compared in SAGEP sensitivity analysis

PNC	CEA
Fission	Fission
Nu*Fission / Fission	Nu*Fission / Fission
Absorption - Fission	Capture
Elastic + Inelastic Scattering, matrix diagonal values	Elastic,g→g + Inelastic,g→g
Elastic + Inelastic Scattering, matrix non-diagonal values	Scattering Matrix
Fission Spectrum	Fission Spectrum

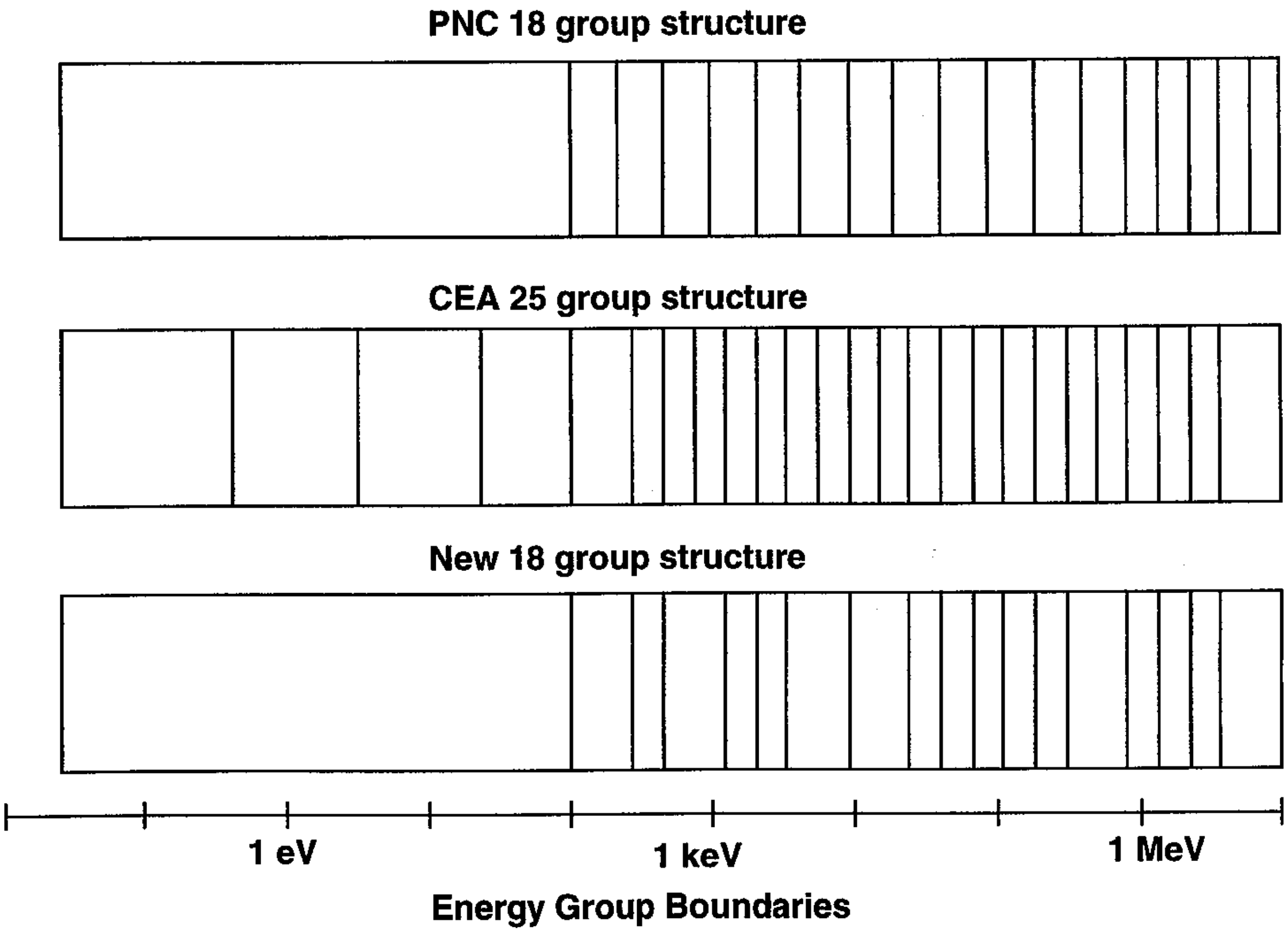

Figure 6.1 Energy group structures

7 NUCLEAR DATA SENSITIVITY ANALYSIS: RESULTS

The sensitivity calculations were carried out as described in the previous section. The SAGEP based analysis produced a value of -0.283 for $\Delta\mathbf{P}/\mathbf{P}$, the fractional difference in radial tilt resulting from the differences between the PNC (JENDL-3.2) and CEA (CARNAVAL IV) nuclear datasets. This compares with a value of -0.132 calculated directly from the diffusion calculations using the two nuclear datasets (Figure 4.7).

The above discrepancy of a factor 2 in the $\Delta\mathbf{P}/\mathbf{P}$ value was unsurprising. As is shown in Sub-section 7.3 below, there were some large differences in cross-section values between the two sets of nuclear data compared, which would compromise assumptions of linearity inherent in the perturbation theory on which the method is based. Also, incompatibilities in data formats led to some reaction types being excluded from the sensitivity analysis. As expected, these factors led to inaccuracies in the value for $\Delta\mathbf{P}/\mathbf{P}$ based on the SAGEP calculation. Despite these shortcomings, the sensitivity analysis was still considered to be accurate for the purposes of identifying which cross-sections are the most significant contributors to the $\Delta\mathbf{P}/\mathbf{P}$ value.

7.1 RADIAL TILT VARIATION, BY ISOTOPE AND REACTION

Table 7.1 shows, for each of the 21 isotopes in the model, the contributions to the $\Delta\mathbf{P}/\mathbf{P}$ value from the variation in the scattering, capture and fission reactions and in the Nu values. The values are the sum over all 18 energy groups (over the triangular 18 x 18 matrix for the scattering reaction). Table 7.2 shows the contribution to $\Delta\mathbf{P}/\mathbf{P}$ from the fission spectrum variation, again summed over all 18 groups, for different values of fission spectrum $\Delta\sigma/\sigma$.

As noted in Section 6, the values in Tables 7.1 and 7.2 were calculated using nuclear data for the inner core region (except for the B_4C isotopes, for which data were taken from the CSD absorber region). Compared with the accuracy in overall $\Delta\mathbf{P}/\mathbf{P}$ values, the variation in the individual contributions if nuclear data were taken from different regions was small - typically a maximum of ~10%.

Examining the details of Table 7.1, it is seen that the value of **ΔP/P** is dominated by a limited number of reactions: fission in Pu^{239}, capture in Fe, scatter in U^{238}, Fe, Cr, O and Na. These contributions represent ~83% of the total (considering just size, not sign); the next largest is <2%. All the important reactions are in the most common isotopes of the core materials. The total given for **ΔP/P**, from the reactions in Table 7.1, was -0.2835.

As shown in Table 7.3, the fractional difference in fission spectrum value ($\Delta\sigma/\sigma$) varies with energy group, between +0.37 and -0.45; from the results in Table 7.2 it is seen that these values correspond to a contribution from the fission spectrum to the overall **ΔP/P** value of from 0.0005 to 0.0008. These two values were based on the assumption that sensitivity coefficients obtained using the same value of $\Delta\sigma/\sigma$ were used for all 18 energy groups in the fission spectrum. If for each energy group a sensitivity coefficient was used that was based on the individual value of $\Delta\sigma/\sigma$, then the calculated contribution to the overall **ΔP/P** would be just 0.0002. The effect of fission spectrum on **ΔP/P** is negligible, the overall value being from -0.2827 to -0.2833.

7.2 RADIAL TILT VARIATION, BY ENERGY GROUP

All the results of the previous Sub-section were based on taking the effect summed over all energy groups, for each combination of reaction type and isotope. The next stage of analysing the results was to look at the greater detail of the results as a function of the 18 individual energy groups.

The contributions to **ΔP/P** as a function of energy group are shown graphically in Figures 7.1 to 7.8. For each reaction type, the figures include only those isotopes for which there are significant contributions to **ΔP/P**. All the figures are for the same vertical scale (**ΔP/P** contribution), to aid the comparison of the importance of the different reactions; in two cases - Figures 7.1 and 7.5 - single values are noted which exceed the extents of the graphs.

Figure 7.1 shows the **ΔP/P** contributions for both the fission reaction and the Nu value, for the three isotopes with the largest contributions: Pu^{239}, Pu^{240} and U^{238}. For each isotope in Figure 7.1, the fission values are shown on the left and the Nu values on the right. The only significant values are for Pu239; for the group 15 fission reaction the value goes off the scale of the figure, to -0.031.

Figure 7.2 shows the **ΔP/P** contributions for the capture reaction for a range of isotopes. The two most significant isotopes show rather different behaviours. Fe has a single large value, for energy group 15. U^{238} has several large values, but they are both positive and negative and to some extent cancel out (though this remains the most significant isotope).

Figures 7.3 to 7.7 show the **ΔP/P** contributions for the scattering reactions; since for each isotope there is a matrix of scattering reactions, only one isotope is represented in each figure. The five figures are for the most significant isotopes - U^{238}, Fe, O, Na and Cr. The figures show the combined effects of both elastic and inelastic scattering, and include both in-group (diagonal values) and down scattering. For all isotopes the major contributions to **ΔP/P** are clustered around the high energy groups, or else along the diagonal of the matrix (i.e. in-group scattering). A single value, group 5 in-group scattering for O (Figure 7.5), is off the scale of the figures (-0.025).

Figure 7.8 shows the **ΔP/P** contributions from the fission spectrum; the figure represents several sets of **ΔP/P** contributions, based on sensitivity coefficients calculated for several different $\Delta\sigma/\sigma$ values. The variation between the different cases is minimal. Examining the detail of the results, there is one large negative value, for group 5, which just about offsets a series of smaller positive contributions.

Table 7.4 lists those individual nuclear data items that produced the largest contributions (~50 items) to the overall value of **ΔP/P**. The values are such that 25% of the total is provided by just 3 nuclear data items: Pu^{239} fission for group 15, plus U^{238} and O group 5 in-group scatter. With just the 10 largest contributions over 50% of the total **ΔP/P** is produced, and just these items listed in Table 7.4 together produce nearly 80% of the total **ΔP/P**.

It is noted that the largest **ΔP/P** contributions are generally for energy group 5 or 15. These groups are twice the width of neighbouring groups (see Fig. 6.1) and so could be expected to provide double the **ΔP/P** contribution. Splitting groups 5 and 15 in two would not materially alter the conclusion that the value of **ΔP/P** is the result of relatively few reactions.

7.3 CROSS-SECTION VARIATION

The preceding analysis of the results showed that the difference in radial rating tilt (**ΔP/P**) as a result of the differences in the two nuclear datasets was dominated by the effects of a small number of nuclear data items. Some further analysis was done, to identify whether those items that contributed most to **ΔP/P** corresponded in general to the largest differences in cross-sections between the two datasets. (The alternative, which turned out to be the case, was that the small number of important nuclear data items was a consequence of there being relatively few large values among the sensitivity coefficients, **G**.)

A direct comparison was made between some of the values from the two nuclear datasets, as shown in Figure 7.9 to 7.23. Fractional differences in cross-sections (i.e. $\Delta\sigma/\sigma$ values) were plotted, but these suffered from two drawbacks. Where the PNC value was zero, no fractional difference could be calculated; so where either (or both) of the values was zero, no points were plotted in the figures. The fractional difference can lend a spurious significance to data items where the absolute values are small; to overcome this, the figures include plots of absolute differences in cross-sections.

Figures 7.9 to 7.16 show the difference in scattering cross-sections, for the four isotopes U^{238}, Cr, Fe and O. For each isotope there are fractional differences (Figures 7.9 to 7.12) and absolute differences (Figures 7.13 to 7.16) in cross-sections. Within each of the two types, the same vertical scale has been used as an aid to comparison. Several of the values are beyond the extents of the graphs (values are annotated) - the scale was chosen to allow the detail to be seen to best effect.

Of the four isotopes for which scattering fractional cross-section differences ($\Delta\sigma/\sigma$) are presented (Figures 7.9 to 7.12), that for Fe was typical of the remaining isotopes, whilst U^{238} and Cr showed some atypically large differences in the body of the matrix. The cross-section differences for O were included because one of the very largest contributions to $\mathbf{\Delta P/P}$ came from this isotope (from group 5 in-group scattering). All the cases showed significant differences along the diagonal and in the high energy region. When turning to the absolute cross-section differences ($\Delta\sigma$) of Figures 7.13 to 7.16, the complex situation is resolved, with the diagonal (i.e. in-group scattering) and near-diagonal values completely dominating all other differences. There are some individual diagonal values which are a lot higher than the rest, but these do not really correlate with the values that produced the dominant contributions to $\mathbf{\Delta P/P}$ (listed in Table 7.4): the matrix points giving large $\mathbf{\Delta P/P}$ contributions have fairly large $\Delta\sigma$ values, but there are quite a number of other matrix points with rather larger $\Delta\sigma$ values.

Figures 7.17 and 7.18 show respectively the fractional and absolute differences in fission cross-sections. The large fractional differences for Pu^{240} and Pu^{242}, at the lowest energies represented, are seen to disappear when viewed as absolute differences. However, the absolute differences are comparatively enhanced for both Pu^{239} and Pu^{241}, again just at low energies. These results were a consequence of the fission cross-section values increasing notably at low energies for the odd-numbered isotopes, and decreasing greatly for the even-numbered.

The capture cross-section fractional differences ($\Delta\sigma/\sigma$) are shown in Figures 7.19 and 7.20, and the absolute differences ($\Delta\sigma$) are in Figures 7.21 and 7.22; the figures show results for a range of 12 isotopes. For B^{10}, Mo, Mn, and the actinides, there is a general and pronounced increase in cross-sections with decreasing energy - this effect is such that it is the dominant feature of the absolute cross-section differences of Figures 7.21 and 7.22. The fractional cross-section differences of Figures 7.19 and 7.20 are much larger than the corresponding values for the fission reaction; particularly notable is one value for Na (group 8), with values well beyond the size of any other (beyond the scale used for the figures).

Figure 7.23 shows the fractional differences in Nu values. All the differences are small.

Table 7.1 Contributions to radial tilt (ΔP/P) from nuclear data differences, by isotope and reaction type

Isotope	Radial Tilt Contributions (ΔP/P)				
	By Reaction Type				Summed over All Reactions
	Fission	Nu	Capture	Scatter	
U^{235}	-.000238	-.000007	.000396	-.000310	-.000160
Pu^{238}	-.000012	-.000001	.000113	-.000046	.000054
U^{238}	.001565	-.002359	.005522	-.085643	-.080915
Pu^{239}	-.041295	.003152	.002964	-.004636	-.039815
Pu^{240}	-.002832	.001472	-.001109	-.001650	-.004119
Pu^{241}	-.001077	.000159	.000845	-.000138	-.000211
Pu^{242}	-.000463	.000120	-.000169	-.000175	-.000687
Am^{241}	.000098	-.000226	.000805	-.000273	.000403
Fe			-.017673	-.059211	-.076884
Cr			-.002453	-.013058	-.015511
Ni			-.003942	-.004950	-.008891
Mo			.002169	-.002896	-.000727
O			.000071	-.039072	-.039001
Na			.000782	-.018965	-.018183
Ti			.000626	-.000318	.000308
Cu			-.000644	-.000281	-.000925
Si			.000001	-.000982	-.000980
Mn			.001576	-.000162	.001413
B^{10}			.000720	.000625	.001345
B^{11}			.000000	.000018	.000018
C			.000000	-.000013	-.000013
Sum over All Isotopes					
Total	-.044254	.002310	-.009400	-.232096	-.283485
+ve values only	.001663	.004903	.016590	.000638	.023794
-ve values only	-.045917	-.002593	-.025990	-.232779	-.307279

Table 7.2 Contribution to radial tilt ($\Delta P/P$) from nuclear data differences for fission spectrum

Fractional Cross-section Difference ($\Delta\sigma/\sigma$)	Radial Tilt Contribution ($\Delta P/P$)
-1.0	.000273
-0.9	.000325
-0.8	.000367
-0.7	.000411
-0.6	.000455
-0.5	.000498
-0.4	.000539
-0.3	.000576
-0.2	.000615
-0.1	.000651
-0.05	.000669
+0.05	.000705
+0.1	.000719
+0.2	.000755
+0.3	.000787
+0.4	.000818
+0.5	.000847
+0.6	.000878
+0.7	.000907
+0.8	.000933
+0.9	.000959
+1.0	.000986

Table 7.3 Fractional differences in fission spectrum values

Energy Group	Fractional Fission Spectrum Difference ($\Delta\sigma/\sigma$)
1	-0.11
2	-0.05
3	-0.01
4	0.03
5	-0.45
6	0.16
7	0.20
8	0.22
9	0.24
10	0.28
11	-0.38
12	-0.32
13	0.35
14	0.15
15	0.37
16	- *
17	- *
18	- *

* both σ values are 0.0

Table 7.4 Main radial tilt ($\Delta P/P$) contributions from nuclear data differences; by isotope, reaction type and energy group

Reaction Type	Isotope	Energy Groups	$\Delta P/P$ value	Reaction Type	Isotope	Energy Groups	$\Delta P/P$ value	Reaction Type	Isotope	Energy Group	$\Delta P/P$ value
Scatter	U^{238}	$5 \rightarrow 5$	-.0157	Scatter	Fe	$5 \rightarrow 5$	-.0101	Capture	U^{238}	12	.0046
		$3 \rightarrow 5$	-.0113			$2 \rightarrow 2$	-.0080			10	-.0041
		$2 \rightarrow 5$	-.0058			$3 \rightarrow 3$	-.0067			14	.0040
		$2 \rightarrow 2$	-.0052			$3 \rightarrow 5$	-.0047			9	-.0038
		$6 \rightarrow 6$	-.0046			$4 \rightarrow 4$	-.0045			7	.0023
		$3 \rightarrow 3$	-.0044			$1 \rightarrow 1$	-.0044		Fe	15	-.0074
		$3 \rightarrow 4$	.0042			$6 \rightarrow 6$	-.0026	Fission	Pu^{239}	15	-.0308
		$7 \rightarrow 7$	-.0040		O	$5 \rightarrow 5$	-.0248			14	-.0116
		$2 \rightarrow 6$	-.0037			$4 \rightarrow 5$	-.0066			12	-.0063
		$1 \rightarrow 1$	-.0032			$1 \rightarrow 1$	-.0039			11	.0054
		$2 \rightarrow 7$	-.0032			$2 \rightarrow 2$	-.0025			4	-.0044
		$1 \rightarrow 5$	-.0031		Na	$5 \rightarrow 6$	.0043			10	.0035
		$4 \rightarrow 4$	-.0030			$5 \rightarrow 5$	-.0038			13	-.0031
		$4 \rightarrow 6$	-.0030			$4 \rightarrow 5$	-.0037			1	.0028
		$2 \rightarrow 4$	.0029			$3 \rightarrow 7$	-.0029	Nu	Pu^{239}	15	.0018
		$3 \rightarrow 6$	-.0028		Cr	$5 \rightarrow 5$	-.0023	Fission Spectrum		5	-.0067
		$3 \rightarrow 7$	-.0027		Ni	$5 \rightarrow 5$	-.0019			1	.0022
		$4 \rightarrow 7$	-.0027								

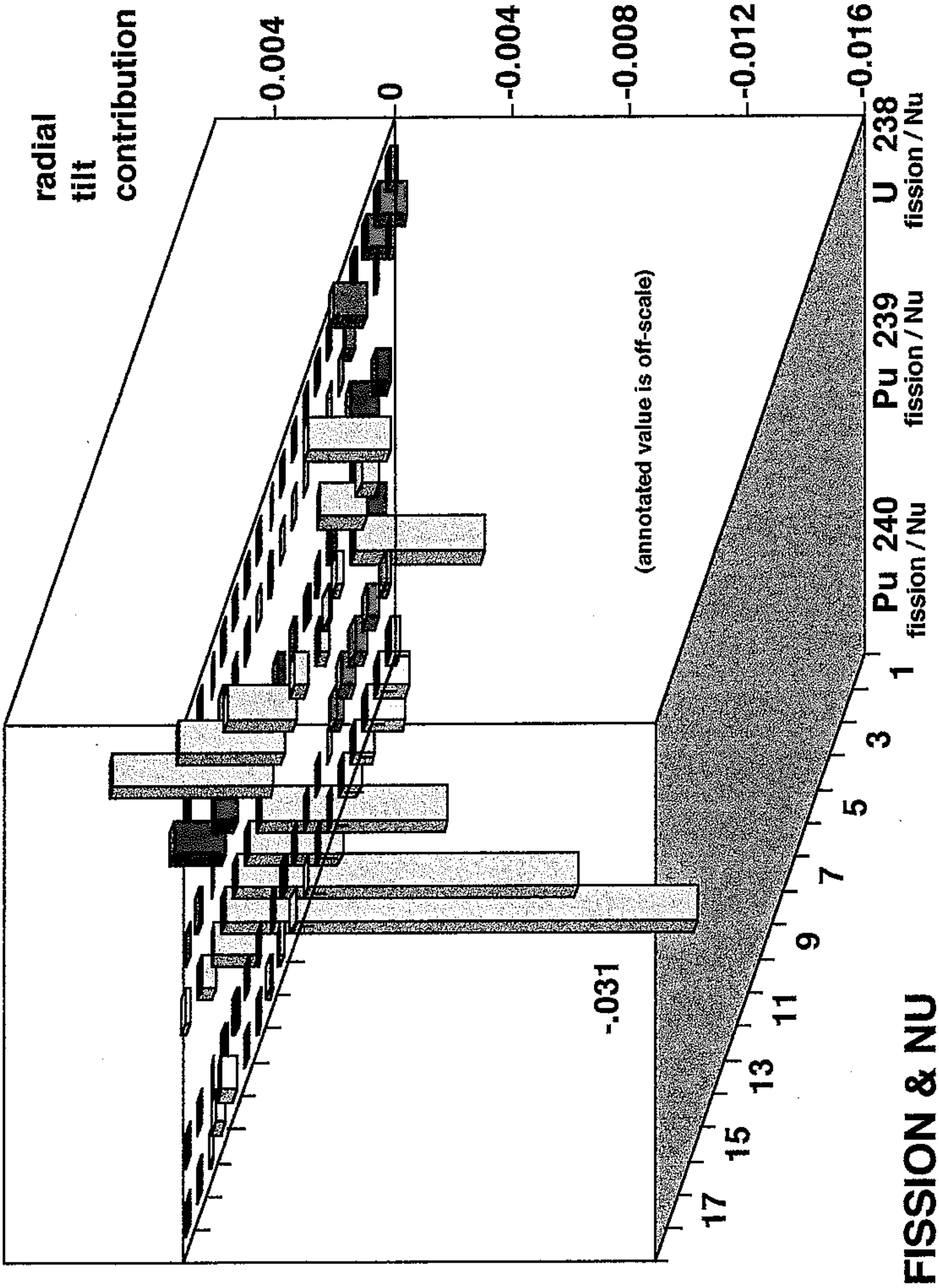

Figure 7.1 Contributions to radial tilt (ΔP/P) from fission cross-section and Nu value differences

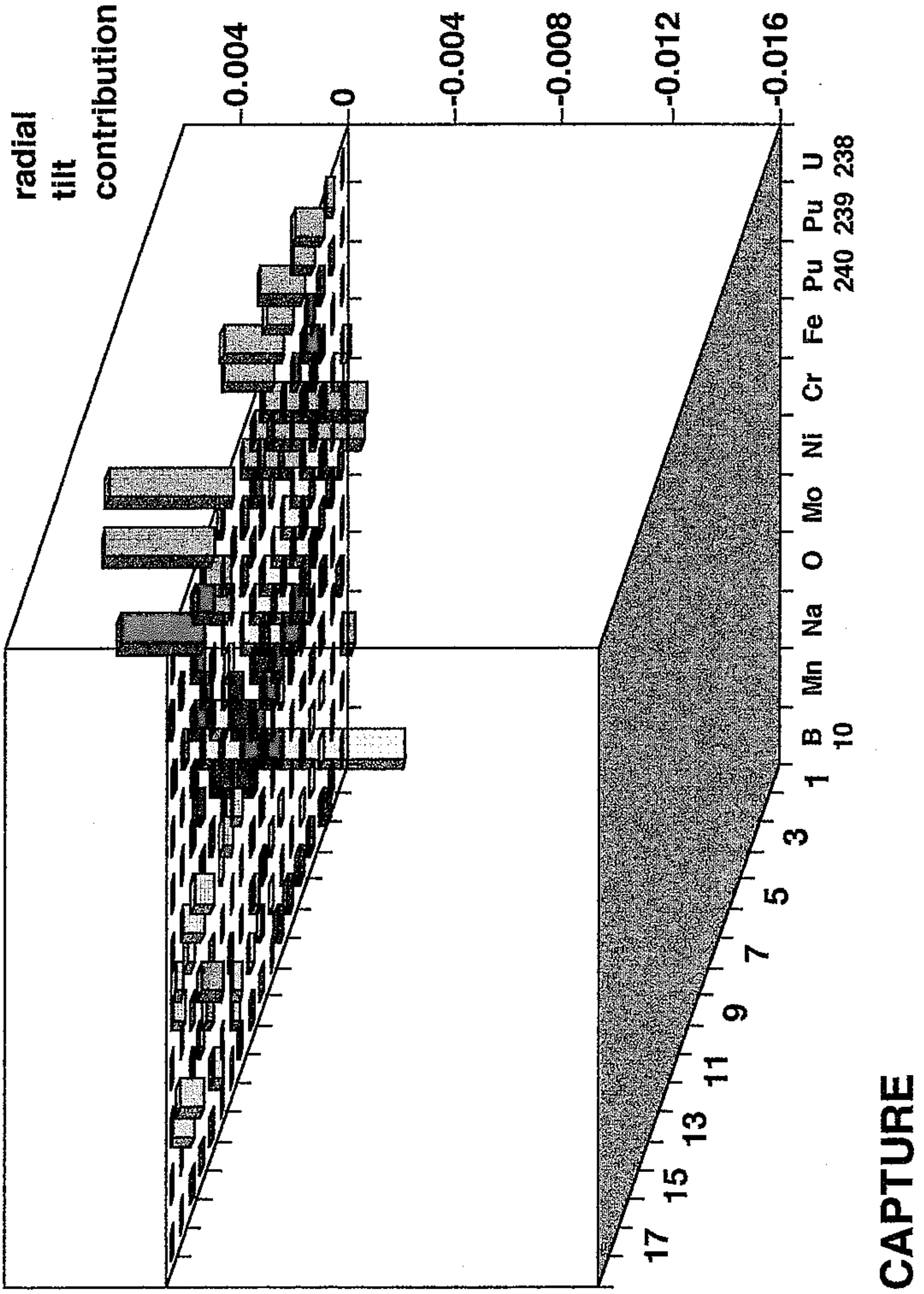

Figure 7.2 Contributions to radial tilt (ΔP/P) from capture cross-section differences

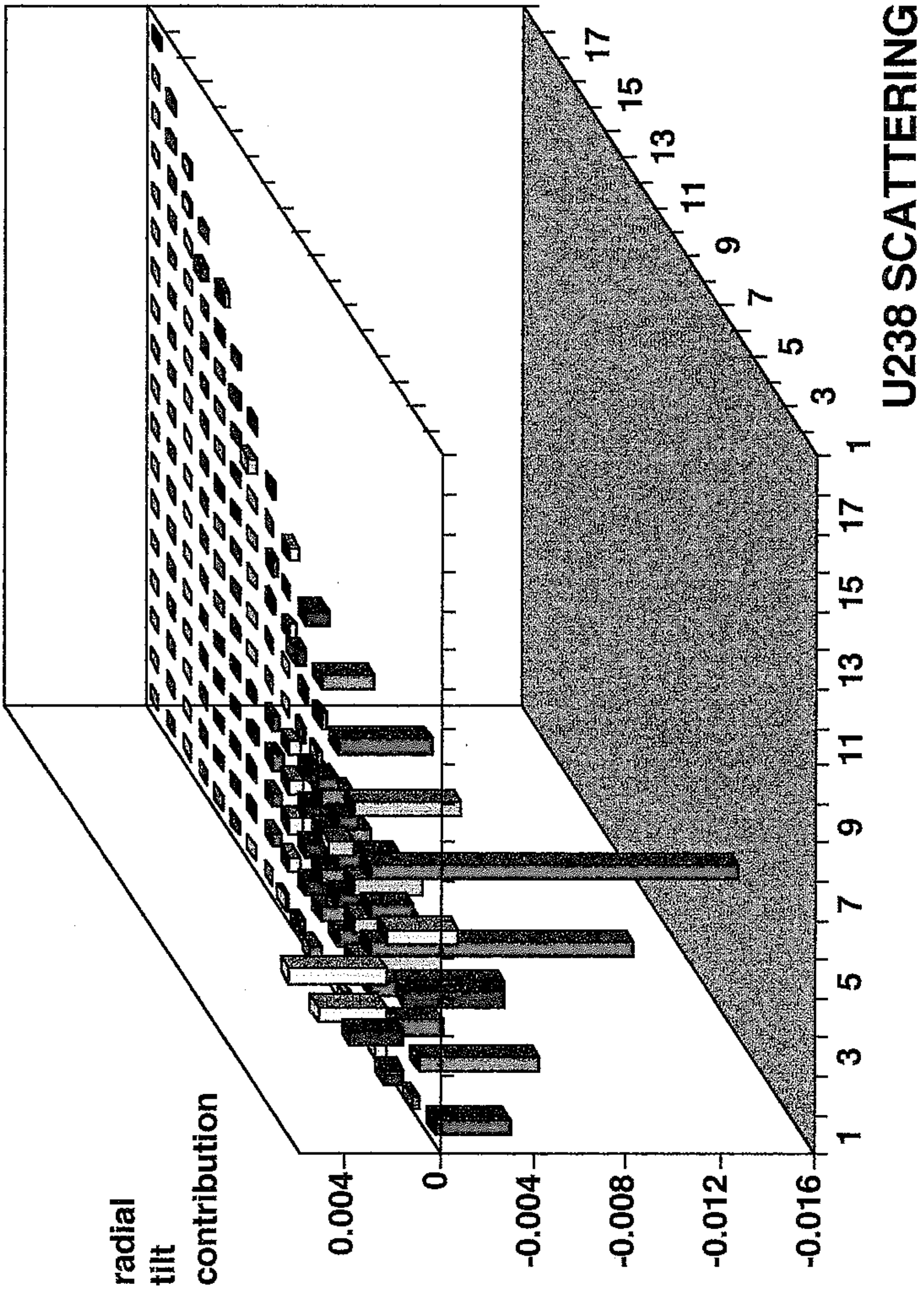

Figure 7.3 Contributions to radial tilt ($\Delta P/P$) from U^{238} scatter cross-section differences

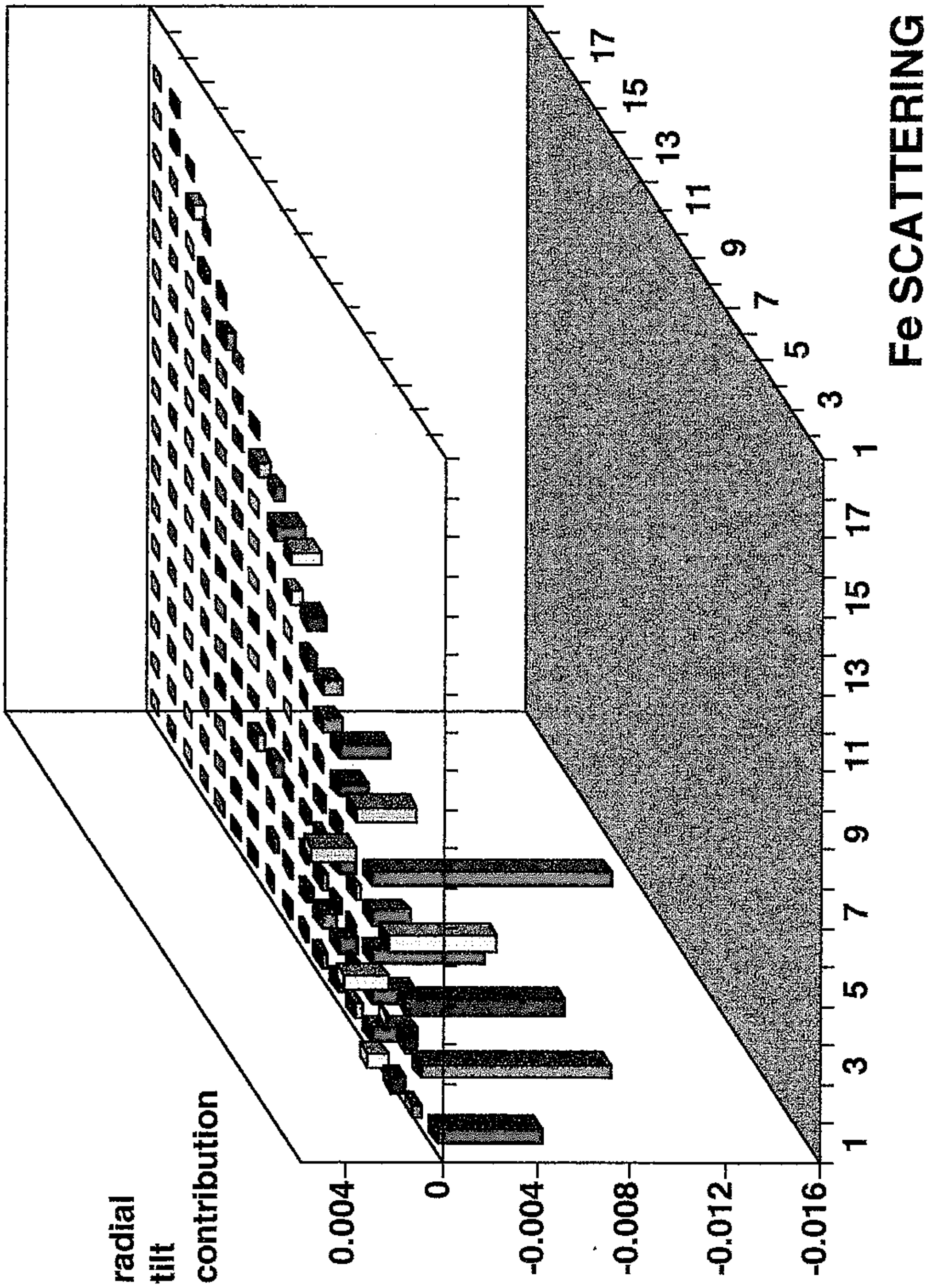

Figure 7.4 Contributions to radial tilt (ΔP/P) from Fe scatter cross-section differences

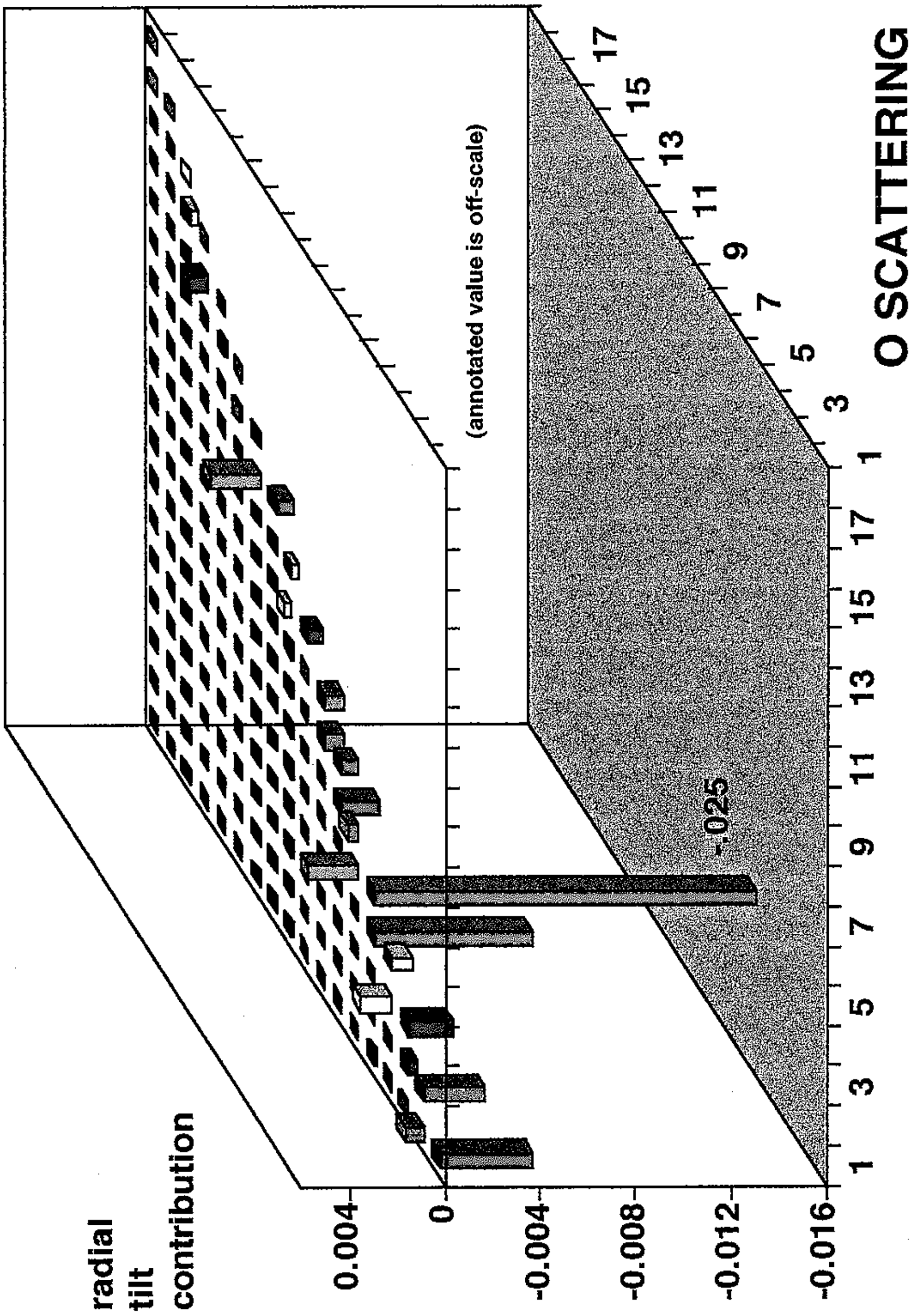

Figure 7.5 Contributions to radial tilt (ΔP/P) from O scatter cross-section differences

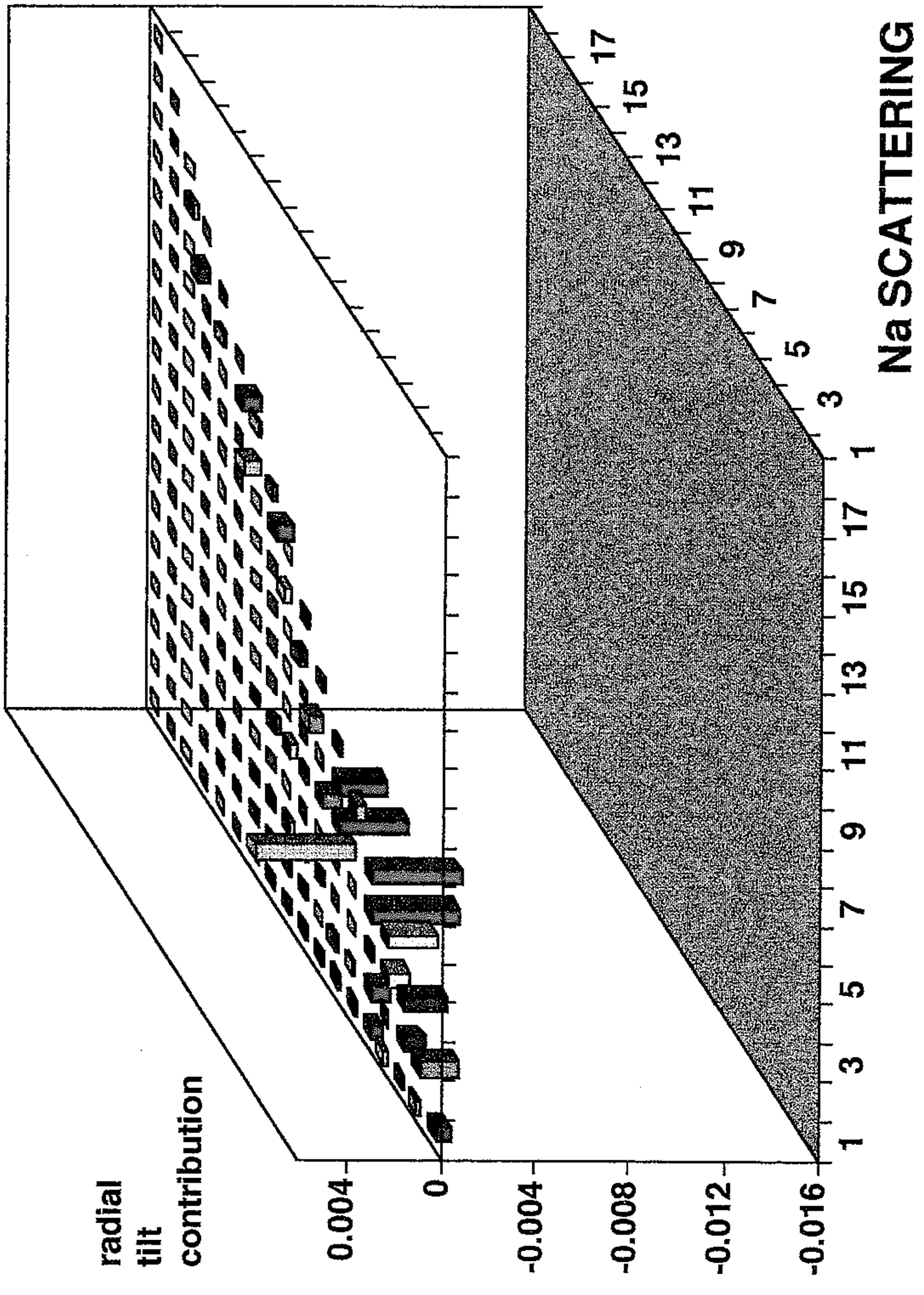

Figure 7.6 Contributions to radial tilt (ΔP/P) from Na scatter cross-section differences

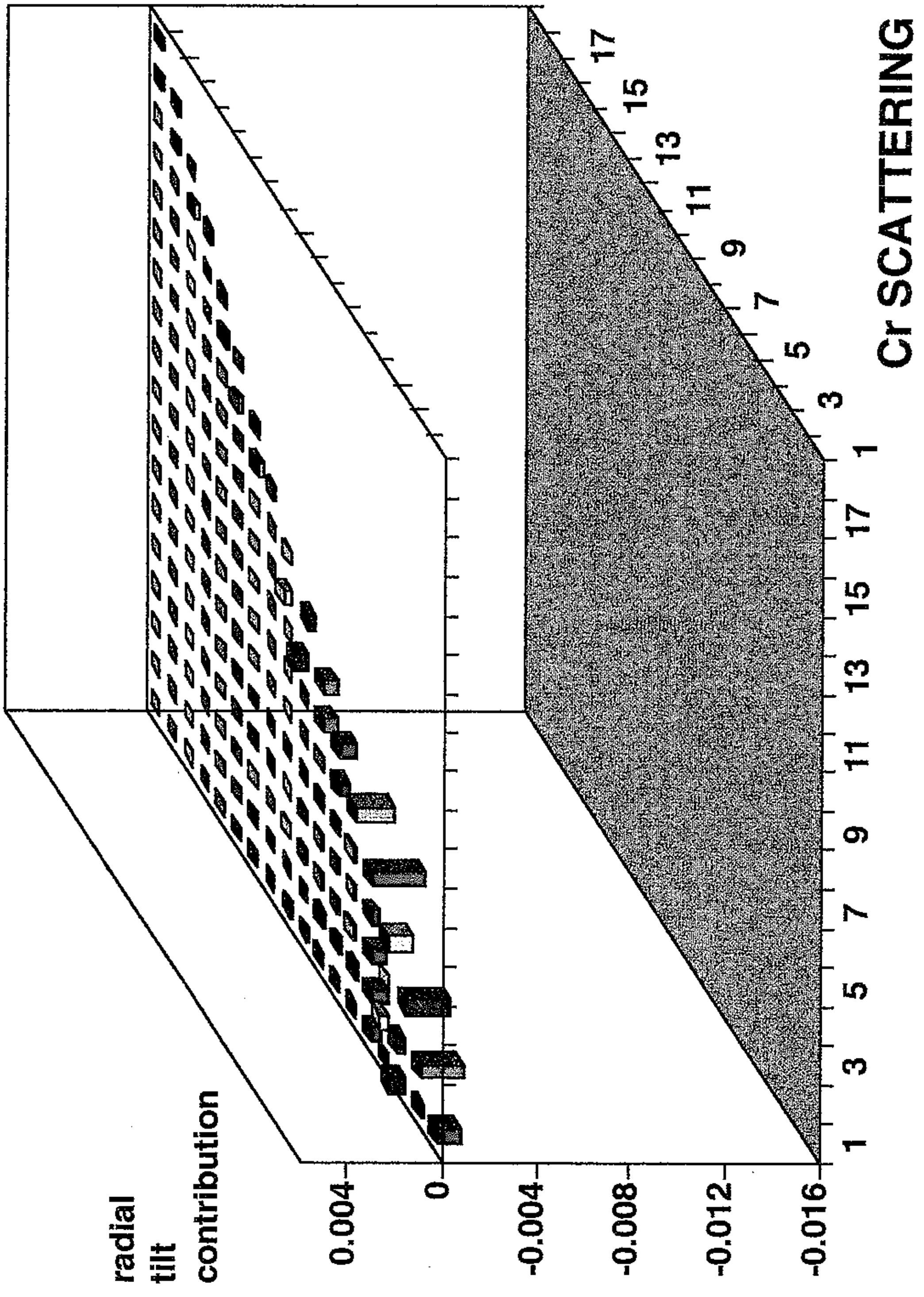

Figure 7.7 Contributions to radial tilt (ΔP/P) from Cr scatter cross-section differences

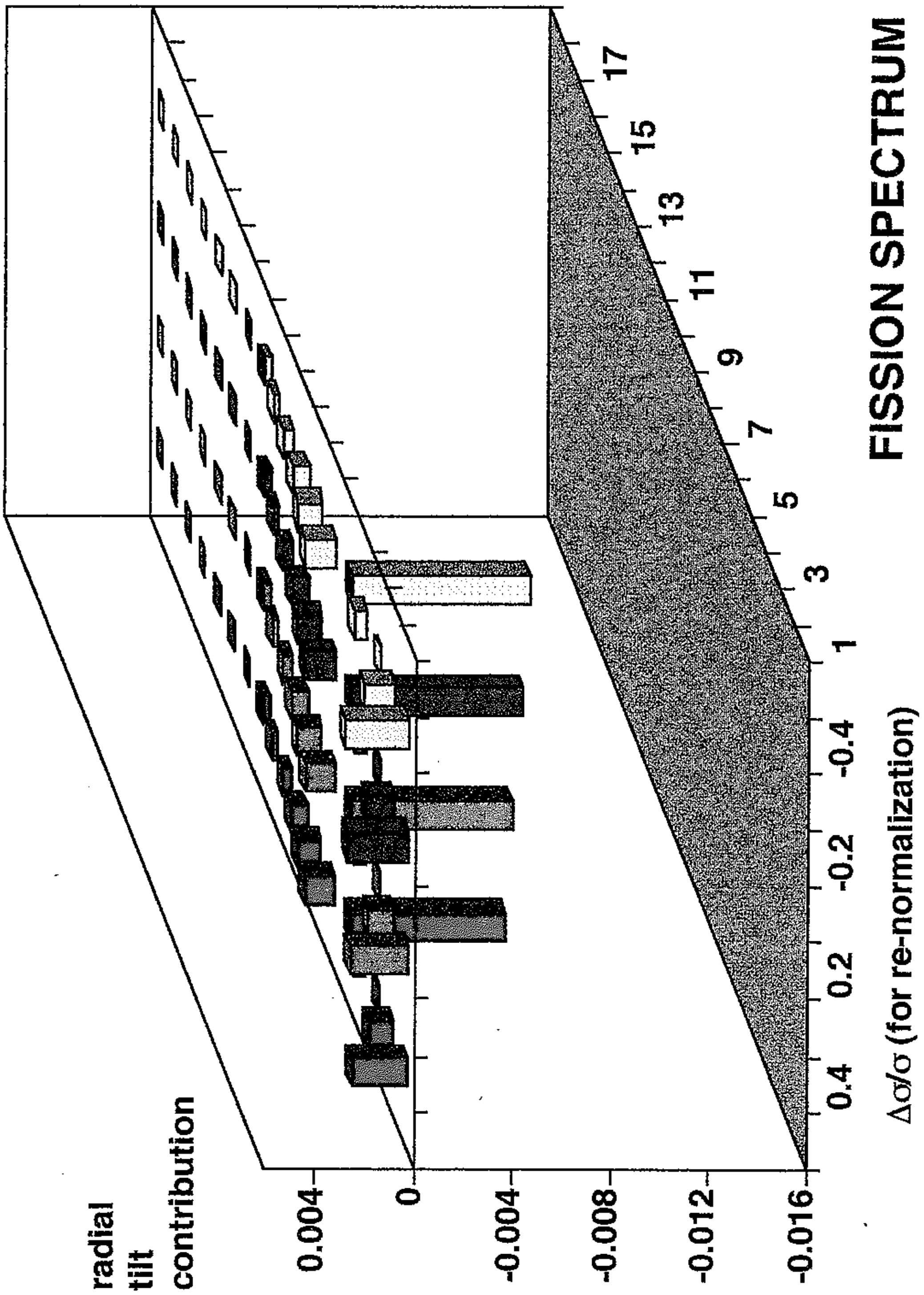

Figure 7.8 Contributions to radial tilt (ΔP/P) from fission spectrum differences

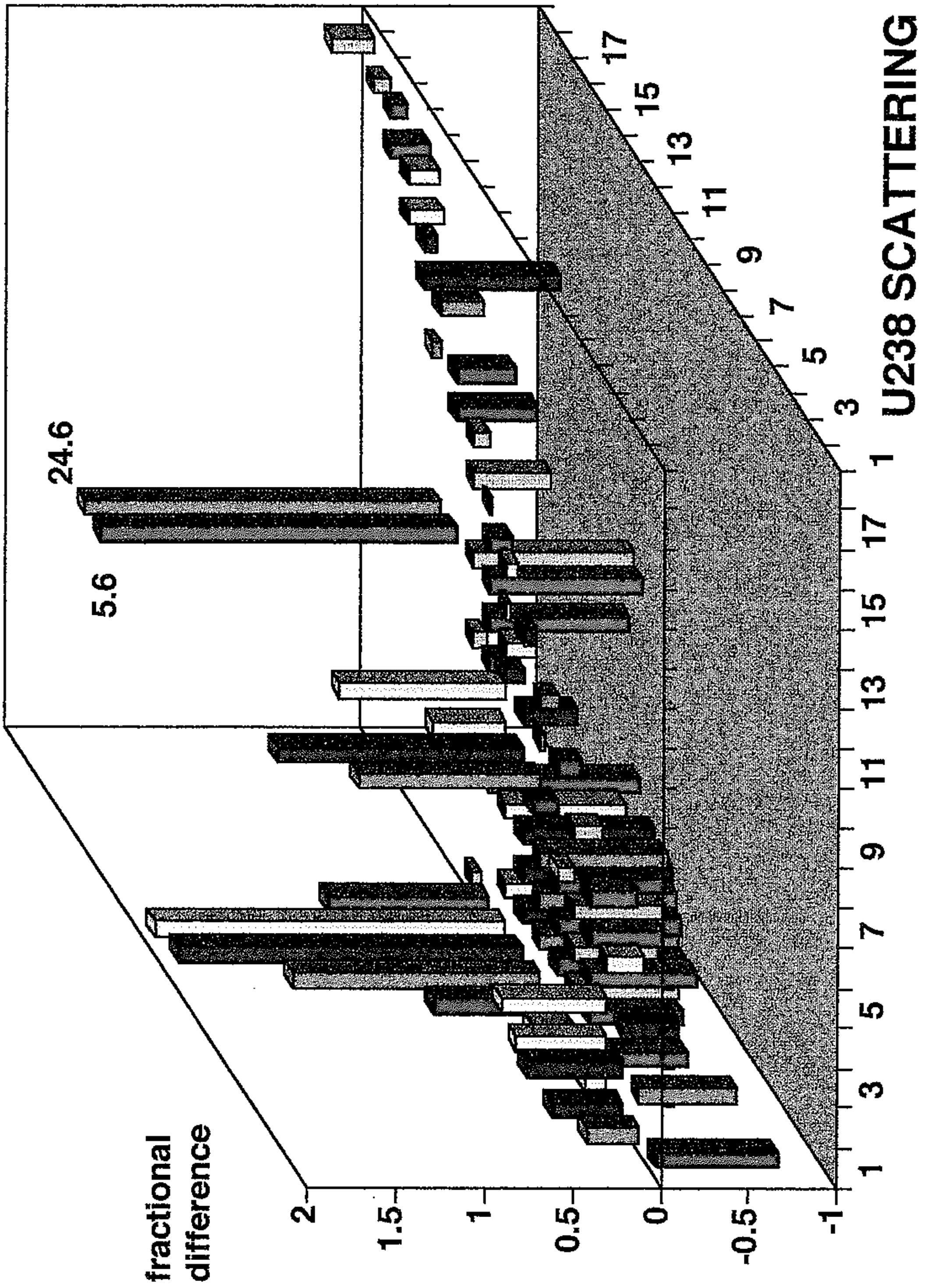

Figure 7.9 Fractional differences in U^{238} scattering cross-sections

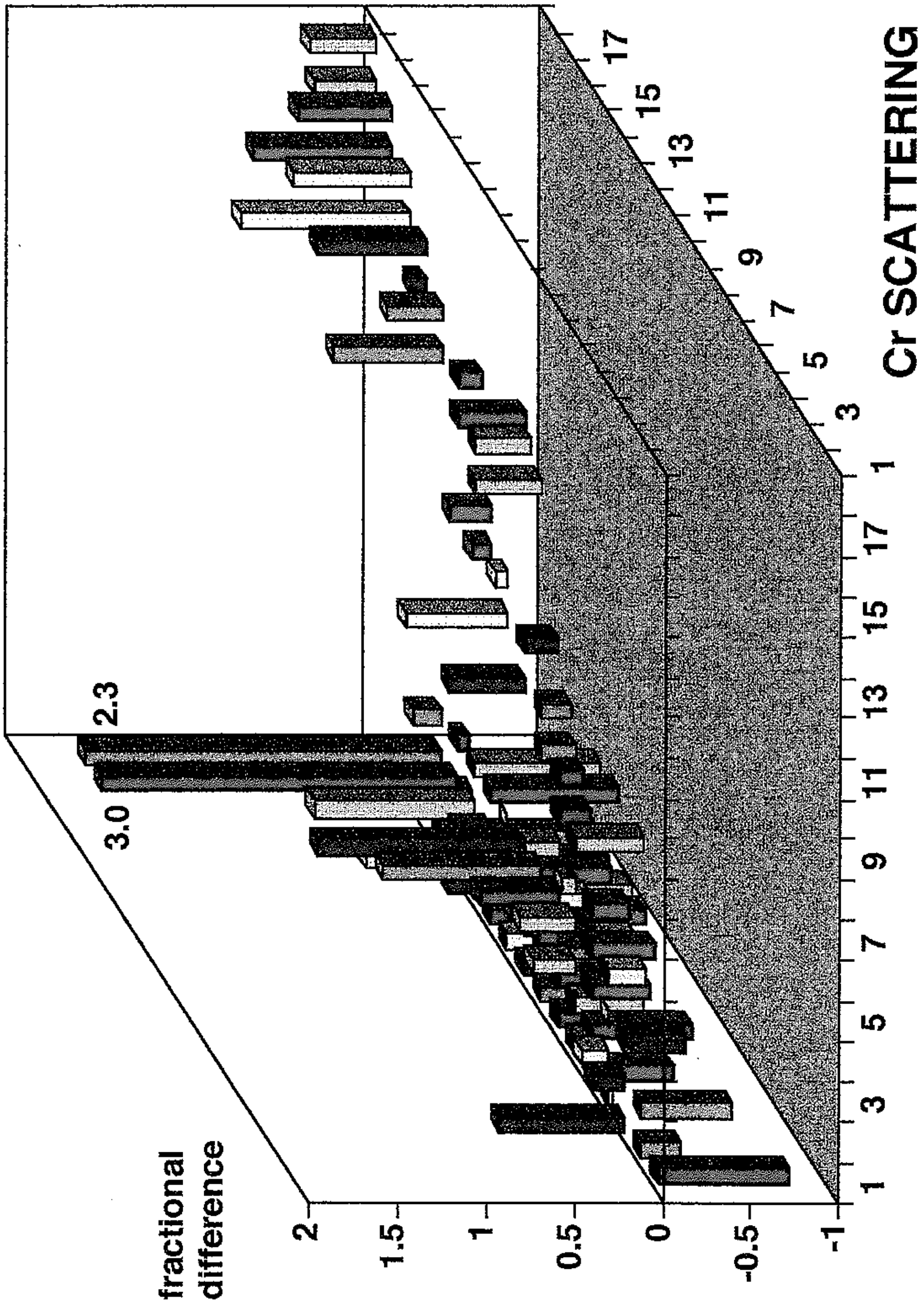

Figure 7.10 Fractional differences in Cr scattering cross-sections

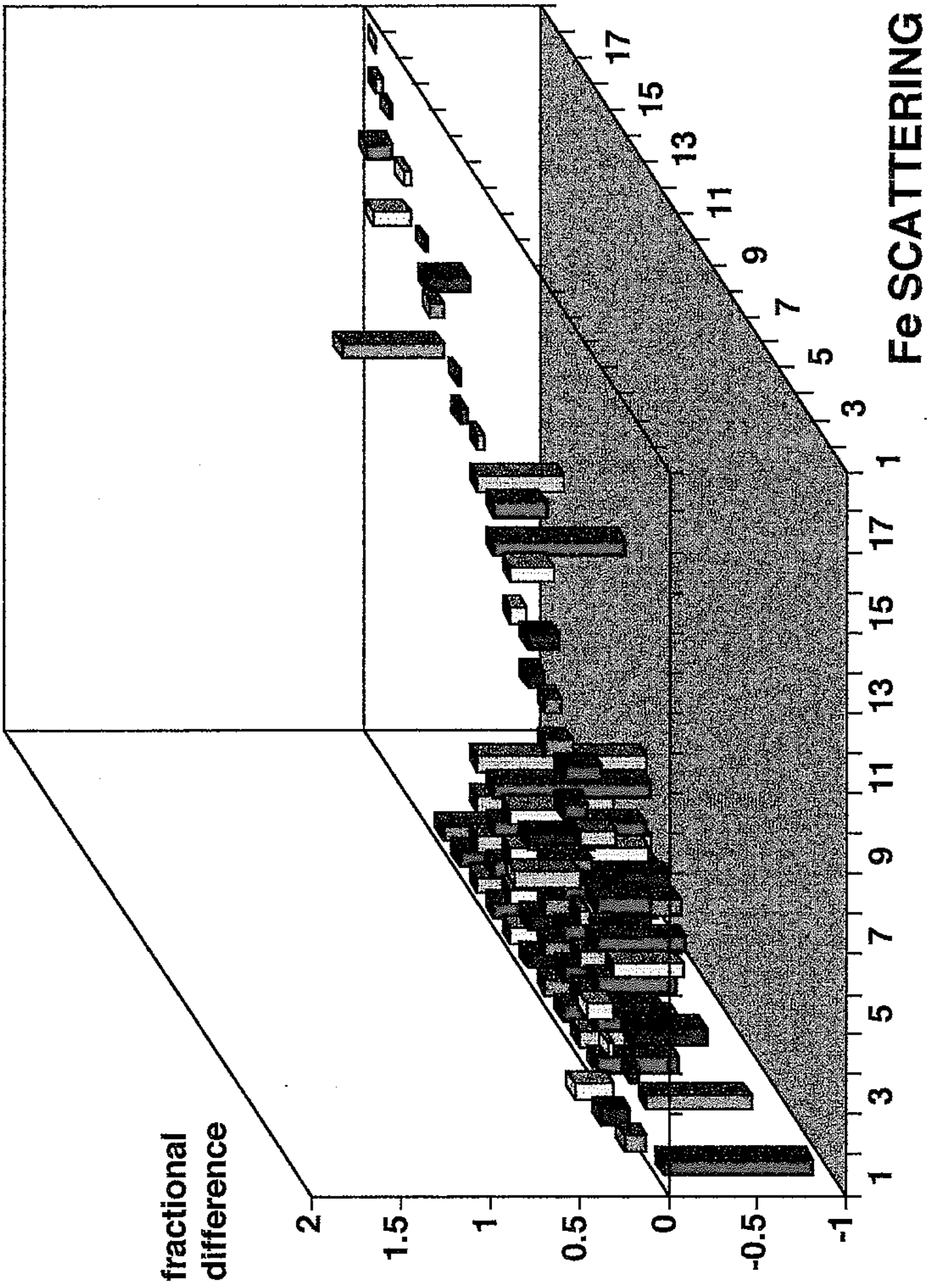

Figure 7.11 Fractional differences in Fe scattering cross-sections

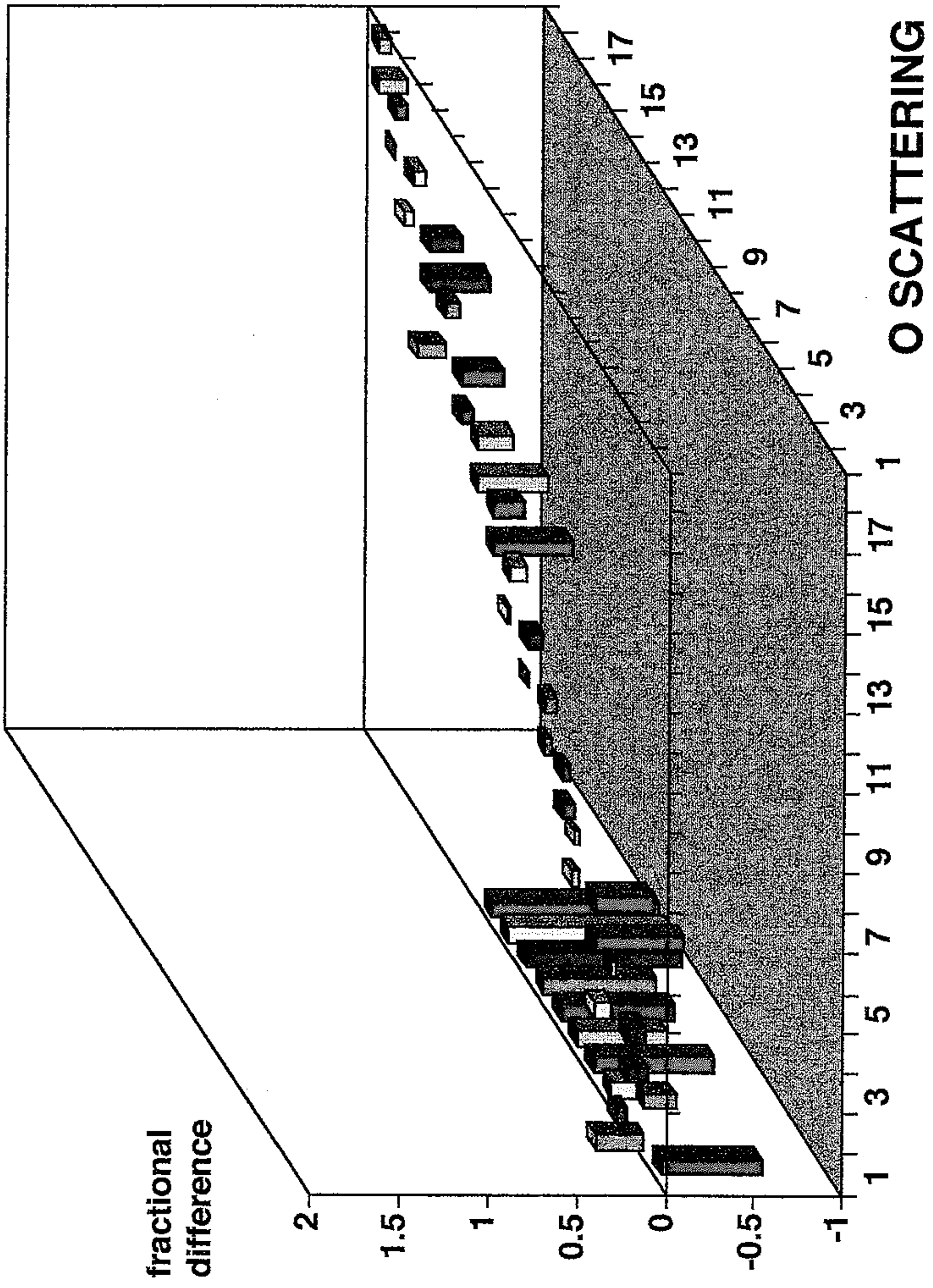

Figure 7.12 Fractional differences in O scattering cross-sections

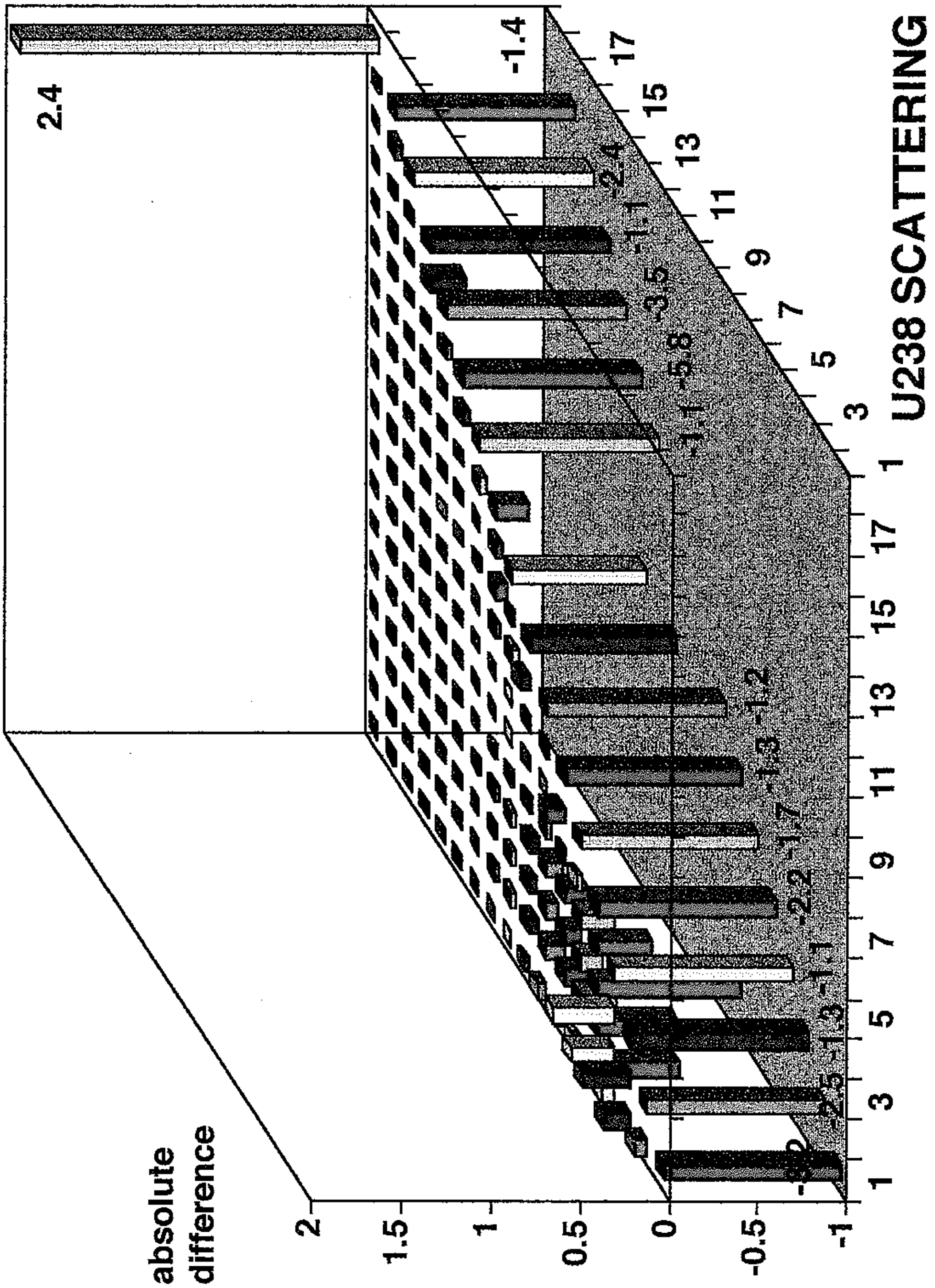

Figure 7.13 Absolute differences in U^{238} scattering cross-sections

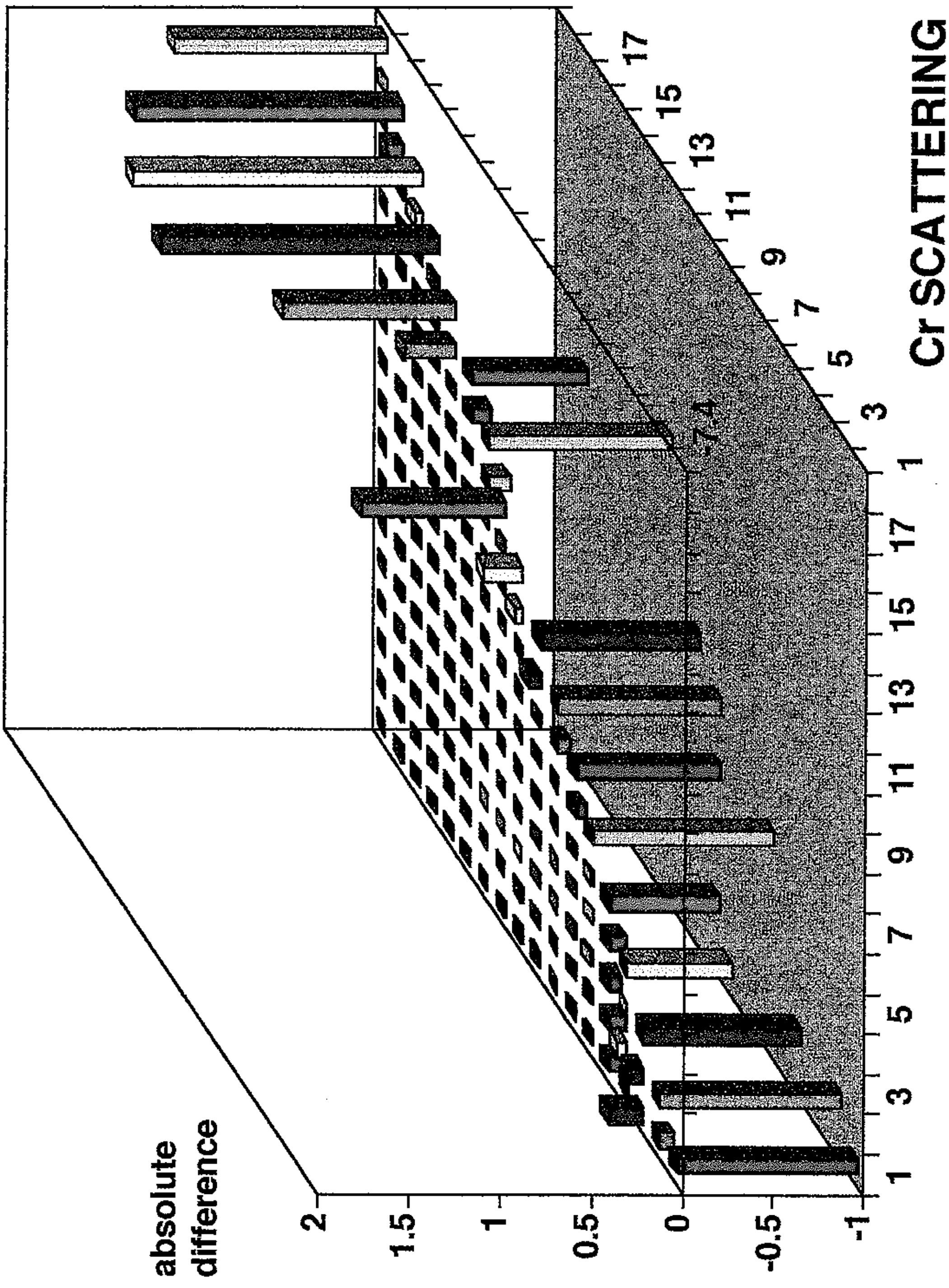

Figure 7.14 Absolute differences in Cr scattering cross-sections

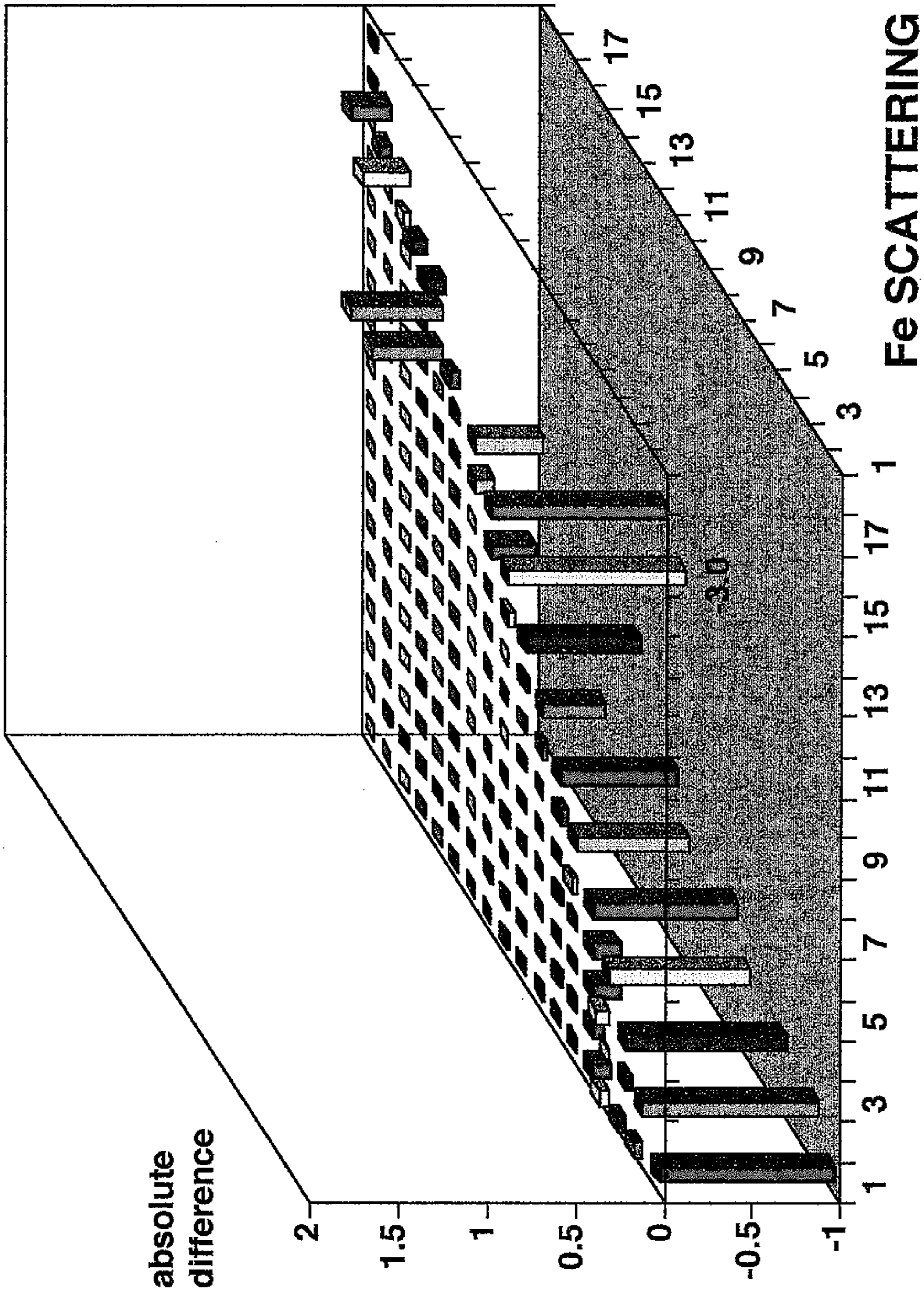

Figure 7.15 Absolute differences in Fe scattering cross-sections

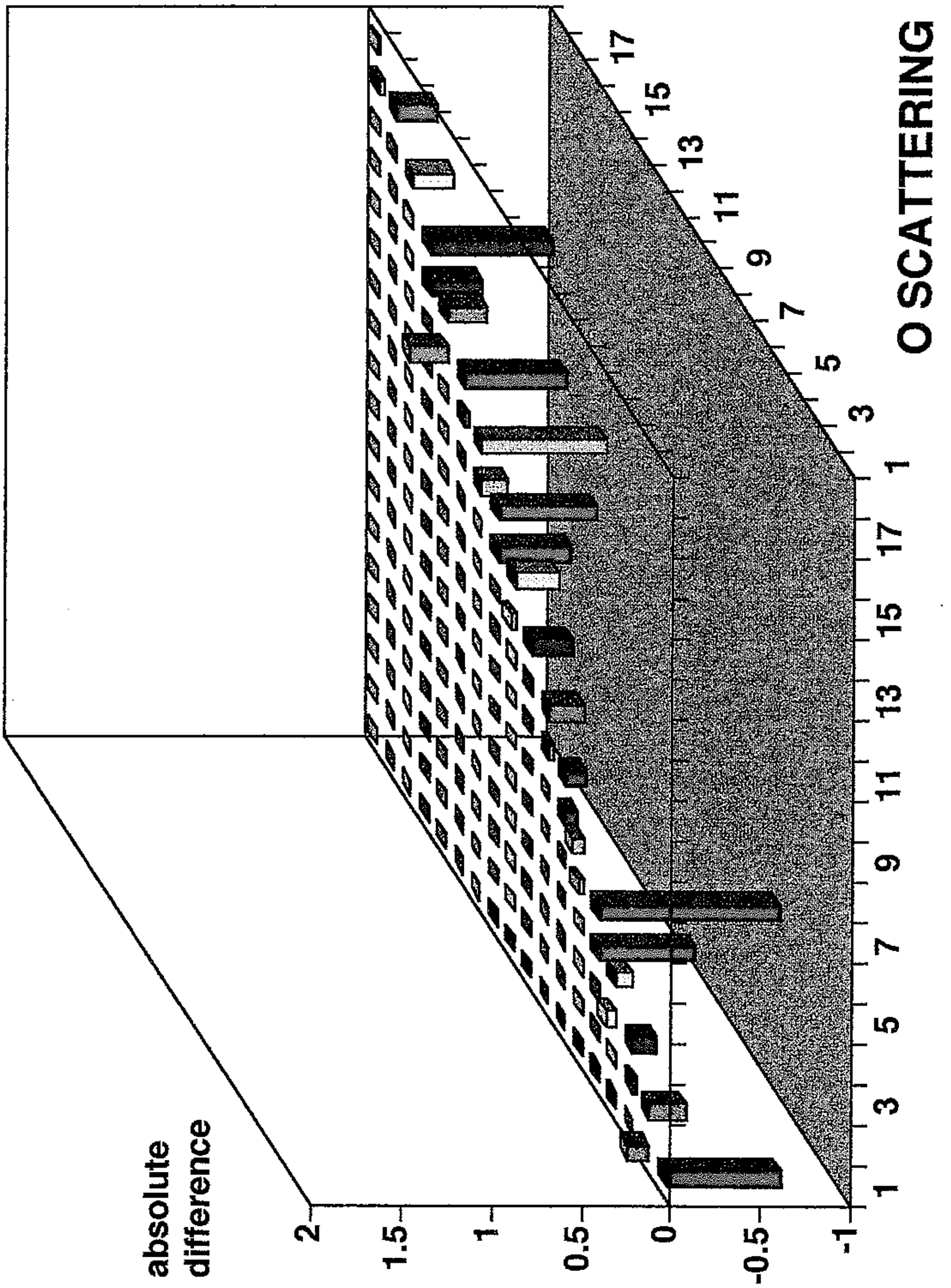

Figure 7.16 Absolute differences in O scattering cross-sections

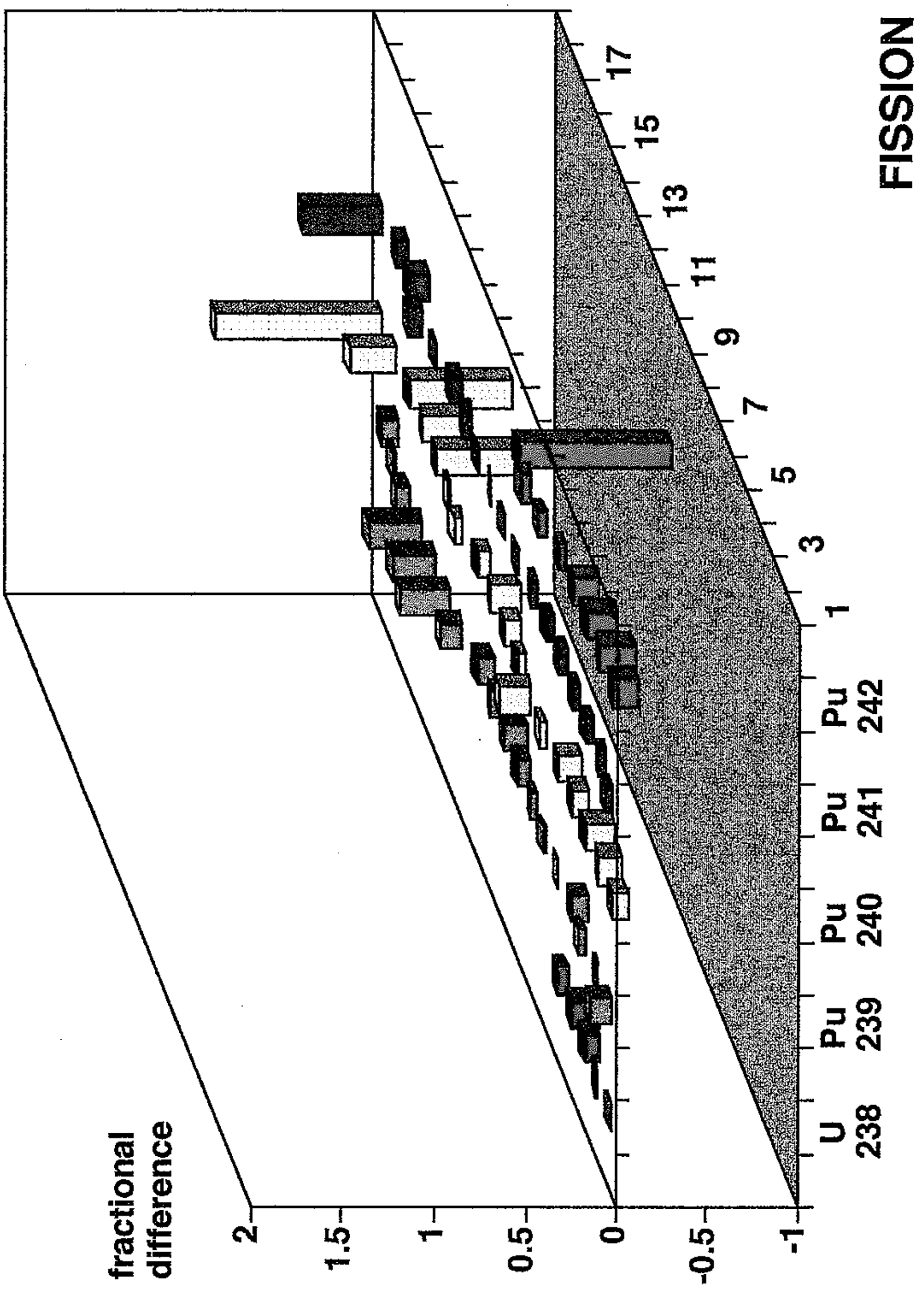

Figure 7.17 Fractional differences in fission cross-sections

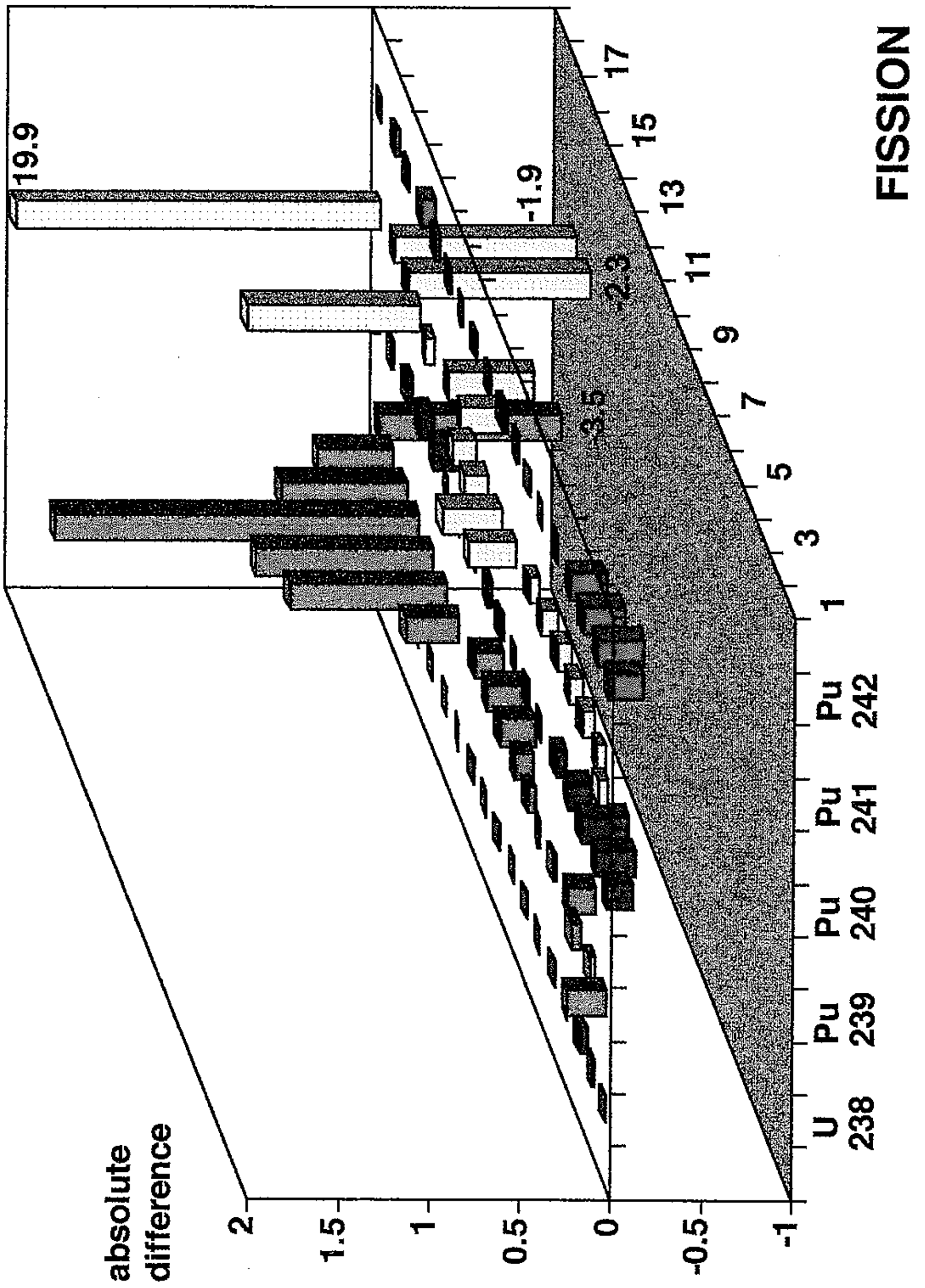

Figure 7.18 Absolute differences in fission cross-sections

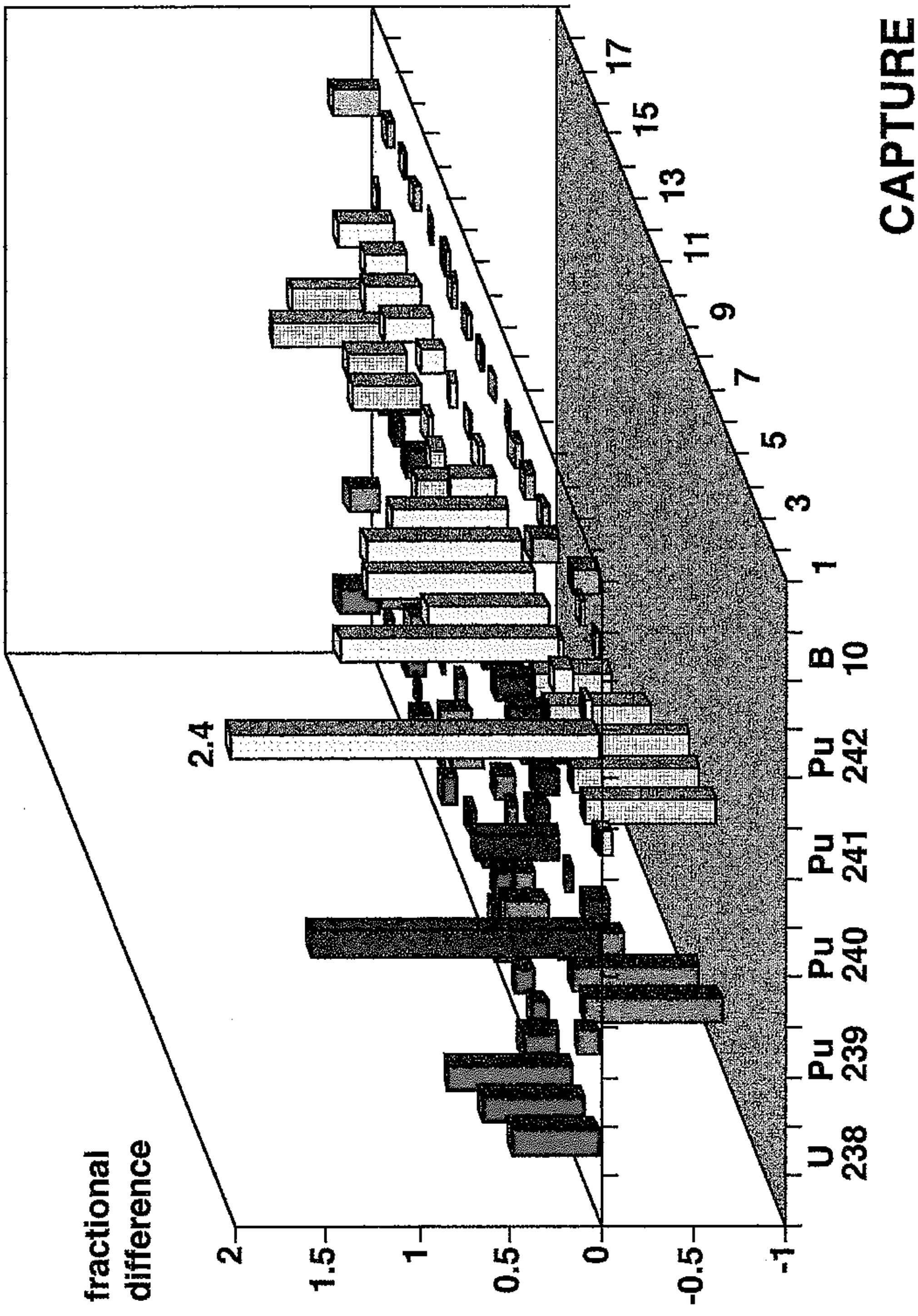

Figure 7.19 Fractional differences in capture cross-sections (I)

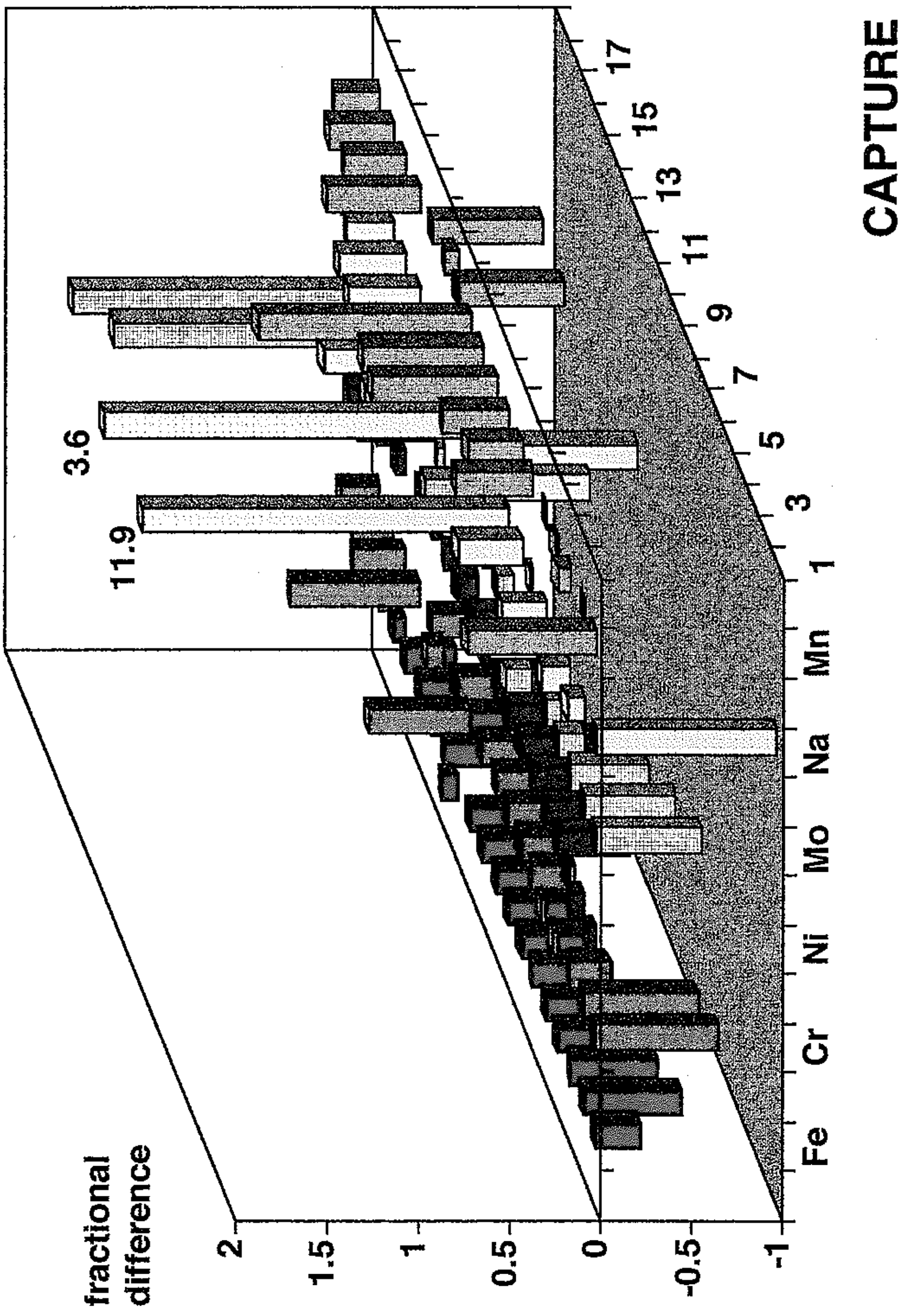

Figure 7.20 Fractional differences in capture cross-sections (II)

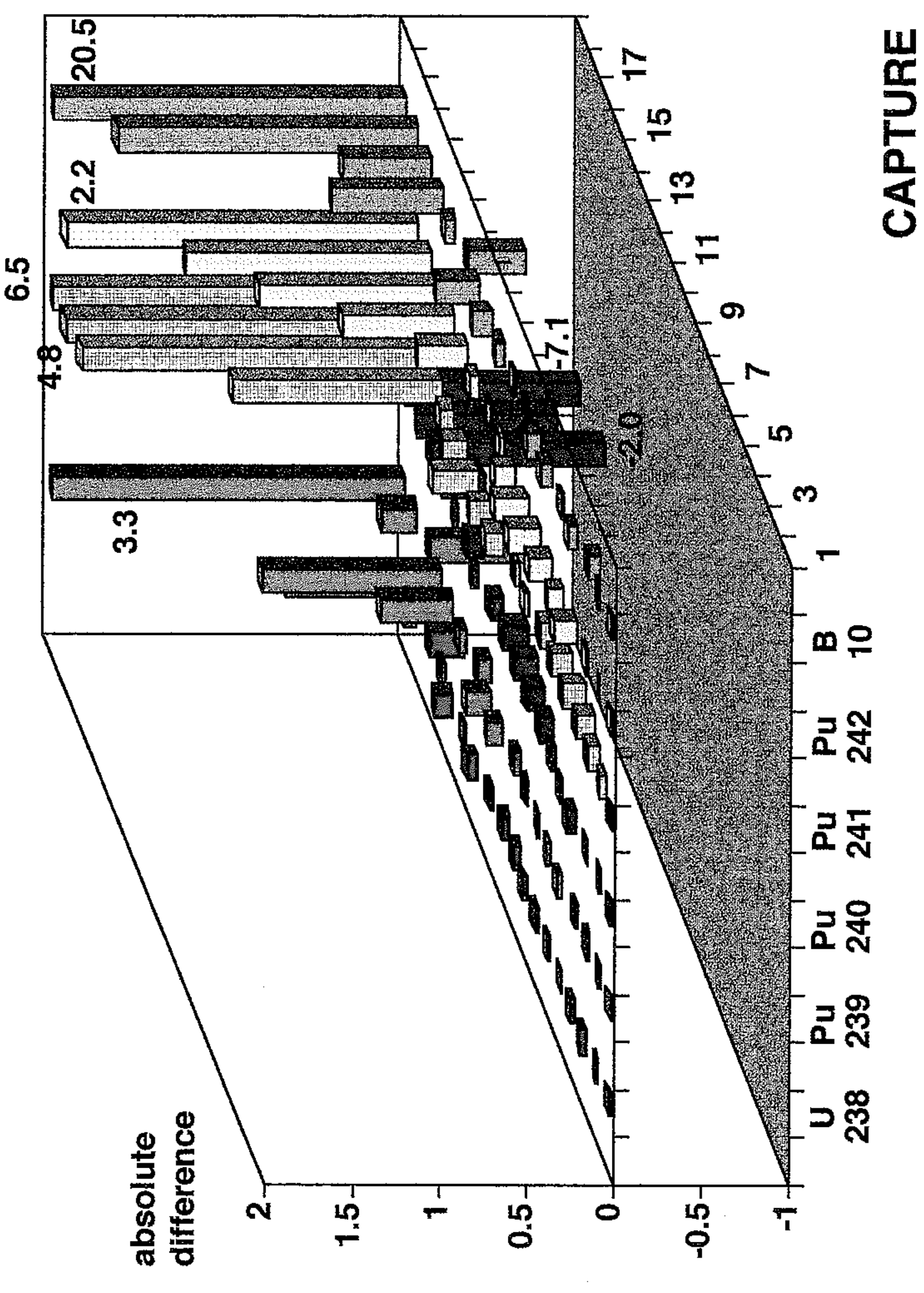

Figure 7.21 Absolute differences in capture cross-sections (I)

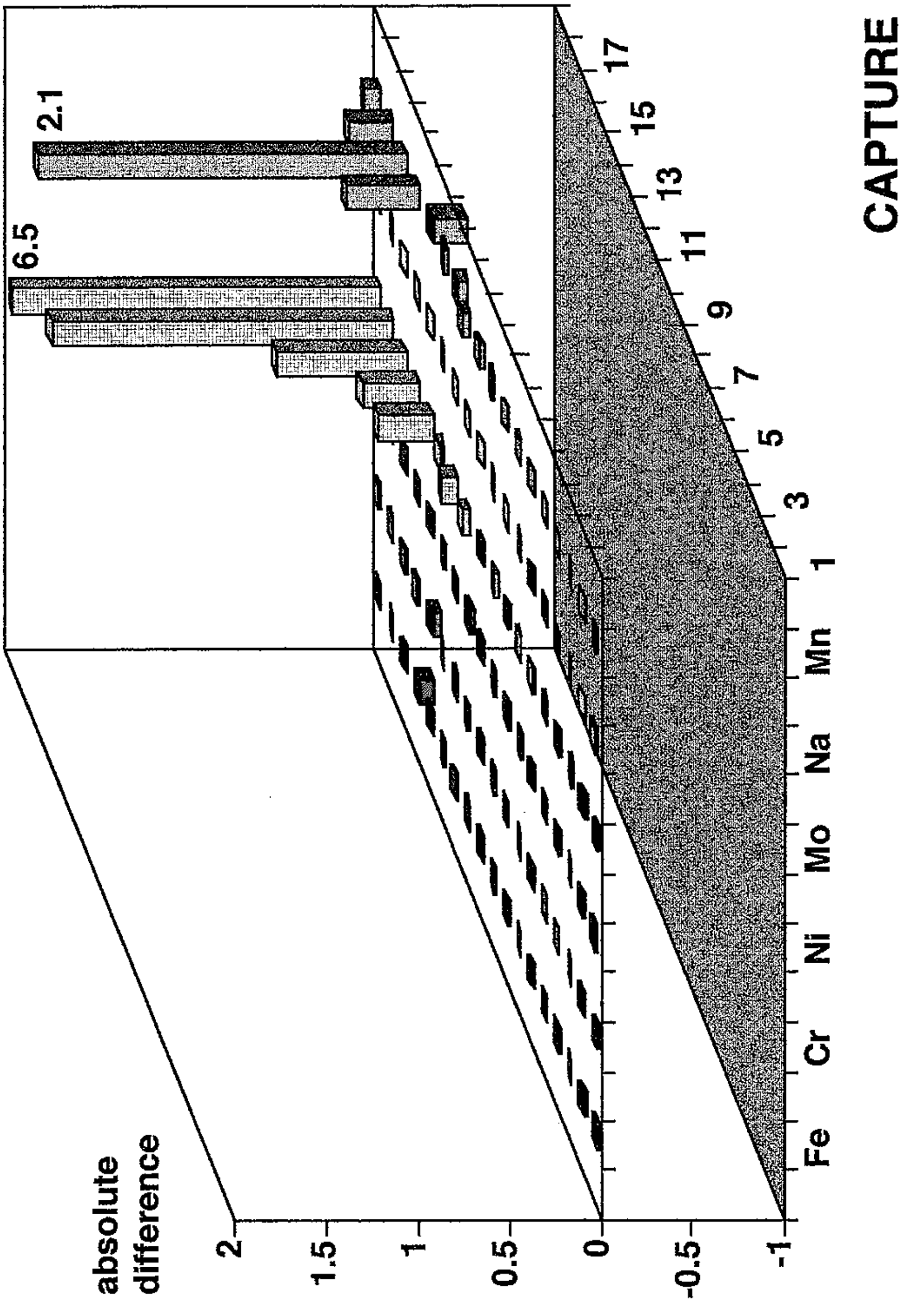

Figure 7.22 Absolute differences in capture cross-sections (II)

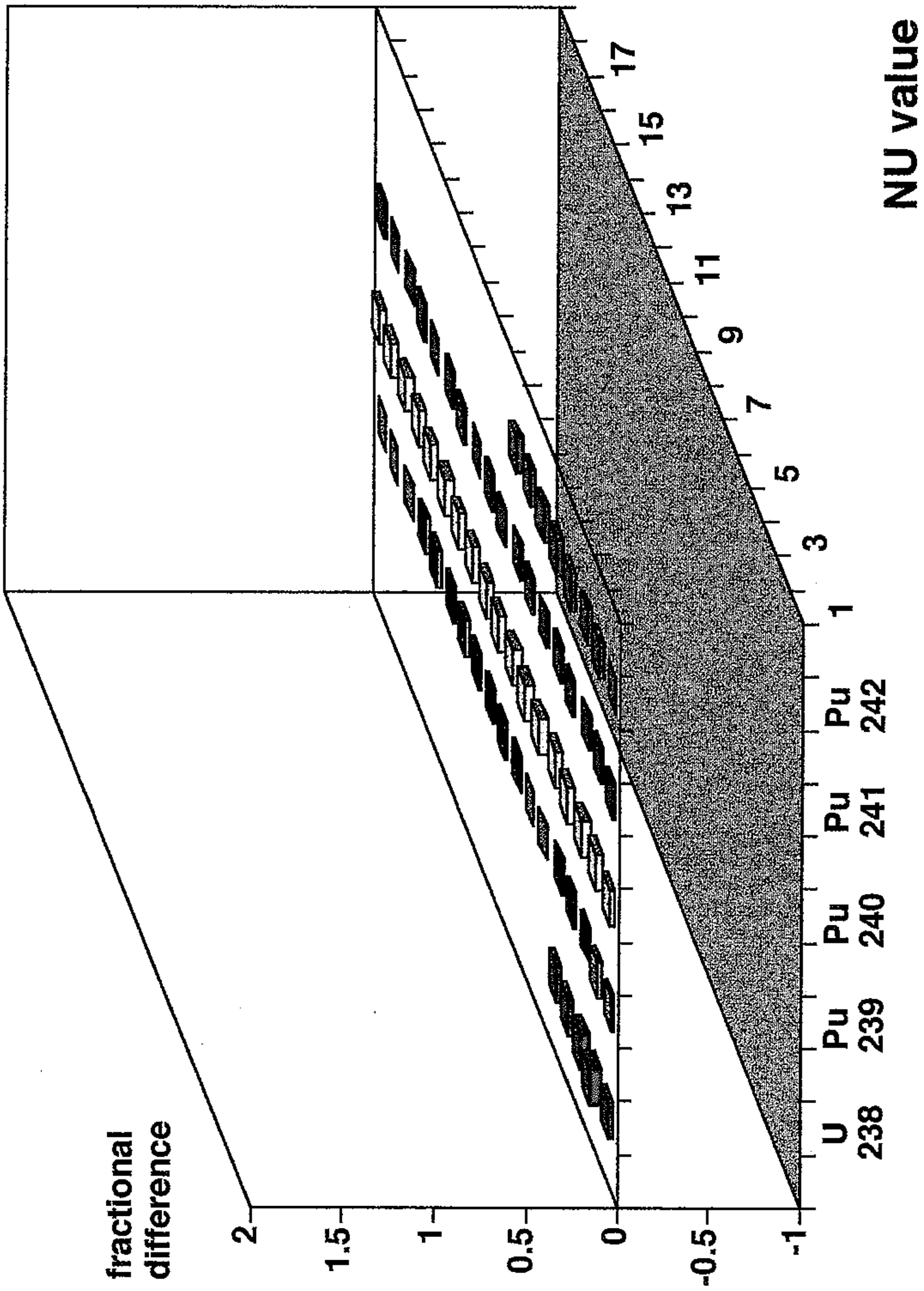

Figure 7.23 Fractional differences in Nu values

8 CONCLUSIONS

Calculations have been carried out to model the flux and rating distributions in an experimental loading of a start-up core at Super-Phenix (SPX). By comparing the results with those from equivalent CEA calculations, some comparison of PNC and CEA calculation methods was possible. Both sets of calculations were also assessed against SPX measurements. Major results from the analysis are presented here; the full comparison exercise was carried out by CEA.

The results showed that Keff values calculated by CEA were higher than those calculated by PNC, by ~2% for core configurations without absorber material and by ~1% for configurations including absorber: of the differences in PNC and CEA calculations, the nuclear datasets used are the most likely cause of the Keff differences. By comparing different pairs of calculations it was possible to obtain values representative of reactivity loss with burn-up and of absorber worth. There was little difference in the reactivity losses: 0.61%Δk/kk' for CEA and 0.66%Δk/kk' for PNC. The absorber worth was rather higher in the CEA calculations, 2.90%Δk/kk' as compared with 1.82%Δk/kk'. The CEA calculations used a reduction in boron density to approximate the absorber heterogeneity effects, rather than the explicitly heterogeneous cell model of the PNC calculations: absorber modelling is an area of significant difference between PNC and CEA calculations.

The calculated flux and rating distributions showed a radial tilt relative to the SPX measurements, the CEA calculations produced a larger tilt than did the PNC calculations. The radial tilts, the fraction by which the ratio of inner to outer ratings differs from the SPX measured value, were 6% and 9% for the PNC calculations but 22% and 23% for the CEA calculations (the values are for two different core configurations).

The comparison exercise included a case modelled by IPPE (Russia). The resulting radial rating shape was very similar to that produced by PNC, though with a slightly larger radial tilt - 10% rather than 6%. It was concluded that the PNC and IPPE calculation routes (including nuclear data) had a greater consistency with each other than either did with the methods of CEA.

CEA carried out an analysis of the component factors of the radial tilt in one of their calculations. A single factor was identified as being the major source of radial tilt differences between the PNC and CEA calculations: the differences in the two nuclear datasets used, JENDL-3.2 and CARNAVAL IV. As a consequence of this result, the study was extended to include a further stage, a comparison of the two nuclear datasets.

The differences between the JENDL-3.2 and CARNAVAL IV datasets, in terms of the variation caused in radial tilt, were analysed using a calculational route based on the SAGEP program. Because of some incompatibilities in the formats of the two sets of nuclear data, it was not possible to incorporate all of the reaction types normally included in the SAGEP based analysis. As the results showed, there were many nuclear data items displaying large differences between the two datasets, this was not consistent with the assumptions of the perturbation theory on which the SAGEP calculations are based. Because of these two effects, the SAGEP based sensitivity analysis did not calculate too accurate a value for the radial tilt caused by the differences in the nuclear datasets: 28%, compared with a value of 13% directly from flux/rating calculations using the two datasets. Despite this discrepancy, the SAGEP sensitivity analysis is still considered valid for its main usage - the identification of the relative contributions by different nuclear data items to the radial tilt difference.

The radial tilt difference between the JENDL-3.2 and CARNAVAL IV datasets was found to be dominated by the contributions from relatively few data items. The three largest items contributed as much as 25% of the total, whilst 10 items produced 50% of the total and 50 items nearly 80%. The three largest contributions come from: Pu^{239} fission (group 15), U^{238} scatter and O scatter (both group 5, in-group scattering); other significant contributors are listed in Table 7.4.

The SAGEP sensitivity analysis assessed the differences in nuclear data in the light of their effect on the radial tilt in the SPX reactor model. The differences in cross-section values were also examined directly. This revealed that the domination of the radial tilt by contributions from a small number of reactions was generally a consequence of the radial tilt being particularly sensitive to certain reactions, rather than of isolated large differences between the two nuclear datasets. In many cases (e.g. Figures 7.14, 7.18) there was seen to be a smooth variation in the cross-section difference with energy group, implying that these items may have a common source for the two datasets, but with different systematic evaluating procedures.

The cross-section differences, depicted in Figures 7.9 to 7.23, showed the following. The Nu values differ by at most 5%. The fission cross-sections generally differ by up to ~10%, with a small number of values showing variations up to 30%; there are a very few values with larger fractional differences but these correspond to small values of absolute cross-section difference. For the scattering cross-sections, the only significant absolute differences are for near-diagonal values (in-group or down-1-group scattering), other values are orders of magnitude smaller; however, there are some very large fractional differences (up to ~200%) for values in the body of the matrix, the near-diagonal values show fractional differences up to ~75% though they are generally less than 20%. The absolute differences in capture cross-sections are small compared with those for fission or scattering, except at low energies for B^{10}, Mo, Mn and the actinides; however, there are many values for which the fractional difference is large (~30-200%); exceptionally, for Na group 8 the difference is ~1000%.

The CEA assessment of the effects contributing to the radial tilt included the production of updated calculations, with identified shortcomings corrected as far as possible - e.g. transport model, more energy groups. The calculation update included the projected replacement of the CARNAVAL IV nuclear data with data from the ERALIB-1 file (which is based on JEF-2.2). It would be appropriate to use the SAGEP sensitivity analysis as described in this report to assess the radial tilt difference between the JENDL-3.2 and ERALIB-1 nuclear data sets. This has not so far been done, since the ERALIB-1 based data has not yet become available.

ACKNOWLEDGEMENT

The author wishes to express his thanks to PNC for being given the opportunity under the International Fellowship scheme to come to work in Japan and undertake the task reported herein.

The work was carried out under the supervision of the General Manager of the Reactor Physics Research Section, Dr. T. Wakabayashi, who provided the right level of support to allow the task to be carried out in an effective and rewarding manner. Both Dr. T. Wakabayashi and the Deputy General Manager of the Reactor Physics Research Section, Mr. M. Ishikawa, participated in technical discussions which were essential to guiding the direction of the work as it progressed.

The work would have been immeasurably more onerous, if not impossible, without the willing contributions of all the members of the Reactor Physics Research Section, in helping me understand the various computer systems and programs used, and particularly in facilitating access to various Japanese reports and data sources.

REFERENCES

3-1 T.B.Fowler et al. Nuclear reactor core analysis code: CITATION ORNL-TM-2496, Rev. 2 (1971)

3-2 T.Nakagawa, T.Asami, T.Yoshida. Curves and tables of neutron cross sections - Japanese Evaluated Nuclear Data Library version 3. JAERI-M 90-099 (1990) (under revision)

3-3 M.Nakagawa, K.Tsuchihashi. SLAROM: A code for cell homogenization calculation of fast reactor. JAERI 1294 (1984)

6-1 A.Hara, T.Takeda, Y.Kikuchi. SAGEP: two-dimensional sensitivity analysis code based on generalized perturbation theory. JAERI-M 84-027 (1984)